Part I. Vortex Dynamics in Wake Models

Part II. Wave Generation

Thesis by

David J. Hill

In Partial Fulfillment of the Requirements

for the Degree of

Doctor of Philosophy

California Institute of Technology

Pasadena, California

1998

(Submitted May 20th, 1998)

Acknowledgements

I thank my advisor, Professor Philip G. Saffman, for his invaluable guidance, encouragement, and patience. I gratefully acknowledge his support and am thankful for the opportunity to have learned from him.

I would like to thank Darren Crowdy, Donal Gallagher, Ron Henderson, Phill Kang, Michael Lough, and Aure Prochazka for many useful discussions and their valued friendships. An excellent environment for study and research has been provided by the entire department of Applied Mathematics.

Moira Regelson and my parents Steve and Elinor Hill have supplied in large part the affirmation and emotional support which have aided me greatly in this endeavor.

Abstract

In Part I, steady wakes in inviscid fluid are constructed and investigated using the techniques of vortex dynamics. As a generalization of Föppl's flow past a circular cylinder [5], a steady solution is given for flow past an elliptical cylinder of arbitrary aspect ratio (perpendicular or parallel to the flow at infinity) with a bound wake of two symmetric recirculating eddies in the form of a point vortex pair. Linear stability analysis predicts an asymmetric instability and the symmetric nonlinear evolution is discussed in terms of a Kirchhoff-Routh path function. The wake behind a sphere is represented by a thin cored vortex ring of arbitrary internal structure. Steady configurations are obtained and long-wavelength perturbations to the ring centerline identify a tilting instability. A generalization of the Kirchhoff-Routh function to an axisymmetric flow consisting of vortex rings and a body is presented. Using conformal maps and point vortices, translating symmetric two-dimensional bubbles with a vortex pair wake are constructed. An instability in which the bubble and vortex pair tilt away from each other is found as well as a symmetric oscillatory instability. The cross-section of a trailing vortex pair immersed in a cross stream shear is represented by two counter-rotating vortex patches. Numerical and analytical analyses are provided. The method of Schwarz functions as introduced by Meiron, Saffman and Schatzman [13] is used in the computation and stability analysis of steady patch shapes. Excellent agreement is obtained using an elliptical patch model. An instability essentially isolated to a single patch is identified, the nonlinear evolution of the elliptical patch model suggests that the patch whose fluid elements rotate against the shear will be destroyed.

Part II examines a possible mechanism for the generation of water waves which arrises from the instability of an initially planar free surface in the presence of a parallel, sheared, inviscid flow. A two-dimensional steady flow comprised of exponential profiles representing both wind and a drift layer in the water is infinitesimally

perturbed. The resulting Rayleigh equation is analytically solved by mean of Hypergeometric functions and the dispersion relation is implicitly defined as solutions of a transcendental equation; stability boundaries are determined and growth rates are calculated. Comparisons are made with the simpler model of Caponi *et al.* [2] which uses piecewise linear profiles.

Contents

List of Figures

List of Tables

Part I

Vortex dynamics in wake models

Introduction

A canonical wake structure behind a body is typified by bound vorticity which forms a continuously circulating bubble of fluid. In two dimensional flow, such a wake consisting of two symmetrically situated counter-rotating vortices is observed in the early stages of an impulsively started flow past a circular cylinder. While below a critical Reynolds number ($Re \sim 48$) this flow is stable, an increase in Reynolds number leads initially to a symmetry breaking instability followed by the formation of a vortex street. There is a similar sequence of changes in the flow past most bodies. For instance, a region of closed streamlines behind a sphere forms a standing ring-eddy at about $Re = 17$. Again an instability in the flow pattern develops above a critical value of the Reynolds number. Recent numerical computations [6], [38]&[25] indicate that as the Reynolds number is increased the first instability ($Re \sim 212$) appears in the near-eddy separated region of the flow as a non-axisymmetric regular bifurcation. As the Reynolds number continues to increase, shedding occurs. While no regular pattern of motion like the vortex street appears to form in the wake, Bachelor [1, p. 262] suggests that vorticity is shed " *in something like a succession of distorted vortex loops not symmetrical about the central axis.*"

We hasten to remark that bound wakes are not limited to solid bodies or bodies with a "no-slip" fluid-body boundary condition. For example, wake formations may be seen to affect the shapes and behavior of bubbles. Ryskin and Leal [29],[30] first computed steady shapes and flows for three dimensional axisymmetric rising bubbles with bound wakes at a variety of Reynolds numbers. In experiments, Kelley and Wu [7] visualized wake structures behind circular bubbles in a Hele-Shaw cell and present evidence that wake shedding (whose onset is controlled by the Reynolds number) is responsible for the zigzagging path of rising two dimensional bubbles.

In 1913 Föppl [5] presented a simple inviscid model representing the wake formed by two recirculating eddies behind a circular cylinder in incompressible flow. In this model the two dimensional velocity field is approximated by potential flow with two counter-rotating point vortices symmetrically situated behind the cylinder. Linear

stability analysis shows the model to be unstable by means of a symmetry breaking convective mechanism. Of course as this is an inviscid model, it is unable to predict the critical Reynolds number at which at which the real viscous flow first exhibits this instability. Föppl's configurations has recently been re-examined by DeLaat and Coene [4] who extended the model to the case of a simple wing-body combination in a cross-flow. Tang and Aubry [36] compared the inviscid model to computations of a impulsively started viscous flow.

In the following chapters we generalize Föppl's model to address the wake structure of flow past elliptically shaped cylinders, spheres, and two dimensional bubbles. We use conformal mapping techniques and image systems in Chapter One to determine the steady location of a point vortex pair of given strength behind an elliptically shaped cylinder of arbitrary aspect ratio. The resulting flow is shown to be stable to symmetric perturbations but unstable to a symmetry breaking perturbation which tilts the vortex pair. To further investigate the evolution of a non-steady symmetric configuration, a Hamiltonian based on the finite part of the kinetic energy is formed (and shown to correspond to the Kirchhoff-Routh path function). For the flow past an arbitrarily shaped symmetric body, the Hamiltonian allows us to determine from symmetric initial vortex locations behind the body if the vortex pair will be advected down stream, orbit steady locations, or over take the body and continue up stream.

Vortex filament theory is used to construct a model of the wake behind a sphere in Chapter Two. The model is again inviscid and features an axisymmetric configuration of a thin cored vortex ring behind a sphere. For a given flow at infinity, the down stream location, ring radius and core radius of the ring are prescribed and the circulation of the ring and the average internal core structure are determined. By constructing an appropriate image system and modifying the arguments of Widnall and Sullivan [43] , we show that the wake model is unstable to a symmetry breaking tilting of the vortex ring. We create a Hamiltonian (which generalizes the Kirchhoff-Routh path function to vortex rings) which describes the axisymmetric interaction of vortex rings of arbitrary internal structure with an axisymmetric body.

The role a vortex wake plays in the shape and stability of two dimensional bubble

receives attention in Chapter Three. The region of fluid external to a translating bubble of constant shape is taken to be the image of the unit disk under an unknown conformal map constructed in a manner which places a vortex pair wake behind the bubble and satisfies a Bernoulli equation at the bubble interface. For a given Weber number and nondimensional vortex pair strength, the map (and hence the shape of the bubble and vortex locations) is numerically calculated. The shapes of the steady bubbles range from circular (very high surface tension) to having a concave upstream face (very strong vortex wake). Linear stability analysis indicates that all solutions are unstable to a perturbation in which the vortex pair and bubble tilt away from one another. For a certain range of Weber number, a symmetric displacement of the vortices leads to unstable symmetric oscillations which may be interpreted as a cooperative instability between two otherwise stable symmetric perturbations; the oscillations of a point vortex wake and the oscillations of the bubble shape.

While the recirculating eddies are an important paradigm, one observes a separate class of wakes behind a lifting surface. In an idealization, the vortex field behind a wing forms a sheet which rolls up for down stream distances into a structure which is approximated by two parallel counter rotating vortex filaments. A point of principle interest is the behavior of the wake for large distances from the lifting surface, as the existence of these counter rotating trailing vortices presents a hazard for aircraft and may be used to deduce the location of submarines. Aeroplanes may experience a loss of control when passing through the trailing vortices created by other aircraft and the trailing vortices created by submarines may be detected when they impinge upon the ocean surface as elevation disturbances or by the cold water or salinity they may transport from the depths. By modeling the trailing vortices as two infinitely long counter-rotating vortex filaments in unbounded potential flow Crow [3], identified a three dimensional co-operative instability which may lead to the mutual destruction of the vortices. We investigate a two dimensional mechanism which leads to the destruction of only one of the trailing vortices in Chapter Four. We take the trailing vortices to be immersed in a cross-stream shear, representing perhaps the wind in an atmospheric boundary layer. We assume no spanwise variation in the vortices and

examine a characteristic two dimensional cross-section of the flow. Patches of constant vorticity embedded in a linear shear velocity are used to model the cross-sections and steady patch shapes are numerically determined. Two families of solutions are found. One is stable to two dimensional perturbations and the other is unstable. The two solutions differ primarily in the shape of the patch whose fluid elements rotate against the shear, this patch is more elongated in the unstable solution. An examination of a perturbation with a corresponding positive growth rate suggests that the instability is relatively isolated to that patch. We formulate an analytic model based on elliptically shaped vortex patches in shear combined with the dispersion relation for a single patch in unbounded shear and strain. This simple approach produces results which are in excellent agreement with our numerics and allows us to examine the nonlinear evolution of the patch shapes. The evolution of the patches under this elliptical approximation suggests that the trailing vortex which is signed against the shear may be destroyed while the other trailing vortex persists.

Chapter 1 The Föppl Problem for non-circular bodies

1.1 Introduction

The inviscid two-dimensional problem of two counter-rotating point vortices of strengths $+\Gamma$ and $-\Gamma$ situated symmetrically behind a circular cylinder of radius a in uniform flow was first studied in 1913 by Föppl [5]. Placing the co-ordinate origin at the center of the cylinder and orienting the axes such that the flow at infinity tends to parallel flow of speed U in the x direction, Föppl found that the vortex pair is steady with respect to the circular cylinder if it lies on the curve defined in polar co-ordinates (ρ, θ) by

$$\left(1 - \frac{a^2}{\rho^2}\right) = \pm 2 \sin\theta \tag{1.1}$$

with a strength Γ specified as

$$\frac{\Gamma}{2\pi U a} = -\frac{(\rho^2 - a^2)^2 (\rho^2 + a^2)}{a\rho^5}. \tag{1.2}$$

A second family of steady solutions can also be given for the vortex pair on the y-axis centered about the cylinder where

$$\frac{\Gamma}{2\pi U a} = -\frac{2(y^2 + a^2)^2 (y^2 - a^2)}{ya((y^2 + a^2)^2 + 2a^2(y^2 - a^2))}. \tag{1.3}$$

See Figure 1.1.

Föppl examined the stability of the vortex pair behind the cylinder to infinitesimal two dimensional perturbations of the positions of the vortices. Despite some mathematical errors as pointed out by Soibelman (private communication), Föppl identified correctly an instability to asymmetric disturbances. Descriptions of Föppl's steady

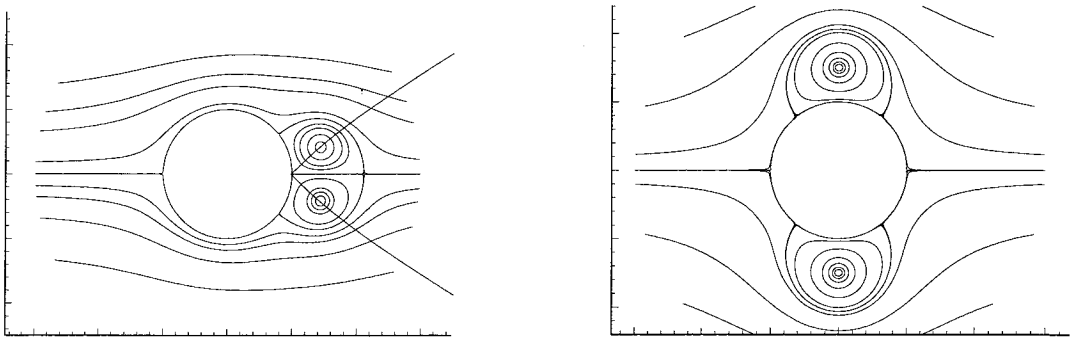

(a) Vortex pair behind cylinder

(b) Vortex pair centered on cylinder

Figure 1.1: The two symmetric stationary configurations for $r/a = 1.5$. In (a) the curve defined by (1.1) is drawn

configurations can be found in some of the standard references: it is included in Lamb's "Hydrodynamics" and "Theoretical Hydrodynamics" by Milne-Thomson as well as Saffman's "Vortex Dynamics". The stability characteristics of such flows have recently enjoyed a renewed interest as simple models of possible convective instability. Tordella [39] examined the stability of Föppl flow during transient motions and De-Laat and Coene [4] analyzed a generalized Föppl flow related to the case of a simple wing-body combination in a cross-flow.

In this chapter, after a brief review of complex flow, we will use simple conformal mapping techniques to generalize Föppl's original configuration. This generalization is effected by replacing the circular cylinder with an elliptic cylinder of arbitrary aspect ratio. We will maintain symmetry by requiring either the major or minor axis be aligned with the flow at infinity. Two families of steady solutions are identified. Both are shown to be unstable to infinitesimal asymmetric perturbations but one family is shown to be stable to infinitesimal symmetric disturbances. We generalize this symmetric result by using Kirchhoff-Routh functions to describe the trajectories on which the non-steady symmetric vortex pair travels. In subsequent chapters we examine two further generalizations: a vortex ring behind a sphere and a two-dimensional bubble with a point vortex wake.

1.2 Complex Flow

For the sake of completeness and notational clarity we begin by reviewing the mathematical connection between two dimensional, incompressible, almost irrotational flow and the theory of complex analytic functions. By "almost irrotational" we allow vorticity only in the form of isolated delta functions.

For a two dimensional flow we use the common notation $\mathbf{u} = (u, v)$, where u is the velocity of the fluid in the x-direction and v is the velocity in the y-direction. The equations of incompressibility $\nabla \cdot \mathbf{u} = 0$ and irrotationality $\nabla \times \mathbf{u} = 0$ may be written as

$$\begin{aligned} \frac{\partial u}{\partial x} + \frac{\partial v}{\partial y} &= 0 \\ \frac{\partial u}{\partial y} - \frac{\partial v}{\partial x} &= 0 \end{aligned} \tag{1.4}$$

which may be interpreted as the Cauchy-Riemann equations for an analytic function $F = u - iv$ of the complex quantity $z = x + iy$. The first integral of this function defines the complex potential $W(z)$,

$$W(z) = \int^z F(\zeta)\, d\zeta. \tag{1.5}$$

Which when split into real and imaginary parts,

$$W = \Phi + i\Psi, \tag{1.6}$$

gives the scalar potential Φ and the streamfunction Ψ. The velocity field at point in the fluid may be obtained from either;

$$\frac{\partial \Psi}{\partial y} = u = \frac{\partial \Phi}{\partial x} \tag{1.7}$$

$$-\frac{\partial \Psi}{\partial x} = v = \frac{\partial \Phi}{\partial y}. \tag{1.8}$$

A point vortex is represented by a delta function of vorticity. Including a point

vortex with circulation Γ at the point z_o in the flow mathematically requires

$$\boldsymbol{\nabla} \times \mathbf{u} = \Gamma \ \delta(z - z_o) \tag{1.9}$$

or in terms of the streamfunction,

$$\nabla^2 \Psi = -\Gamma \ \delta(z - z_o). \tag{1.10}$$

Solving for the corresponding infinite space Green's function gives

$$\Psi = -\frac{\Gamma}{2\pi} \log |z - z_o| \tag{1.11}$$

which, when combined with its harmonic conjugate, gives the complex potential

$$W(z) = -i\frac{\Gamma}{2\pi} \log (z - z_o) . \tag{1.12}$$

To satisfy boundary conditions in a given region of interest or to account for the influence of other point vortices, the complex potential may be modified by the addition of a locally analytic function $F(z)$. In general the complex potential in the region of a point vortex has the form

$$W(z) = -i\frac{\Gamma}{2\pi} \log (z - z_o) + F(z). \tag{1.13}$$

As a final point in our discussion of the complex flow, we note the velocity field defined by this potential is singular at the point of vorticity itself;

$$u - iv = \frac{dF}{dz} - i\frac{\Gamma}{2\pi}\frac{1}{z - z_o}. \tag{1.14}$$

This singularity is simply the infinite rotational velocity induced by the delta function of vorticity: the point vortex is advected by the locally analytic flow,

$$u(z_o) - iv(z_o) = \frac{dF}{dz}(z_o). \tag{1.15}$$

1.3 Two counter-rotating point vortices behind an elliptic cylinder

In his paper Föppl [5] suggests that the flow may be modified to the configuration of a vortex pair behind a flat plate which is perpendicular to the flow at infinity. Föppl does discuss heuristically such a configuration but suggests in error that the locus of steady points is simply the image of the stationary curve behind the circular cylinder under the map which takes the circular cylinder to the plate. Furthermore, Föppl makes no speculation about the stability of such a system.

We generalize the problem by replacing the circular cylinder in the Föppl flow with an elliptic cylinder, of arbitrary aspect ratio, whose major axis is either perpendicular or parallel to the direction of the flow at infinity, thus retaining a degree of symmetry. Of course our solutions will include the case of a flat plate either parallel or perpendicular to the flow at infinity as well as Föppl's original flow. We mention that in the perpendicular flat plate limit, the flow has an infinite velocity at the plate ends and no Kutta condition is applied.

In general we find two families of steady locations for a vortex pair: behind the elliptic cylinder and centered about the cylinder. We perturb the steady solutions infinitesimally to examine the stability of the configuration to two dimensional disturbances.

1.3.1 A derivation of the equations of motion for a vortex pair in the presence of an elliptic cylinder

In this subsection we formulate the equations which govern the locations of two point vortices with opposite strengths in the presence of an elliptic cylinder centered at the origin. The boundary of the cylinder is a streamline and the flow tends to parallel flow at infinity with the positive x-axis pointing in the downstream direction.

To find the flow we use the complex velocity potential

$$W(\zeta) = U\left(\zeta + \frac{a^2}{\zeta}\right) - \frac{i\Gamma}{2\pi}\log\frac{(\zeta-\zeta_+)}{(\zeta-\zeta_-)} + \frac{i\Gamma}{2\pi}\log\frac{(a^2-\zeta\overline{\zeta}_+)}{(a^2-\zeta\overline{\zeta}_-)}; \tag{1.16}$$

where the derivative $dW/d\zeta$ gives the instantaneous velocity field $u-iv$ for flow about a circular cylinder of radius a with point vortices of strength $\pm\Gamma$ located at $\zeta_\pm$. We combine this potential with the conformal Joukowski transformation which maps a circle to an ellipse, and its inverse which maps the region outside of an ellipse to the area outside a circle:

$$z = \zeta + \frac{c^2}{4\zeta} \tag{1.17}$$

$$\zeta = \frac{1}{2}\left(z + \sqrt{z^2-c^2}\right) \equiv f(z) \tag{1.18}$$

where c is complex, $c = |c|\exp(i\phi)$, and $|c| \leq 2a$. Notice that under the map (1.17) the image of a circular cylinder $\zeta = a\exp(i\theta)$ is given by

$$\zeta = \exp(i\phi)\left((a+\frac{|c|^2}{4a})\cos(\tau) + i(a-\frac{|c|^2}{4a})\sin(\tau)\right) \tag{1.19}$$

where $\tau = \theta - \phi$. This describes an ellipse tilted an angle ϕ with major axis $(a + |c|^2/4a)$ and minor axis $(a - |c|^2/4a)$. The branch-cut in (1.18) is taken to be a line between $z = \pm c$, and thus inside the ellipse defined by (1.19), and the branch is chosen so that $\zeta \sim z$ for large z. We restrict ourselves to $\phi = 0$, which will correspond to an ellipse with its major axis aligned with the direction of the flow at infinity; and to $\phi = \pi/2$, which will correspond to the ellipse with its major axis perpendicular to the direction of flow at infinity. With this understanding we define the real quantity $\lambda \equiv c^2/(4a^2)$ which defines the shape of the ellipse. The aspect ratio may be computed as $(1-\lambda)/(1+\lambda)$ so that when $\lambda = -1$ we have a flat plate perpendicular to the flow, $\lambda = 0$ corresponds to the circular cylinder and $\lambda = 1$ gives the flat plat parallel to the flow.

The image of $|\zeta| = a$ gives the boundary of the elliptic cylinder with area $\pi a^2\left(1-\lambda^2\right)$;

the z-plane will be considered to be the physical plane occupied by the fluid. The physical boundary condition of no flow into the elliptic cylinder implies that the boundary of the cylinder is a stream line. This condition has already been met by the complex potential $W[f(z)]$ we defined in equations (1.16). Notice that when z is the image of a circle of radius a under the map (1.17) we have $\Psi\left(f(z)\right) = \Im\left[W\left(f(z)\right)\right] = \Im\left[W\left(ae^{i\theta}\right)\right] = 0$.

For a given ellipse, the locations of the point vortices define the flow and are in general time dependent. We can quickly derive the coupled ordinary differential equations which govern the position of the vortices. The locations $z_\pm$ of the two point vortices are given as the images of $\zeta_\pm$ under our map (1.17) so that

$$z_\pm = \zeta_\pm + \lambda\frac{a^2}{\zeta_\pm} \tag{1.20}$$

$$\zeta_\pm = f\left(z_\pm\right) \tag{1.21}$$

where $\zeta = f\left(z\right)$is the inverse map defined in equation (1.18). Notice that since λ is real, $\overline{z}_+$ is the image of $\overline{\zeta}_+$ and $\overline{z}_-$ is the image of $\overline{\zeta}_-$. In general the complex velocity $u - iv$ at a point z in the physical domain may be computed by using the chain rule

$$u(z) - iv(z) = \frac{dW}{df}\frac{df}{dz} \tag{1.22}$$

where according to equation (1.16)

$$\begin{aligned}\frac{dW}{df} &= U\left(1 - \frac{a^2}{\zeta^2}\right) \\ &\quad -\frac{i\Gamma}{2\pi}\left(\frac{1}{\zeta - \zeta_+} - \frac{\overline{\zeta}_+}{\zeta\overline{\zeta}_+ - a^2} - \frac{1}{\zeta - \zeta_-} + \frac{\overline{\zeta}_-}{\zeta\overline{\zeta}_- - a^2}\right).\end{aligned} \tag{1.23}$$

As we have mentioned such velocities are singular at the point vortices due to the infinite rotational velocity of a point vortex. The velocity of the flow which advects a given point vortex is found by removing the simple pole singularity when evaluating

(1.22) at the vortex, so

$$\begin{aligned}\frac{d\overline{z}_{\pm}}{dt} &= \lim_{z\to z_{\pm}}\{U\left(1-\frac{a^2}{\zeta^2}\right)\frac{df}{dz} \\ &\quad -\frac{i\Gamma}{2\pi}\left(\frac{1}{\zeta-\zeta_+}-\frac{\overline{\zeta}_+}{\zeta\overline{\zeta}_+-a^2}-\frac{1}{\zeta-\zeta_-}+\frac{\overline{\zeta}_-}{\zeta\overline{\zeta}_--a^2}\right)\frac{df}{dz}\pm\frac{i\Gamma}{2\pi}\frac{1}{z-z_{\pm}}\}\end{aligned} \tag{1.24}$$

where $\zeta = f(z)$. Using the relation

$$\lim_{x\to y}\left\{\frac{f'(x)}{f(x)-f(y)}-\frac{1}{x-y}\right\}=\frac{1}{2}\frac{f''(y)}{(f'(y))^2} \tag{1.25}$$

we find the equations which describe the motion of two counter-rotating vortices in the presence of an elliptical cylinder:

$$\begin{aligned}\frac{d\overline{z}_{\pm}}{dt} &= U\left(1-\frac{a^2}{\zeta_{\pm}^2}\right)\frac{df(z_{\pm})}{dz} \\ &\quad -\frac{i\Gamma}{2\pi}\left(\pm\frac{f''(z_{\pm})}{2(f'(z_{\pm}))^2}-\frac{\overline{\zeta}_+}{\zeta_{\pm}\overline{\zeta}_+-a^2}-\frac{1}{\zeta_{\pm}-\zeta_-}+\frac{\overline{\zeta}_-}{\zeta_{\pm}\overline{\zeta}_--a^2}\right)\frac{df(z_{\pm})}{dz}.\end{aligned} \tag{1.26}$$

1.3.2 The steady locations for a symmetrically situated vortex pair

We impose $z_+ = \overline{z}_-$ since we are looking for steady solutions of our system - defined by equation(1.26) - which are symmetric about the x-axis, i.e., the direction of flow at infinity. The steady system then satisfies

$$\left(1-\frac{a^2}{\zeta_+^2}\right)=\frac{i\Gamma}{2\pi U}\left(\frac{f''(z_+)}{2(f'(z_+))^2}-\frac{\overline{\zeta}_+}{|\zeta_+|^2-a^2}-\frac{1}{\zeta_+-\overline{\zeta}_+}+\frac{\zeta_+}{\zeta_+^2-a^2}\right). \tag{1.27}$$

To find the locus of possible positions of the point vortices, we start with the elimination of the parameter $\frac{i\Gamma}{2\pi U}$ by dividing equation (1.27) by its complex conjugate; dropping the subscript and simplifying yields

$$-(\zeta+\overline{\zeta})\left((|\zeta|^2-a^2)^2+|\zeta|^2(\zeta-\overline{\zeta})^2\right) \tag{1.28}$$

$$= \left|\zeta^2 - a^2\right|^2 a^2 \left(A(\bar{\zeta}^2 - a^2)\zeta^2 + \bar{A}(\zeta^2 - a^2)\bar{\zeta}^2\right)$$

where in terms of ζ

$$\begin{aligned} A &= \frac{f''(z)}{2\left(f'(z)\right)^2} \\ &= \frac{-\lambda}{\zeta\left(\zeta^2 - \lambda\right)}. \end{aligned} \tag{1.29}$$

We find steady configurations for the vortices behind the elliptical cylinder by assuming $\zeta \neq iy$. This leads to

$$\begin{aligned} &\left|\zeta^2 - \lambda\right|^2 \left\{\left(|\zeta|^2 - a^2\right)^2 + |\zeta|^2 \left(z - \bar{\zeta}\right)^2\right\} \\ = \; &\lambda a^2 \left|\zeta^2 - a^2\right|^2 \left\{a^2\lambda - |\zeta|^2 (a^2 + \lambda^2) + |\zeta|^2 \left(\zeta - \bar{\zeta}\right)^2 + |\zeta|^4\right\} \end{aligned} \tag{1.30}$$

Describing ζ in complex polar notation, $\zeta = r_s \exp(i\theta_s)$; this equation simplifies to give the curve

$$\sin^2(\theta_s) = \frac{\left(\left(\frac{r_s}{a}\right)^2 - 1\right)^2 \left(\left(\frac{r_s}{a}\right)^2 - \lambda\right)}{4\left(\left(\frac{r_s}{a}\right)^6 - \lambda\right)} \tag{1.31}$$

in the non-physical ζ-plane. The image of this curve under the map (1.17) defines the curve in the physical plane on which a vortex pair lies. Recall that the cylinder in the physical z-plane has aspect ratio $(1 - \lambda)/(1 + \lambda)$ with $|\lambda| \leq 1$ and the fluid corresponds to the image of points outside the circular cylinder indicating $r_s/a > 1$. When $\lambda = 0$ this result reduces to the curve (1.1) given by Föppl for the flow behind a circular cylinder. This curve emanates from the stagnation point at the back (or front) of the ellipse. The fore-aft symmetry of the curve is a result of the fore-aft symmetry of the ellipse and the time reversibility of the Euler equations. Equations (1.31) and (1.27) are used to determine the strength of a stationary vortex pair. The image of a given point $\zeta = r_s \exp(\pm i\theta_s)$ on the curve (1.31) will represent a stationary

vortex pair when the strength of the pair is given by

$$\frac{\Gamma}{2\pi U a} = -\frac{\left(\left(\frac{r_s}{a}\right)^2-1\right)^2\left(\left(\frac{r_s}{a}\right)^2+1\right)\left(\lambda-\left(\frac{r_s}{a}\right)^4\right)^2}{\left(\frac{r_s}{a}\right)\left(\lambda+\lambda\left(\frac{r_s}{a}\right)^8-2\lambda\left(\frac{r_s}{a}\right)^6-2\lambda\left(\frac{r_s}{a}\right)^4+\left(\frac{r_s}{a}\right)^2\lambda+\left(\frac{r_s}{a}\right)^{10}\right)}\sqrt{\frac{\left(\frac{r_s}{a}\right)^2-\lambda}{\left(\frac{r_s}{a}\right)^6-\lambda}}. \tag{1.32}$$

As an aside we note that there does not exist a steady symmetric vortex configuration *behind* a flat plate perpendicular to the flow such that the velocities at the tips of the plate are finite so that the Kutta condition can not be satisfied by such a configuration.

The equations for the vortex strength (1.32) and vortex location (1.31) in the ζ-plane together with the map define a first family of steady solutions. Obviously this is just the generalization of the solutions for the vortex pair behind the circular cylinder: equations (1.1) and (1.2). Figure 1.2 displays various steady solutions with point vortices behind elliptical cylinders; the curve on which any steady vortex pair must lie is also included.

The generalization of a second family of solutions comes from noticing that $\zeta = iy_s$, corresponding to vortices on the vertical axis in the physical plane $z = i(y_s - a^2\lambda/y_s)$, will solve the steady equation (1.28). This solution for point vortices located above and below the ellipse has strengths given by

$$\frac{\Gamma}{2\pi U a} = -\frac{2\left(\left(\frac{y_s}{a}\right)^2-1\right)\left(\left(\frac{y_s}{a}\right)^2+1\right)^2\left(\left(\frac{y_s}{a}\right)^2+\lambda\right)}{\left(\frac{y_s}{a}\right)\left(\left(\left(\frac{y_s}{a}\right)^2+1\right)^2\left(\left(\frac{y_s}{a}\right)^2+\lambda\right)+2\left(\frac{y_s}{a}\right)^2(1-\lambda)\left(\left(\frac{y_s}{a}\right)^2-1\right)\right)}. \tag{1.33}$$

Representative steady solutions are presented in Figure 1.3. One finds that this configuration also does not satisfy the Kutta condition in the case of a flat plate perpendicular to the flow.

1.4 The stability of the configuration

1.4.1 A derivation of the perturbation equations

To study the stability of the steady configuration with the vortex pair symmetrically situated down stream from an elliptic cylinder, we analyze the response to an in-

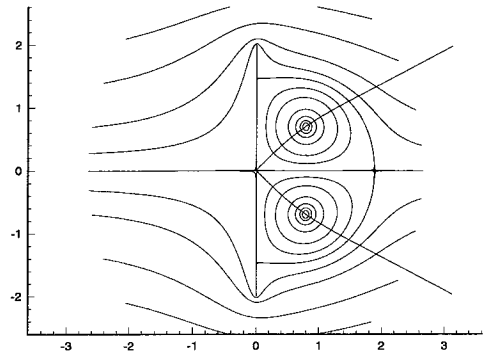

(a) $\lambda = -1$.

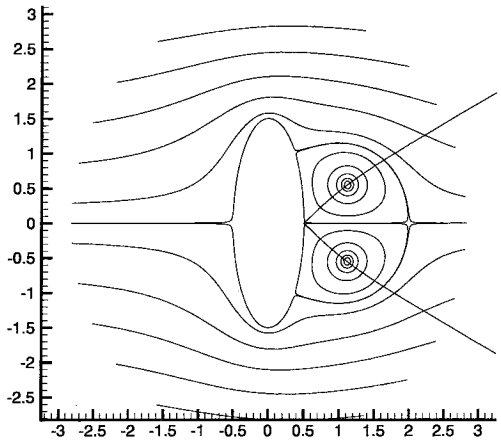

(b) $\lambda = -.5$

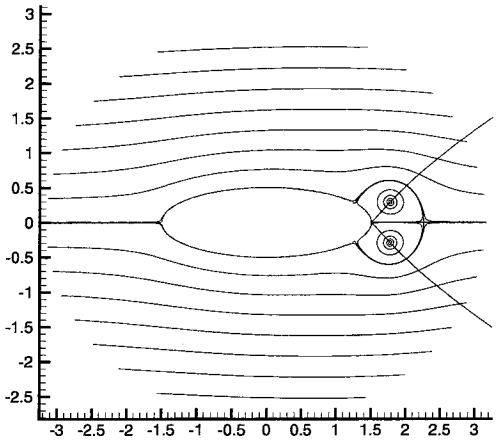

(c) $\lambda = +.5$

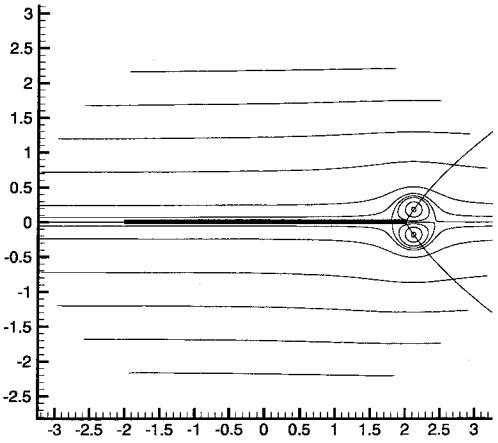

(d) $\lambda = +1$.

Figure 1.2: The generalized Föppl flow with vortices behind cylinders of various ellipticities. The locations and strengths of the vortices are determined by $r_s/a = 1.5$ in equations (1.31) and (1.32). The curve defined by (1.31) is also drawn.

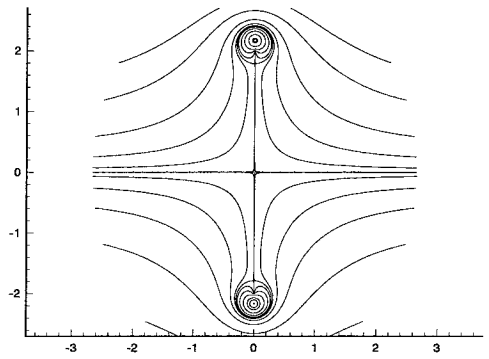

(a) $\lambda = -1$.

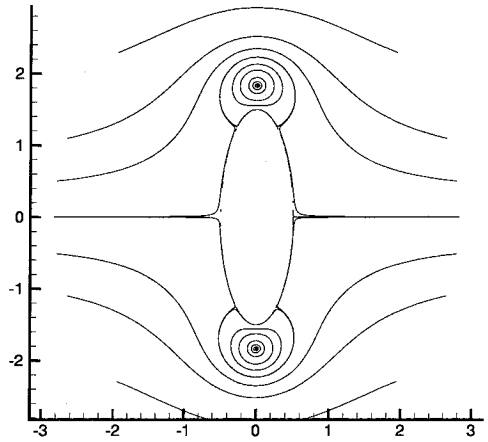

(b) $\lambda = -.5$

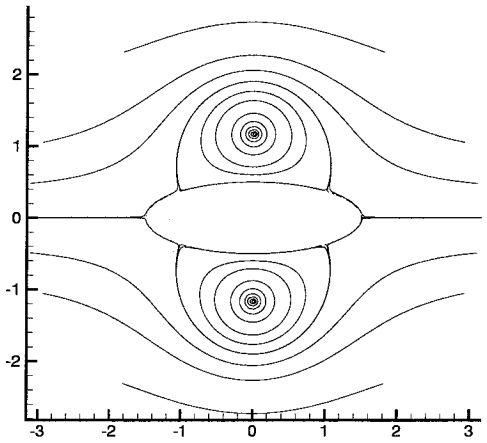

(c) $\lambda = +.5$

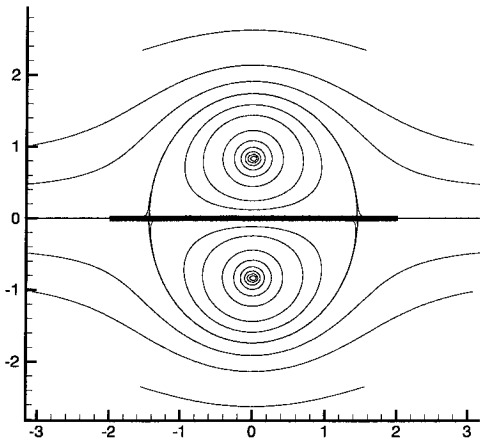

(d) $\lambda = +1$.

Figure 1.3: The generalized Föppl flow with vorticies centered on cylinders of various ellipticities. The strengths of the vortices are determined by $y_s/a = 1.5$ in equation (1.33).

finitesimal two dimension perturbation in the vortex location. The circulations $\pm\Gamma$ of the vortices are held constant. We assume the vortices' locations, z_+ and z_-, are given by

$$z_+(t) = z_+^s + \epsilon\widehat{z}_+(t) \tag{1.34}$$

$$z_-(t) = z_-^s + \epsilon\widehat{z}_-(t). \tag{1.35}$$

The quantities with an overhat are the time dependant perturbations and the superscript s denotes the steady solutions. The steady vortex locations, z_+^s and z_-^s, are the image of $\zeta_+^s = r_s \exp(i\theta_s)$ and its complex conjugate ζ_-^s under the map (1.17). Recall r_s and θ_s are defined for a specific ellipse and vortex strength by equations (1.32) and (1.31). To study the stability, we substitute the perturbed vortices, (1.34) and (1.35), into the equations of motion (1.26), linearize about the steady solution, and solve for the evolution of the infinitesimal perturbations.

We choose to examine the problem in the non-physical ζ-plane. Let

$$\zeta_+ = \zeta_+^s + \epsilon\widehat{\zeta}_+(t) \tag{1.36}$$

$$\zeta_- = \zeta_-^s + \epsilon\widehat{\zeta}_-(t) \tag{1.37}$$

so that under the conformal map (1.17) $\widehat{\zeta}_\pm$ relates to $\widehat{z}_\pm$ by

$$\widehat{z}_\pm(t) = \left(1 - \lambda\left(\frac{a}{\zeta_\pm^s}\right)^2\right)\widehat{\zeta}_\pm(t) + O\left(\epsilon^2\right). \tag{1.38}$$

Using the relationship $1 - \lambda\left(a/z_\pm^s\right)^2 = 1/\frac{df}{dz}$, the full equations of motion can be replaced with approximate evolution equations in the z plane accurate through order ϵ:

$$\overline{\left(\frac{d\widehat{\zeta}_\pm}{dt}\right)}\left|\frac{df\left(z_\pm^s\right)}{dz}\right|^{-2} \simeq U\left(1 - \frac{a^2}{\zeta_\pm^2}\right) \tag{1.39}$$

$$-\frac{i\Gamma}{2\pi}\left(\pm\frac{f''(z_\pm)}{2\left(f'(z_\pm)\right)^2} - \frac{\overline{\zeta}_+}{\zeta_\pm\overline{\zeta}_+ - a^2} - \frac{1}{\zeta_+ - \zeta_-} + \frac{\overline{\zeta}_-}{\zeta_\pm\overline{\zeta}_- - a^2}\right).$$

Notice that $|df/dz|^2$ will have the same value at either point vortex since $z^s_\pm$ are conjugates. To formulate our perturbation equations, we linearize the right hand side about the steady locations in the ζ-plane. Spliting the vortex locations into real and imaginary parts in the nonphysical plane,

$$\zeta_\pm(t) = x^s_\pm + iy^s_\pm + \epsilon(\hat{x}_\pm(t) + i\hat{y}_\pm(t)), \tag{1.40}$$

and assuming the time dependence of the perturbations is of the exponential form $\exp(\mu t)$ leads to an eigenvalue problem;

$$\left|\frac{df(z^s)}{dz}\right|^2 \mathbf{M}\vec{x} = \mu\vec{x} \tag{1.41}$$

where $\vec{x} = \{\hat{x}_+, \hat{y}_+, \hat{x}_-, \hat{y}_-\}^T$. We define instability as the existence of an eigenvalue with positive real part.

1.4.2 A simplification due to physical symmetries

Given a stationary location for the vortex pair in the non-physical ζ-plane, $\zeta^s = x^s \pm iy^s$, the appropriate linearized system (1.41) has certain symmetries. Let $M_{i,j}$ be the elements of the matrix $\mathbf{M}$; a change of basis to the physically motivated system of symmetric and asymmetric perturbations exploits these relations by de-coupling some of the equations, giving

$$\left|\frac{df(z^s)}{dz}\right|^2 \begin{bmatrix} M_{11}+M_{13} & M_{12}-M_{14} \\ M_{21}+M_{23} & -M_{11}-M_{13} \end{bmatrix} \vec{x}_{sym} = \mu_{sym}\vec{x}_{sym} \tag{1.42}$$

and

$$\left|\frac{df(z^s)}{dz}\right|^2 \begin{bmatrix} M_{11}-M_{13} & M_{12}+M_{14} \\ M_{21}-M_{23} & M_{13}-M_{11} \end{bmatrix} \vec{x}_{asym} = \mu_{asym}\vec{x}_{asym} \tag{1.43}$$

where $\vec{x}_{sym} = \frac{1}{2}\{\hat{x}_+ + \hat{x}_-, \hat{y}_+ - \hat{y}_-\}^T$ is the symmetric part of a perturbation and $\vec{x}_{asym} = \frac{1}{2}\{\hat{x}_+ - \hat{x}_-, \hat{y}_+ + \hat{y}_-\}^T$ is the asymmetric part. The corresponding eigenval-

ues are given by

$$\mu_{sym}^2 = \left|\frac{df(z^s)}{dz}\right|^4 \left((M_{11}+M_{13})^2 + (M_{12}-M_{14})(M_{21}+M_{23})\right) \tag{1.44}$$

and

$$\mu_{asym}^2 = \left|\frac{df(z^s)}{dz}\right|^4 \left((M_{11}-M_{13})^2 + (M_{21}-M_{23})(M_{12}+M_{14})\right). \tag{1.45}$$

Recall that we have two fundamentally different configurations for steady vortex pair in the presence of the elliptical cylinder. The pair is symmetrically located behind (and actually also ahead by time reversal) the cylinder or centered about the cylinder. We examine the stability of these two cases separately.

In order to calculate the growth rates for perturbations to a stationary vortex pair we must calculate first the matrix elements $M_{i,j}$, the analytic forms of which can be found in Appendix A.

1.4.3 The stability of the vortex pair behind an elliptical cylinder

In the case where the steady vortices are located behind the vortex as the images of $\zeta_{\pm}^s = r_s \exp(\pm i\theta_s)$, we find at either steady vortex

$$\left|\frac{df(z^s)}{dz}\right|^2 = \frac{\left(\frac{r_s}{a}\right)^4\left(\left(\frac{r_s}{a}\right)^6 - \lambda\right)}{\left(\left(\frac{r_s}{a}\right)^2 - \lambda\right)\left(\left(\frac{r_s}{a}\right)^4 - \lambda\right)^2}. \tag{1.46}$$

Recall that $r_s/a > 1$ for point outside the cylinder. Using the relations which define the location of the steady pair behind the elliptical cylinder (1.31) and the vortex strength (1.32) we are able to calculate the eigenvalues for both the symmetric and asymmetric part of an infinitesimal perturbation. For the case of the circular cylinder, $\lambda = 0$, the eigenvalues reduce to simple forms. The symmetric perturbations are seen

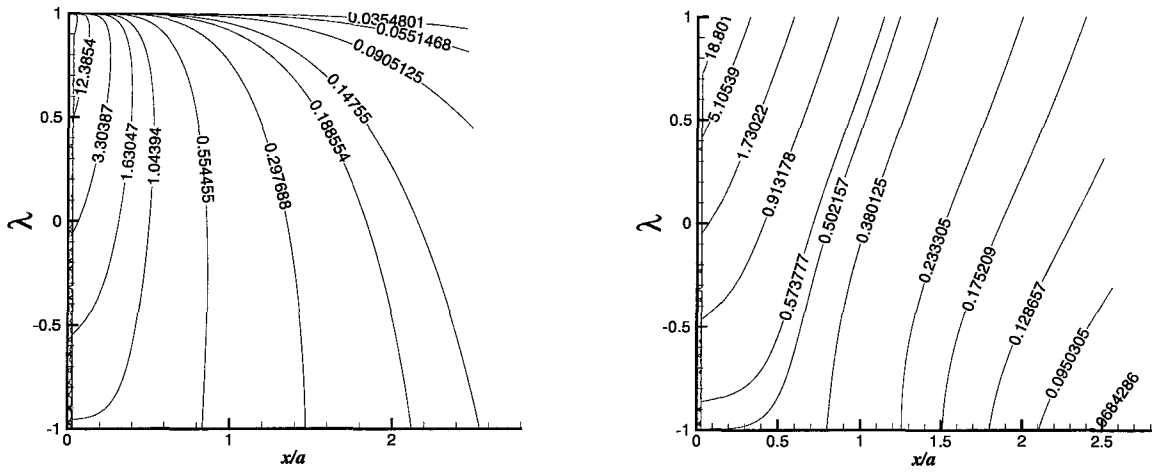

(a) Symmetric frequencies $i\mu$

(b) Asymmetric growth rates μ

Figure 1.4: The growth rates μ nondimensionalized on a/U for the vortex pair behind the cylinder.

to be stable

$$\left(\frac{a}{U}\right)^2 \left(\mu^2_{sym}\right) \Big|_{\lambda=0} = -\frac{(3\left(\frac{r_s}{a}\right)^2 - 1)(\left(\frac{r_s}{a}\right)^4 + 2\left(\frac{r_s}{a}\right)^2 + 5)}{\left(\frac{r_s}{a}\right)^{10}} < 0 \text{ for } r_s/a > 1/\sqrt{3} \quad (1.47)$$

while the asymmetric perturbations are unstable

$$\left(\frac{a}{U}\right)^2 \left(\mu^2_{asym}\right) \Big|_{\lambda=0} = \frac{3\left(\frac{r_s}{a}\right)^2 (\left(\frac{r_s}{a}\right)^4 + \left(\frac{r_s}{a}\right)^2 - 1) + 1}{\left(\frac{r_s}{a}\right)^{10}} > 0 \text{ for all } r_s/a. \quad (1.48)$$

The growth rates for the $\lambda = 0$ case have also recently been calculated by DeLaat and Coene [4].

To examine the response to the perturbations for a general elliptic cylinder ($1 \geq \lambda \geq -1$), we present in Figure 1.4 contour plots of the eigenvalues as functions of the downstream distance of the vortex pair and the ellipticity of the cylinder. By computing the growth rates μ, we find that a steady solution representing a vortex pair behind an elliptical cylinder is always stable to symmetric perturbations and always unstable to perturbations with an asymmetric component. Figure 1.4 (a) is a

contour plot of the frequency $\pm i\mu$ of the stable symmetric perturbations as a function of λ and x - the downstream distance of the vortex pair measured from the back of the cylinder. The growth rates $\pm\mu$ of the unstable asymmetric perturbations are shown in Figure 1.4 (b). The stability to symmetric perturbations is of special interest as it indicates stability for a flow in which the fluid is confined to the upper half plane with a boundary along the x-axis. In such a case the vortex in the lower half plane is simply the symmetric image.

1.4.4 The stability of the vortex pair centered about an elliptical cylinder

We now turn our attention to the case of the steady vortex pair on the vertical axis of symmetry, about the center of the elliptical cylinder. The steady vortices are located at the images of $\zeta_s = \pm ir_s$. We find that at either vortex

$$\left|\frac{df(z^s)}{dz}\right|^2 = \frac{\left(\frac{r_s}{a}\right)^4}{\left(\left(\frac{r_s}{a}\right)^2+\lambda\right)^2}. \tag{1.49}$$

Using the relation (1.33), which defines the vortex strength, we calculate the growth rates for an infinitesimal perturbation. For the circular cylinder, $\lambda = 0$, the growth rates have the simple forms

$$\left(\frac{a}{U}\right)^2 \left(\mu^2_{sym}\right)_{\lambda=0} = 2\frac{\left(3\left(\frac{r_s}{a}\right)-1\right)\left(\left(\frac{r_s}{a}\right)^8+10\left(\frac{r_s}{a}\right)^6-8\left(\frac{r_s}{a}\right)^4+14\left(\frac{r_s}{a}\right)^2-1\right)}{\left(\frac{r_s}{a}\right)^6\left(\left(\frac{r_s}{a}\right)^4+4\left(\frac{r_s}{a}\right)^2-1\right)^2} \tag{1.50}$$

and

$$\left(\frac{a}{U}\right)^2 \left(\mu^2_{asym}\right)_{\lambda=0} = 2\frac{\left(3\left(\frac{r_s}{a}\right)^6+\left(\frac{r_s}{a}\right)^4+5\left(\frac{r_s}{a}\right)^2-1\right)}{\left(\frac{r_s}{a}\right)^6\left(\left(\frac{r_s}{a}\right)^4+4\left(\frac{r_s}{a}\right)^2-1\right)}; \tag{1.51}$$

notice that these quantities are positive for points outside the cylinder ($r_s/a > 1$). Any perturbation to the steady configuration will be unstable.

We present in Figure 1.5 contour plots of the eigenvalues as functions of the ellip-

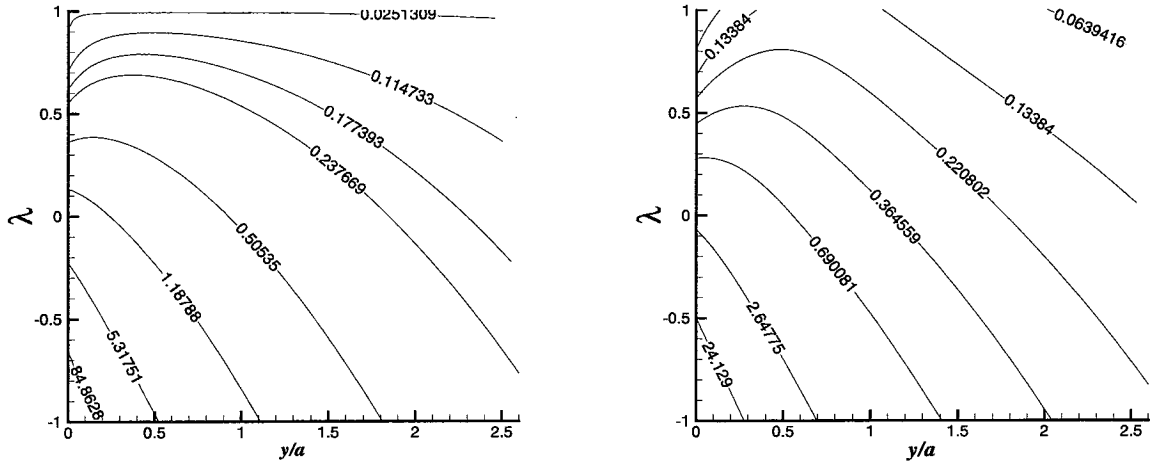

(a) Symmetric growth rates μ

(b) Asymmetric growth rates μ

Figure 1.5: The growth rates μ nondimensionalized on a/U for the pair centered about an elliptical cylinder. All perturbations are unstable

ticity of the cylinder and the vertical distance of a vortex measured from the boundary. By computing the growth rates μ we find that a steady solution representing a vortex centered about the elliptical cylinder is unstable to any two dimensional perturbations of the vortex locations. Figure 1.5 (a) is a contour plot of the growth rates $\pm\mu$ of the symmetric perturbations as a function of λ and y - the vertical distance of a vortex measured from the top of the cylinder. The growth rates $\pm\mu$ of the unstable asymmetric perturbations are shown in Figure 1.5 (b).

1.5 The nonlinear trajectories of the symmetrically located vortex pair

Given parallel flow at infinity aligned along the x-axis and given the elliptic cylinder centered at the origin and symmetric about the x-axis, a vortex pair also initially symmetric about the x-axis will remain so in the absence of any external asymmetric perturbations. This symmetric development also reflects the motion of a single vortex

when the x-axis is considered to be a wall. In the previous section we found steady locations of the symmetric vortex pair in the presence of an elliptic cylinder and performed linear perturbation analysis to study the stability. We found the steady locations for the vortex pair behind the ellipse to be stable to infinitesimal symmetric perturbations, but the stationary vortex pair centered about the ellipse was shown to be unstable to such perturbations. We now produce the trajectories that a symmetric vortex pair will follow under the full evolution equations from an arbitrary symmetric initial locations. It should be mentioned that while some such trajectories for the case of a circular cylinder have been numerically calculated by time integrating the nonlinear equations (DeLaat and Coene [4]), our intention, after consideration of the kinetic energy, is to present an analytic function which defines the trajectories.

We construct a conserved function with Hamiltonian characteristics which represents the finite part of the energy of the flow for this time evolving system. Such a function for point vortex evolution is known as a Kirchhoff-Routh function (see Saffman [32]) or Routh's stream function (see Milne-Thompson [17]). Given the initial strength and location of a symmetric vortex pair behind an elliptical cylinder, it will be an easy matter to determine if the pair will remain with the cylinder while orbiting the steady solution behind the cylinder, be convected permanently away from the cylinder, or overtake the cylinder and continue upstream.

We begin with a derivation of the Kirchhoff-Routh function, followed by a construction of the path function for the case of two point vortices in the presence of a circular cylinder. We then use that result to formulate the Kirchhoff-Routh function for the more general case involving an elliptic cylinder.

1.5.1 The Kirchhoff-Routh function

We can quickly derive the Kirchhoff-Routh function for the case of a flow with N point vortices in the presence of a stationary body. Saffman [32] has shown that in the absence of a background flow, the finite part of the kinetic energy can be identified as the Kirchhoff-Routh function. To generalize this result, we show that

with the addition of a time-independent background flow ψ_o the finite part of the energy is still conserved and takes the form of the Kirchhoff-Routh function.

Using complex notation, $z = x + iy$, we take the time dependent locations of the vortices to be $z_r(t)$ with strength κ_r. The stream function for such a flow has the general form

$$\psi(z, \overline{z}, t) = \psi_o(z, \overline{z}) + \psi_v(z, \overline{z}, t) \tag{1.52}$$

with

$$\psi_v(z, \overline{z}, t) = \sum_r^N \kappa_r G(z, \overline{z} | z_r(t), \overline{z}_r(t)) \tag{1.53}$$

and

$$G(z, \overline{z} | z_r(t), \bar{\zeta}_r(t)) = \frac{-1}{2\pi} \log |z - z_r(t)| + g(z, \overline{z} | z_r(t), \overline{z}_r(t)); \tag{1.54}$$

The function ψ_o is a time-independent irrotational flow about the body with the boundary conditions $\psi_o = 0$ on the body surface ∂B and ψ_o tending to parallel flow at infinity. The term ψ_v represents the flow due to the point vortices. In the fluid domain $G(z, \overline{z} | z_r, \overline{z}_r)$ is the Green's function representing a point vortex at z_r with the conditions $G(z, \overline{z} | z_r, \overline{z}_r) = 0$ on the body surface and $g(z, \overline{z} | z_r, z_r)$ tending to a constant at infinity.

We calculate the kinetic energy $(K.E.)$ of the flow and examine the evolution of its finite part. Integrating over the fluid, the kinetic energy is given by

$$K.E. = \frac{1}{2} \int_{all\ fluid} \left(u^2 + v^2\right)\, dA \tag{1.55}$$

$$= \frac{1}{2} \int_{all\ fluid} \vec{\nabla}\psi \cdot \vec{\nabla}\psi\, dA. \tag{1.56}$$

We subtract the time-independent (and possibly divergent) kinetic energy of the background flow and define the resulting energy as T;

$$T = \frac{1}{2} \int_{all\ fluid} \vec{\nabla}\psi \cdot \vec{\nabla}\psi\, dA - \frac{1}{2} \int_{all\ fluid} \vec{\nabla}\psi_o \cdot \vec{\nabla}\psi_o\, dA \tag{1.57}$$

$$= \int\limits_{all\ fluid} \vec{\nabla}\psi_o \cdot \vec{\nabla}\psi_v \, dA + \frac{1}{2} \int\limits_{all\ fluid} \left(\vec{\nabla}\psi_v\right)^2 \, dA. \tag{1.58}$$

An application of Green's formula gives boundary integrals over the arc at infinity and over the body as well as an area integration;

$$\begin{aligned} T &= \lim_{R\to\infty} \oint\limits_{|z|=R} \psi_o \frac{\partial \psi_v}{\partial n} ds - \oint\limits_{\partial B} \psi_o \frac{\partial \psi_v}{\partial n} ds - \int\limits_{all\ fluid} \psi_o \nabla^2 \psi_v \, dA \\ &+ \frac{1}{2} \left(\lim_{R\to\infty} \oint\limits_{|z|=R} \psi_v \frac{\partial \psi_v}{\partial n} ds - \oint\limits_{\partial B} \psi_v \frac{\partial \psi_v}{\partial n} ds - \int\limits_{all\ fluid} \psi_v \nabla^2 \psi_v \, dA \right). \end{aligned} \tag{1.59}$$

The boundary conditions for the background streamfunciton ψ_o and the vortex streamfunction ψ_v imply that the boundary integrals contribute nothing. The remaining area integration may be calculated;

$$\begin{aligned} T &= -\int\limits_{all\ fluid} \left(\psi_o + \frac{1}{2}\psi_v\right) \nabla^2 \psi_v \, dA \\ &= \sum_j^N \kappa_j \psi_o(z_j(t), \overline{z}_j(t)) + \frac{1}{2} \sum_j^N \kappa_j \psi_j(z_j(t), \overline{z}_j(t)) \\ &= \sum_r^N \kappa_r \psi_o(z_r(t), \overline{z}_r(t)) + \frac{1}{2} \sum_{j\neq k}^N \sum_k^N \kappa_j \kappa_k G(z_j, \overline{z}_j | z_k, \overline{z}_k) \\ &+ \frac{1}{2} \sum_j^N \kappa_r^2 g(z, \overline{z} | z_r(t), \overline{z}_r(t)) - \frac{1}{2} \lim_{\epsilon\to 0} \sum_r^N \frac{\kappa_r^2}{2\pi} \log \epsilon. \end{aligned} \tag{1.60}$$

The divergent term represents the time-independent infinite kinetic energy due to singular velocities at the points z_r. Subtracting this divergence from T, we identify Ψ as the finite part of the kinetic energy

$$\Psi = \frac{1}{2} \sum_{j\neq k}^N \sum_k^N \kappa_j \kappa_k G(z_j, \overline{z}_j | z_k, \overline{z}_k) + \frac{1}{2} \sum_j^N \kappa_j^2 g(z_j, \overline{z}_j | z_j, \overline{z}_j) + \sum_j^N \kappa_j \psi_o(z_j, \overline{z}_j). \tag{1.61}$$

This quantity Ψ which represents the finite part of the kinetic energy is conserved.

Notice that the velocities of individual vortices may be recovered from Ψ,

$$\frac{dx_j}{dt} = -\frac{1}{\kappa_j}\frac{\partial \Psi}{\partial y_j} \tag{1.62}$$

$$\frac{dy_j}{dt} = \frac{1}{\kappa_j}\frac{\partial \Psi}{\partial x_j}. \tag{1.63}$$

These equations imply that

$$\frac{d\Psi}{dt} = \sum_j \left(\frac{\partial \Psi}{\partial y_j}\frac{dy_j}{dt} + \frac{\partial \Psi}{\partial x_j}\frac{dx_j}{dt} \right) = 0. \tag{1.64}$$

We have shown that an inviscid fluid in the presence of a body moving with fixed speed (corresponding to a time-independent background flow ψ_o) conserves kinetic energy. For a given flow, Ψ is known as the corresponding Kirchhoff-Routh function. If one re-writes equations, (1.62) and (1.63) with the notational change $q_j = \sqrt{|\kappa_j|}x_j$ and $p_j = \sqrt{|\kappa_j|}y_j$, then Ψ is interpreted as a Hamiltonian.

1.5.2 The trajectories about a circular cylinder

For the case of point vortices in the presence of a circular cylinder of radius a, the stream function due to both the background ψ_o and the presence of point vortices, located at z_r with strength κ_r, is given by

$$\psi(z, \bar{z}) = \psi_o(z, \bar{z}) + \sum_r \kappa_r G(z, \bar{z}|z_r, \bar{z}_r) \tag{1.65}$$

where

$$G(z, \bar{z}|z_r, \bar{z}_r) = \frac{-1}{2\pi}\left(\log|z - z_r| - \frac{1}{2}\log((1 - \frac{a^2}{\bar{z}_r z})(1 - \frac{a^2}{z_r \bar{z}})) \right) \tag{1.66}$$

and

$$\psi_o(z, \bar{z}) = \frac{U}{2i}(z + \frac{a^2}{z} - \bar{z} - \frac{a^2}{\bar{z}}) \tag{1.67}$$

with $z = x + iy$ and the overbar denoting complex conjugation.

The path function (i.e. the Hamiltonian) can now be constructed:

$$\Psi = \sum_s \kappa_s(\psi_s + \frac{1}{2}\kappa_s g_s) \tag{1.68}$$

where

$$\psi_s = \psi_o(z_s, \bar{z}_s) + \frac{1}{2}\sum_{r\neq s} \kappa_r\kappa_s G(z_r, \bar{z}_r|z_s, \bar{z}_s) \tag{1.69}$$

and

$$g_s = \lim_{z\to z_s}\left[G(z, \bar{z}|z_s, \bar{z}_s) + \frac{1}{2\pi}\log|z - z_s|\right]. \tag{1.70}$$

We are interested in the problem of only two point vortices; the locations given by z_1 and z_2 and with the corresponding strengths κ_1 and κ_2. In this case the Kirchhoff-Routh function has a simple form;

$$\begin{aligned}\Psi\left(z_1, \bar{z}_1|z_2, \bar{z}_2\right) &= \kappa_1\psi_o\left(z_1, \bar{z}_1\right) + \kappa_2\psi_o\left(z_2, \bar{z}_2\right) \\ &\quad -\frac{1}{2\pi}\left(\kappa_1\kappa_2\right)\left\{\log|z_2 - z_1| - \log\left|1 - \frac{a^2}{z_1\bar{z}_2}\right|\right\} \\ &\quad +\frac{1}{4\pi}\kappa_1^2\log\left(1 - \frac{a^2}{|z_1|^2}\right) + \frac{1}{4\pi}\kappa_2^2\log\left(1 - \frac{a^2}{|z_2|^2}\right).\end{aligned} \tag{1.71}$$

And for the case of the symmetric vortex pair, we say $z_1 = \bar{z}_2$ and $\kappa \equiv \kappa_1 = -\kappa_2$ with the flow parallel to the x-axis. Calling the symmetric Routh path function Ψ_s we find

$$\begin{aligned}\Psi_s &= 2Uy\kappa\left(1 - \frac{a^2}{x^2 + y^2}\right) + \frac{\kappa^2}{2\pi}\log|2y| + \frac{\kappa^2}{2\pi}\log\left|1 - \frac{a^2}{x^2 + y^2}\right| \\ &\quad -\frac{1}{2}\frac{\kappa^2}{2\pi}\log\left|\frac{\left(x^2 - y^2 - a^2\right)^2 + 4x^2y^2}{\left(x^2 + y^2\right)^2}\right|\end{aligned} \tag{1.72}$$

where $z_1 = x + iy$. Relating Ψ_s to Ψ one finds

$$u_1 = -\frac{1}{2\kappa}\frac{\partial\Psi_s}{\partial y}, \tag{1.73}$$

$$v_1 = \frac{1}{2\kappa}\frac{\partial \Psi_s}{\partial x}. \tag{1.74}$$

1.5.3 The trajectories about an elliptical cylinder

To generalize the Kirchhoff-Routh function for the case of an elliptic cylinder, we choose to use conformal mapping techniques. As earlier, we use the Joukowski transformation pair. Recall

$$z = \zeta + \lambda\frac{a^2}{\zeta} \tag{1.75}$$

maps a circle to an ellipse, while its inverse

$$\zeta = \frac{1}{2}\left(z + \sqrt{z^2 - 4a^2\lambda}\right) \tag{1.76}$$

takes the region outside of an ellipse to the area outside a circle. The branch cut is chosen to be contained within the ellipse. The z-plane will be the physical plane, in which the boundary of our body is an ellipse, while in the non-physical plane (the ζ-plane) the boundary is circular. We require λ be real so that the ellipse will have major and minor axis aligned on the co-ordinate axis. When $\lambda = -1$ a circle of radius a will be mapped to a flat plate on the y-axis, while $\lambda = 1$ maps the circle to a flat plate on the x-axis.

In order to construct the Kirchhoff-Routh function in the z-plane, let $\Gamma(z_1, \bar{z}_1|z_2, \bar{z}_2)$ be the Green's Function in the z-plane and $G(\zeta_1, \bar{\zeta}_1|\zeta_2, \bar{\zeta}_2)$ its image in the ζ-plane. Define γ and g as the additional harmonic parts of the stream function required to satisfy boundary conditions; so that we may write

$$\Gamma(z_1, \bar{z}_1|z_2, \bar{z}_2) = \gamma(z_1, \bar{z}_1|z_2, \bar{z}_2) - \frac{1}{2\pi}\log|z_1 - z_2| \tag{1.77}$$

and

$$G(\zeta_1, \bar{\zeta}_1|\zeta_2, \bar{\zeta}_2) = g(\zeta_1, \bar{\zeta}_1|\zeta_2, \bar{\zeta}_2) - \frac{1}{2\pi}\log|\zeta_1 - \zeta_2|. \tag{1.78}$$

Since the Green's function in the ζ-plane is simply the map of the Green's function

in the z-plane, if we let ζ_1 tend to the image of z_1 we find

$$g(\zeta_1, \overline{\zeta}_1|\zeta_1, \bar{\zeta}_1) = \gamma(z_1, \bar{z}_1|z_1, \bar{z}_1) - \frac{1}{2\pi}\log|\frac{dz_1}{d\zeta_1}|. \tag{1.79}$$

With this in mind the path function for the case of two point vortices in the presence of an ellipse becomes

$$\begin{aligned}\Psi\left(z_1, \overline{z}_1|z_2, \overline{z}_2\right) &= \kappa_1\psi_o\left(\zeta_1, \overline{\zeta}_1\right) + \kappa_2\psi_o\left(\zeta_2, \overline{\zeta}_2\right) \\ &\quad -\frac{\kappa_1\kappa_2}{2\pi}\left(\log|\zeta_1 - \zeta_2| - \log\left|1 - \frac{a^2}{\zeta_1\overline{\zeta}_2}\right|\right) \\ &\quad +\frac{\kappa_1^2}{4\pi}\left(\log\left|\frac{dz_1}{d\zeta_1}\right| + \log\left|1 - \frac{a^2}{|\zeta_1|^2}\right|\right) \\ &\quad +\frac{\kappa_2^2}{4\pi}\left(\log\left|\frac{dz_2}{d\zeta_2}\right| + \log\left|1 - \frac{a^2}{|\zeta_2|^2}\right|\right).\end{aligned} \tag{1.80}$$

We are interested in the special case of a vortex pair symmetrically located behind a cylinder, $z_1 = \overline{z}_2$ and $\kappa \equiv \kappa_1 = -\kappa_2$. Call this path function Ψ_s, then

$$\begin{aligned}\Psi_s\left(z_1, \overline{z}_1\right) &= \kappa\left(\psi_o\left(\zeta_1, \overline{\zeta}_1\right) - \psi_o\left(\overline{\zeta}_1, \zeta_1\right)\right) \\ &\quad +\frac{\kappa^2}{2\pi}\left(\log|\zeta_1 - \overline{\zeta}_1| - \log\left|1 - \frac{a^2}{\zeta_1^2}\right|\right) \\ &\quad +\frac{\kappa^2}{2\pi}\left(\log\left|\frac{dz_1}{d\zeta_1}\right| + \log\left|1 - \frac{a^2}{|\zeta_1|^2}\right|\right).\end{aligned} \tag{1.81}$$

where, from the map equations (1.75) and (1.76), we see that $\frac{dz_1}{d\zeta_1} = 1 - \lambda a^2/\zeta_1^2$ and $\zeta_1 = \frac{1}{2}\left(z_1 + \sqrt{z_1^2 - 4a^2\lambda}\right)$.

The contours in the Figure 1.6 give the trajectories of a vortex in the upper half plane which is half of a symmetric pair. Due to time reversibility and the physical symmetry of the cylinder, the trajectories are symmetric about the y-axis. The stationary point for the vortex behind the cylinder forms the center of a class of orbiting trajectories. The steady location for the vortex above the cylinder is the saddle point from which the separatrix emanates. The separatrix closes at the points $\{x, y\} = \{\pm\infty, \kappa/(4\pi U)\}$. A vortex pair in unbounded fluid will travel at the speed

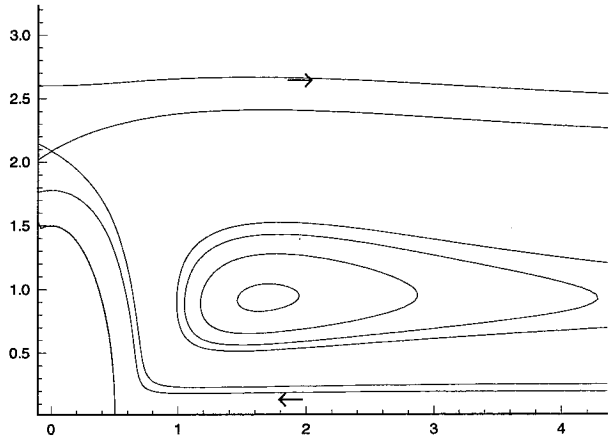

Figure 1.6: The Contours of Hamiltonian for $\kappa = -7/2\pi$, nondimensionalized by the choice $U, a = 1$. The ellipse is defined by $\lambda = -.5$.

$U = \kappa/(2\pi l)$ where l is the separation distance, so the point at infinity where the separatrix closes represents a steady location for the vortex pair which does not see the cylinder. Those trajectories within the separatrix are closed orbits. If the vortex is above the upper branch of the separatrix it will be convected down stream, while it if is below the lower branch of the separatrix the vortex pair will pass about the cylinder and head up stream. We also mention that since we have an analytic location for the saddle point, (1.33) with (1.75), given a vortex strength it is a simple matter to calculate the value of the Hamiltonian which defines the separatrix.

Chapter 2 The Generalization of Föppl Flow to a Vortex Ring Behind a Sphere

2.1 Introduction

In his numerical examination of the time variation of equipressure surfaces in moderate Reynolds number flow past a sphere, Shirayama [34] relates the leading wake instability to a tilting of the ring-like wake. We construct a simple model for the eddy structure observed behind a sphere, and the stability analysis is done with the hope that it may give insight into the convective mechanism that produces the wake shedding.

In this chapter we study the motion of a thin cored vortex ring in the presence of a sphere of radius a moving with constant speed U in an inviscid fluid. The vortex ring itself is a vortex filament with strength Γ and a core radius c_r whose centerline forms a circle of radius R; by "thin cored" we mean that the ratio c_r/R of the core radius to the ring radius is small. While there are many ways in which a vortex ring might interact with a sphere we will limit ourselves to a generalization of Föppl's two dimensional wake model studied in the last chapter. In particular we will be looking for axisymmetric solutions which are steady with respect to the sphere. The linear stability properties of such steady solutions are then analyzed by adding an infinitesimal sinusoidal perturbation to the centerline of the vortex ring and computing associated growth rates.

A circular vortex ring in unbounded flow at rest at infinity will travel in the direction of its axis of symmetry with a speed which depends on its strength, radius, and core radius. The so called self-induced velocity, first calculated in 1867 by Kelvin,

of a uniform finite cored vortex ring is to leading order given by

$$U = \frac{\Gamma}{4\pi R}\left[\log\left(\frac{8R}{c_r}\right) - \frac{1}{4}\right]. \tag{2.1}$$

By taking into account the internal structure of a vortex ring, Saffman [32] used energy considerations to deduce that the speed of a thin cored vortex ring is given by

$$U = \frac{\Gamma}{4\pi R}\left[\log\left(\frac{8R}{c_r}\right) - \frac{1}{2} - \frac{8\pi^2}{\Gamma}\int_o^{c_r} r\left[w\left(r\right)\right]^2 dr + \frac{4\pi^2}{\Gamma^2}\int_o^{c_r} r\left[v\left(r\right)\right]^2 dr\right] \tag{2.2}$$

where w is the swirl velocity and v is radial velocity.

To give an expression for the velocity field $\mathbf{u}$ outside the core of a vortex filament, we first note that, since the flow is incompressible, $\mathbf{u}$ can be represented as the curl of a vector potential $\mathbf{A}$. We assume the velocity field induced by a thin vortex filament is adequately approximated by the field induced by a filament for which all of the vorticity is concentrated on the centerline. Under this assumption the expression for the vector potential at point $\mathbf{P}$, outside of the core, due to the vortex filament is given by a Biot-Savart line integral;

$$\mathbf{A} = \frac{\Gamma}{4\pi}\oint \frac{d\mathbf{s}}{|\mathbf{P} - \mathbf{R}(s,t)|} \tag{2.3}$$

and thus

$$\mathbf{u} = -\frac{\Gamma}{4\pi}\oint \frac{(\mathbf{P} - \mathbf{R}(s,t))}{|\mathbf{P} - \mathbf{R}(s,t)|^3} \times d\mathbf{s}, \tag{2.4}$$

where $\mathbf{R}(s,t)$ is a parameterization of the vortex filament centerline and $\delta\mathbf{s}$ is a line element of the closed curve of integration coincident with the line vortex. To calculate the value of the velocity field at a point on the thin cored filament of a vortex ring, Thomson [37] suggested a cut-off method be used to circumvent the fact that the integral in (2.4) diverges logarithmically as $\mathbf{P}$ approaches a point $\mathbf{R}$ on the curve. In the absence of other flows, the equation for the motion of a point on the filament is given by

$$\frac{\partial \mathbf{R}(s',t)}{\partial t} = -\frac{\Gamma}{4\pi}\int_{[\delta]} \frac{\left(\mathbf{R}(s',t) - \mathbf{R}(s,t)\right)}{|\mathbf{R}(s',t) - \mathbf{R}(s,t)|^3} \times d\mathbf{s} \tag{2.5}$$

where the subscript $[\delta]$ indicates that a section of length $2\delta c_r$ centered on the point $\mathbf{R}(s',t)$ has been removed from the range of integration. When used to calculate the velocity of a ring, equation (2.5) gives

$$\begin{aligned} U &= \frac{\Gamma}{8\pi R}\log\left(\frac{1+\cos\left(\delta\frac{c_r}{2R}\right)}{1-\cos\left(\delta\frac{c_r}{2R}\right)}\right) \\ &= \frac{\Gamma}{4\pi R}\left[\log\left(\frac{8R}{c_r}\right)-\frac{1}{2}\log\left(\left(\frac{8R}{c_r}\right)^2\frac{1-\cos\left(\delta\frac{c_r}{2R}\right)}{1+\cos\left(\delta\frac{c_r}{2R}\right)}\right)\right] \end{aligned} \tag{2.6}$$

which when $\delta c_r/R$ is small has the leading order form

$$U=\frac{\Gamma}{4\pi R}\left[\log\left(\frac{8R}{c_r}\right)-\log\left(2\delta\right)\right]. \tag{2.7}$$

A comparison with the velocity (2.2) may be made to determine the correct cut-off value δ for a given internal structure.

As a result of their higher order theory for filament motion, Moore and Saffman [21] showed that the cut-off approximation is a dynamically consistent method for describing the motion of thin cored filaments in the case that the cut-off length is prescribed by the internal structure of the filaments as

$$\log\left(2\delta\right)=\frac{1}{2}+\frac{8\pi^2}{\Gamma}\int_o^{c_r} r\left[w\left(r\right)\right]^2dr-\frac{4\pi^2}{\Gamma^2}\int_o^{c_r} r\left[v\left(r\right)\right]^2dr \tag{2.8}$$

where δc_r is small compared to the local radius of curvature of the centerline. A uniform core without swirl implies $v\left(r\right)\simeq \Gamma r/\left(2\pi c_r^2\right)$ from which one calculates $\log\left(2\delta\right)=1/4$ in agreement with expression (2.1); for a stagnant core one finds $\log\left(2\delta\right)=1/2$.

We shall not assume any specific internal structure in this chapter; our results will be equally applicable to all core structures which satisfy certain compatibility criteria. In particular, for a given steady vortex ring location we will calculate a value for the ratio $\delta c_r/R$; our work will only be applicable to core structures (i.e., δs) such that c_r/R is small. In order to use the cut-off equation in our stability analysis we will also require that the perturbation wavelength be large compared to $2\delta c_r$, the cut-off

length.

2.2 Steady configurations

2.2.1 The axisymmetric flow

In looking for a steady configuration of the vortex ring behind a moving sphere of radius a, we define a cylindrical polar coordinate system (ρ, ϕ, z), with ρ radial, ϕ azimuthal, and z axial. The corresponding velocity components are (v, w, u). The origin is taken to be the center of the sphere and the positive z-direction points downstream. The center of the vortex ring will be located a distance Z downstream, so the centerline of the ring will be located on the curve (R, ϕ, Z). Since the steady solutions we are seeking are axisymmetric and swirl-free outside the filament, the corresponding vector potential has one nonzero entry,

$$\mathbf{A} = \left(0, \frac{\psi}{\rho}, 0\right). \tag{2.9}$$

From the function ψ, known as Stokes stream function, velocities are readily available:

$$u = \frac{1}{\rho}\frac{\partial \psi}{\partial \rho}, \tag{2.10}$$

$$v = \frac{-1}{\rho}\frac{\partial \psi}{\partial z}. \tag{2.11}$$

To create the streamfunction for our configuration, we combine the simple irrotational flow past a sphere, the flow induced by a vortex ring in unbounded fluid and a flow referred to as an image. The image is that irrotational flow which balances the flow induced by the vortex ring across the sphere's surface and decays to zero for large distances from the sphere.

In the absence of the vortex ring,

$$\psi_{bg} = U\frac{\rho^2}{2}\left(1 - \frac{a^3}{(\rho^2 + z^2)^{3/2}}\right) \tag{2.12}$$

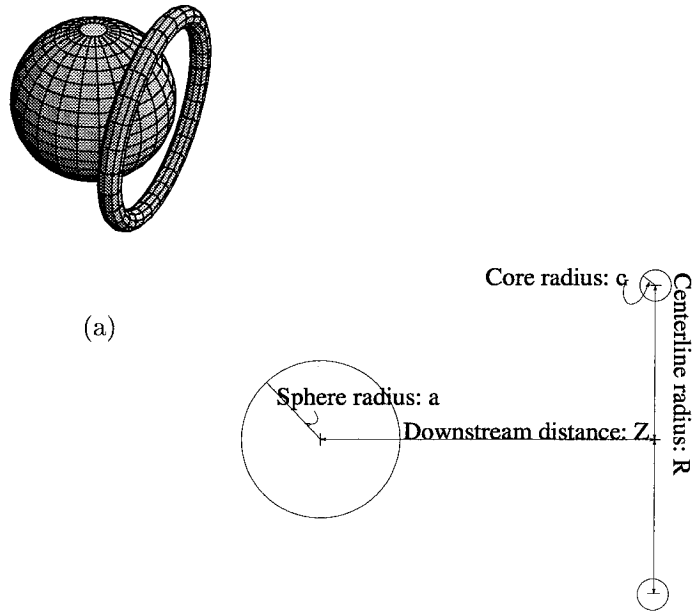

Figure 2.1: A sketch and cross section of a axisymmetric vortex ring and sphere.

gives the irrotational flow past the sphere. We shall refer to this as the background flow; hence the subscript bg.

To calculate the velocity field due to a thin vortex ring of radius R in unbounded fluid a distance Z down stream from the origin, we make the following substitutions in expression (2.3) for the vector potential $\mathbf{A}$:

$$|\mathbf{P} - \mathbf{R}(s,t)| = \sqrt{(z-Z)^2 + \rho^2 + R^2 - 2\rho R\cos\left(\phi - \phi'\right)} \tag{2.13}$$

$$d\mathbf{s} = \mathbf{e}_{\boldsymbol{\phi}} R\cos\left(\phi - \phi'\right) d\phi' + \mathbf{e}_{\boldsymbol{\rho}} R\sin\left(\phi - \phi'\right) d\phi'. \tag{2.14}$$

The integrand in the $\mathbf{e}_{\boldsymbol{\rho}}$ direction is odd and sums to zero. We find the Stokes stream function due the vortex ring has the simple form

$$\psi_{vortex}(z,\rho) = \frac{\Gamma\rho R}{4\pi}\int_o^{2\pi} \frac{\cos\theta}{\sqrt{(z-Z)^2 + \rho^2 + R^2 - 2\rho R\cos\theta}} d\theta. \tag{2.15}$$

Such an expression could be represented in terms of elliptic integrals of the 1^{st} and

2^{nd} kind.

As discussed in Saffman's "Vortex Dynamics," a distribution of vorticity can be prescribed within the sphere in such a way that it serves as an image system for any vorticity outside the sphere. That is to say it preserves the physical boundary condition of no flow across the surface the sphere. Ordinarily such an image system is quite complicated; but in the case of a circular line vortex which lies on a spherical surface concentric with our physical sphere, the image system can be constructed as an axisymmetric vortex ring inside the sphere. This image ring has its vorticity concentrated on its own centerline with strength Γ'. The image ring is located on the curve $\left(R', \phi, Z'\right)$ where the quantities are related to the physical vortex ring by

$$R' = R\frac{a^2}{Z^2 + R^2} \tag{2.16}$$

$$Z' = Z\frac{a^2}{Z^2 + R^2} \tag{2.17}$$

$$\Gamma' = -\Gamma\sqrt{\frac{R}{R'}}. \tag{2.18}$$

Accordingly we find the stream function due to the image;

$$\psi_{image}\left(z, \rho\right) = -\frac{\Gamma\rho Ra}{4\pi\sqrt{Z^2 + R^2}}\int_o^{2\pi}\frac{\cos\theta}{\sqrt{(z - Z')^2 + \rho^2 + R'^2 - 2\rho R'\cos\theta}}d\theta. \tag{2.19}$$

It is simple matter to check that $\psi_{vortex} + \psi_{image} = 0$ for points on the surface of the sphere.

Combining the stream functions for irrotational flow past a sphere, the ring induced flow and the image system, gives the Stokes stream function for our system:

$$\psi = \psi_{bg} + \psi_{vortex} + \psi_{image.} \tag{2.20}$$

The velocities are given by the relations $u = \left(\partial\psi/\partial\rho\right)/\rho$ and $v = -\left(\partial\psi/\partial z\right)/\rho$, at a point on the filament of the thin cored vortex ring the cut-off equation is employed in evaluating the contributions from ψ_{vortex}.

2.2.2 Computation of steady configurations

In order to arrive at the equations which govern the axisymmetric interaction of a thin cored ring with a sphere, we use expression (2.6) for the self-induced velocity of the ring. Recall that this velocity corresponds to the leading order approximation to the cut-off integration for a ring. Under this approximation the downstream location Z and radius R of the centerline of the ring evolve according to the equations

$$\begin{aligned} \frac{dZ}{dt} &= \frac{1}{R}\frac{\partial}{\partial \rho}\left(\psi_{bg}(R,Z)+\psi_{image}(R,Z)\right) \\ &\quad +\frac{\Gamma}{8\pi R}\log\left(\frac{1+\cos\left(\delta\frac{c_r}{2R}\right)}{1-\cos\left(\delta\frac{c_r}{2R}\right)}\right) \end{aligned} \tag{2.21}$$

$$\frac{dR}{dt} = -\frac{1}{R}\frac{\partial}{\partial z}\left(\psi_{bg}(R,Z)+\psi_{image}(R,Z)\right). \tag{2.22}$$

To conserve the volume of the thin cored ring, we also require $R(t)\ c_r^2(t) = const.$

A steady configuration satisfies the following equations:

$$0 = \frac{1}{R}\frac{\partial \psi_{bg}}{\partial \rho}+\frac{1}{R}\frac{\partial \psi_{image}}{\partial \rho}+\frac{\Gamma}{8\pi R}\log\left(\frac{1+\cos\left(\delta\frac{c_r}{2R}\right)}{1-\cos\left(\delta\frac{c_r}{2R}\right)}\right) \tag{2.23}$$

$$0 = \frac{1}{R}\frac{\partial \psi_{bg}}{\partial z}+\frac{1}{R}\frac{\partial \psi_{image}}{\partial z}. \tag{2.24}$$

For a given background flow speed U and sphere radius a, our approach is to choose a steady ring location Z and radius R and to use equations (2.23) and (2.24) to calculate the strength Γ of the vortex ring and its corresponding core radius c_r. In order to be consistent with our approximate self-induced ring velocity, c_r/R must be small.

From equation (2.24) we find a relationship between the strength Γ of a steady vortex ring and the speed U of the fluid at infinity; particularly their ratio is a function of ring location Z and radius R,

$$\frac{aU}{\Gamma} = -\frac{d^2\left(Z^2+R^2\right)^{5/2}}{6a\pi}\int_o^{2\pi}\frac{\cos\theta}{\left(d^4+2a^2R^2(1-\cos\theta)\right)^{3/2}}d\theta, \tag{2.25}$$

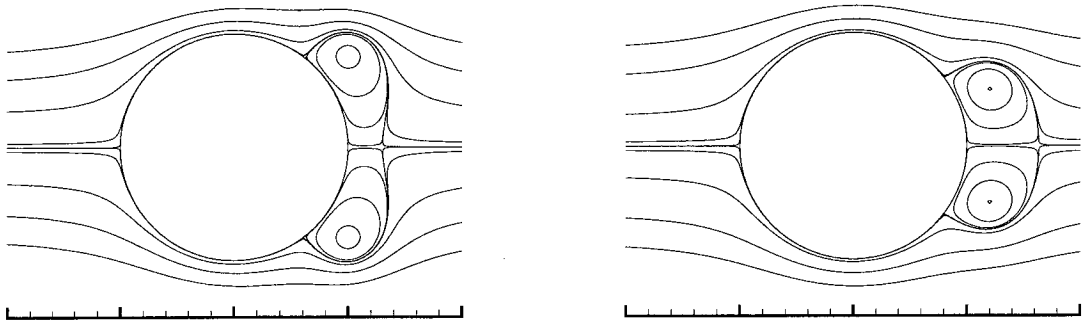

(a) $\delta c_r/R = 0.097$, $\Gamma/(Ua) = -2.094$ (b) $\delta c_r/R = 0.411$, $\Gamma/(Ua) = -2.110$

Figure 2.2: Streamlines for a steady vortex ring behind a sphere. Swirl is required in (b) for the ring to be thin cored.

where $d^2 = R^2 + Z^2 - a^2$. We calculate the corresponding value of c_r/R from equation (2.23);

$$\log\left(\frac{1-\cos\left(\delta\frac{c_r}{2R}\right)}{1+\cos\left(\delta\frac{c_r}{2R}\right)}\right) = \frac{8\pi}{\Gamma}\left(\frac{\partial\psi_{bg}}{\partial\rho} + \frac{\partial\psi_{image}}{\partial\rho}\right), \tag{2.26}$$

or more specifically as a function of R and Z

$$\delta\frac{c_r}{R} = 2\arccos\left[\frac{1-f}{1+f}\right] \tag{2.27}$$

where

$$\begin{aligned}\log(f) &= 8\pi\frac{U}{\Gamma}R\left(1 + \frac{3a^3R^2}{2\left(Z^2+R^2\right)^{5/2}} - \frac{a^3}{\left(Z^2+R^2\right)^{3/2}}\right) - \\ &\quad 2aR\int_o^{2\pi}\frac{\cos\theta\left(\left(Z^2-a^2\right)^2 + R^2\left(Z^2 - a^2\cos\theta\right)\right)}{\left(d^4 + 2a^2R^2(1-\cos\theta)\right)^{3/2}}d\theta.\end{aligned} \tag{2.28}$$

Recall that aU/Γ is a function of R and Z by expression (2.25).

The vortex strength Γ and core radius c_r of steady rings are plotted as functions of R and Z; Figures 2.3 (a) and (b). Since we are considering a wake model, we

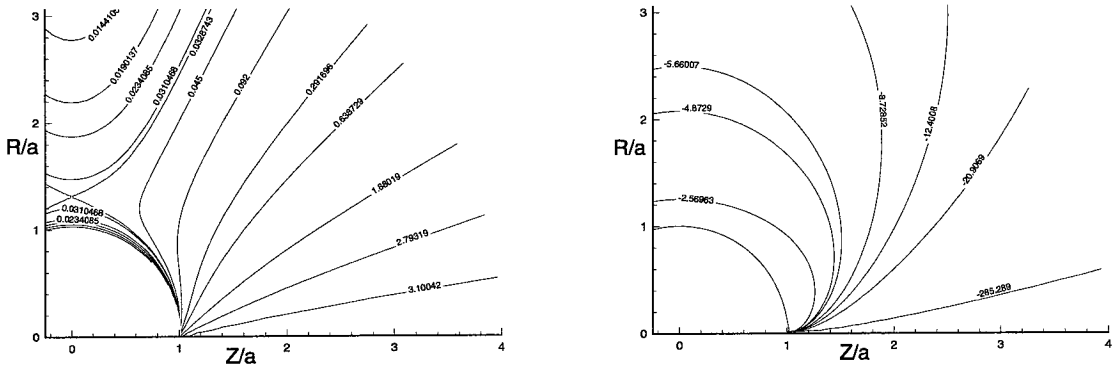

(a) $\delta c_r/R$ (b) $\Gamma/(Ua)$

Figure 2.3: The core size and strength of a steady vortex ring behind a sphere.

have only plotted these quantities for positive downstream distances Z. Obviously the time-reversibility of the Euler equations implies that there are corresponding upstream values.

Recall as defined in equation (2.8), the cut-off ratio δ is dependent on the internal structure of the filament; e.g. $\delta = \exp(1/4)/2$ for a uniform core. From the contour plot of $\delta c_r/R$ we may check the criterion that c_r/R be small for a given core structure; such locations correspond to consistent solutions of our system. Since $2\delta c_r$ is the cut-off distance in calculating the induced velocity, the corresponding angle $2\delta c_r/R$ must be less than 2π. From and examination of Figure 2.3, we see that in much of the area behind the sphere the cut-off angle $2\delta c_r/R$ is relatively large. A ring in this area may only be thin cored if δ is large, implying a large swirl velocity inside the ring.

2.3 Stability analysis

2.3.1 Formulation of the stability problem

Before proceeding to address the stability of our configuration we note that Thomson [37] first investigated the stability of a thin cored vortex ring in unbounded fluid to infinitesimal sinusoidal perturbations of its centerline. In his analysis, consistent to

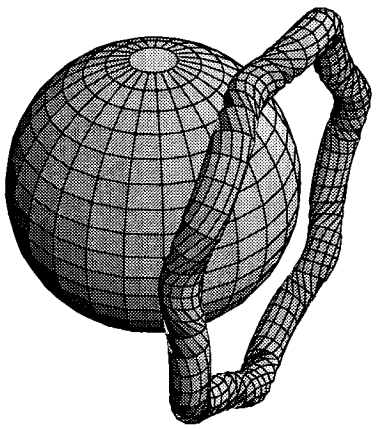

Figure 2.4: A sketch of a perturbed vortex ring and sphere.

$O\left(\ln\left(c_r/R\right)\right)$, he concluded that rings were stable to disturbances in which nc_r/R is small, where n is the number of waves on the ring of radius R. Widnall and Sullivan [43] employed the cut-off equation to examine the same stability problem; their analysis included terms of $O\left(1\right)$. Widnall and Sullivan found instability only for perturbation wavelengths too small to be consistent with the use of the cut-off approximation. It should be mentioned that later, through the work of Widnall, Bliss and Tsai [42],[44] and of Moore and Saffman [22], a short-wave co-operative instability was identified. By a construction of a suitable image system and utilization of the results of Widnall and Sullivan [43], Lough [9] shows that a vortex ring in a pipe is subject to a symmetry breaking tilting instability. Following a similar approach, we shall show that a vortex ring behind a sphere is unstable to a tilting perturbation.

In this section we study the response of a thin cored vortex ring behind a sphere to infinitesimal sinusoidal perturbations of its centerline. We limit our attention to perturbation wavelengths consistent with the cut-off equation. In cylindrical polar coordinates the vector to a point on the perturbed vortex filament is given by

$$\mathbf{R} = \left(R + \epsilon r_o e^{in\theta}\right) \mathbf{e}_\mathbf{r}\left(\theta\right) + \left(Z + \epsilon \zeta_o e^{in\theta}\right) \mathbf{e}_z, \tag{2.29}$$

where the origin is at the center of the sphere and $\vec{e}_z$ points downstream.

In order to derive the linearized evolution equations for the location and shape of the vortex filament, we begin by examining the general velocity field. As in the steady calculations, the field can be considered to be the sum of three parts: the flow induced by the vortex, the background flow past the sphere, and the flow induced by the image system. Since the Stokes stream function can not account for non-axisymmetric terms introduced in the flow by the perturbations, we choose to represent the background flow past the sphere and the contribution from the image system as the gradient of a scalar potential field φ. The velocity at some point $\mathbf{P}$ outside the vortex core is given by

$$\mathbf{u}(\mathbf{P}) = -\frac{\Gamma}{4\pi}\oint \frac{(\mathbf{P}-\mathbf{R}_*)}{|\mathbf{P}-\mathbf{R}_*|}\times d\mathbf{s}_* + \boldsymbol{\nabla}\varphi. \tag{2.30}$$

The scalar field φ is determined by requiring that, when evaluated at the surface of the sphere, the normal component of $\mathbf{u}$ is zero, $\mathbf{u}$ tends to parallel flow at infinity, and $\nabla^2\varphi = 0$ in the fluid.

To calculate the velocity of a point on the vortex filament ($\mathbf{P}$ goes to a point $\mathbf{R}$ on the centerline) we must replace $\oint$ by the cut-off $\int_{[\delta]}$. For such an approximation to be valid, the perturbation wavelength $2\pi R/n$ must be much longer than the cut-off distance $2\delta c_r$.

To order ϵ , the potential may be written as

$$\varphi = \varphi_{bg}(z,\rho) + \varphi_i(z,\rho) + \epsilon e^{in\theta}\left\{r_o\varphi_{r,n}(z,\rho) + \zeta_o\varphi_{\zeta,n}(z,\rho)\right\} + O\left(\epsilon^2\right) \tag{2.31}$$

where

$$\varphi_{bg} = Uz\left(1 + \frac{a^3}{2\left(z^2+\rho^2\right)^{3/2}}\right) \tag{2.32}$$

is the background flow past a sphere and φ_i accounts for the leading order image flow. We note that the potentials φ_{bg} and φ_i are equivalent to the Stokes streamfunction ψ_{bg} and ψ_{image} defined by equations (2.12) and (2.19). The computation of the image corrections, $\varphi_{r,n}$ and $\varphi_{\zeta,n}$, is described in Appendix B. They are obtained by imposing

the boundary condition of no flow into the sphere:

$$\frac{\partial \varphi}{\partial r} = \frac{\Gamma}{4\pi}\mathbf{n}_r \cdot \oint \frac{(\mathbf{P}-\mathbf{R}_*)}{|\mathbf{P}-\mathbf{R}_*|} \times d\mathbf{s}_*|_{r=a} \tag{2.33}$$

where r is the radial co-ordinate in spherical co-ordinates and $\mathbf{n}_r$ is the normal to the sphere's surface.

2.3.2 The perturbation equation and the calculation of growth rates

In the absence of any background the potential flow or image system, Widnall and Sullivan [43] used the equations of motion resulting from the cut-off equation (2.5) in their stability analysis to show that the motion of a point on the filament due only to the velocity induced by a perturbed vortex ring in unbounded fluid obeys

$$\frac{\partial r_o}{\partial t} = Vs\left(\delta\frac{c_r}{R}; n\right)\zeta_o \tag{2.34}$$

$$\frac{\partial \zeta_o}{\partial t} = Us\left(\delta\frac{c_r}{R}; n\right) r_o \tag{2.35}$$

for applicable wavelengths, where the self-induced velocity perturbations are given by

$$\frac{4\pi R^2}{\Gamma}Vs\left(\delta\frac{c_r}{R}; n\right) = F(1) + \frac{1}{2}(n-1)F(n+1) - \frac{1}{2}(n+1)F(n-1) \tag{2.36}$$

$$\begin{aligned}\frac{4\pi R^2}{\Gamma}Us\left(\delta\frac{c_r}{R}; n\right) &= -\frac{3}{2} - \frac{3}{2}F(0) + \frac{1}{2}F(1) \\ &\quad + \frac{1}{2}F(n) + \frac{1}{4}(1-2n)F(n+1) + \frac{1}{4}(1+2n)F(n-1)\end{aligned} \tag{2.37}$$

with

$$F(m) = \frac{1}{\sqrt{2}}\int_{\delta\frac{c_r}{R}}^{\pi} \frac{\cos m\theta}{(1-\cos\theta)^{3/2}} d\theta. \tag{2.38}$$

With the formulation of Widnall and Sullivan in mind, we see that once the potential φ has been determine to order ϵ the equations linearized about a steady

solution take the form

$$\frac{\partial}{\partial t}\begin{pmatrix} r_o \\ \zeta_o \end{pmatrix} = \mathbf{M}\begin{pmatrix} r_o \\ \zeta_o \end{pmatrix} \tag{2.39}$$

with

$$\mathbf{M} = \begin{pmatrix} \frac{\partial^2}{\partial R^2}\left(\varphi_{bg}+\varphi_i\right) + \frac{\partial}{\partial R}\varphi_{r,n} & \frac{\partial^2}{\partial R \partial Z}\left(\varphi_{bg}+\varphi_i\right) + \frac{\partial}{\partial R}\varphi_{\zeta,n} + V_s \\ \frac{\partial^2}{\partial Z \partial R}\left(\varphi_{bg}+\varphi_i\right) + \frac{\partial}{\partial Z}\varphi_{r,n} + U_s & \frac{\partial^2}{\partial Z^2}\left(\varphi_{bg}+\varphi_i\right) + \frac{\partial}{\partial Z}\varphi_{\zeta,n} \end{pmatrix} \tag{2.40}$$

where the matrix entries are evaluated at a steady solution defined by (2.25) and (2.27). Writing $\vec{x}\,(t) = \{r_o, \zeta_o\}^T$, we perform the standard separation of variables, $\vec{x}_n\,(t) = \exp\left(\mu_n t\right)\vec{x}_n\,(0)$, to arrive at the eigenvalue equation

$$\mathbf{M}\vec{x}_n = \mu_n \vec{x}_n. \tag{2.41}$$

The mode of the perturbation is denoted by the subscript n on the eigenvalue. Eigenvalues, μ_n, with positive real parts represent instability.

We anticipate that eigenvalues will come in $\pm$ pairs. Since the matrix is 2×2 the eigenvalues will, from the quadratic equation, have the form

$$\mu_n = \alpha \pm \sqrt{\beta}. \tag{2.42}$$

Furthermore time reversal is equivalent to a reflection about the y-axis for our steady state so that if $\mu_n = \lambda$ is an eigenvalue, so is $\mu_n = -\lambda$, thus $\alpha = 0$.

In order to justify the use of the cut-off equation in evaluating the induced velocities Us and Vs, we restrict our stability analysis to steady solutions in which the cut-off distance $2\delta c_r$ is much smaller that the perturbation wavelengths.

We calculate the first six growth rates at eight different locations indicated in Figure 2.5 and present them in Tables 2.1 and 2.2. We find that the ring is always stable to an axisymmetric displacement ($n = 0$ mode). When the steady vortex ring is far from the sphere, it is unstable to a tilting ($n = 1$) perturbation, but stable to all higher modes.

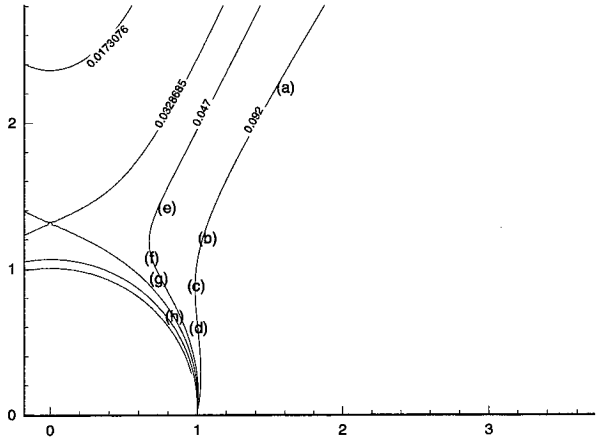

Figure 2.5: The locations of steady rings for which we compute growth rates, distances have been non-dimensionalized on the sphere radius.

In his study of wakeless axisymmetric bubbles, Mieron [12] found bubbles shapes to be stable to all perturbations with oscillation frequencies determined by the ratio of inertial forces to surface tension know as the Weber number. We conjecture that the natural frequencies of a bubble may be tuned by means of the Webber number to lead to a cooperative instability with a vortex ring wake for given modal perturbations.

For rings closer to the sphere, the eigenvalues of higher modes appear, in order, to pass through the origin and become unstable. For most core structures we are unable to draw any concrete conclusions from this behavior for a subtle reason: in calculating the image flow we assumed that the velocity at the surface of the sphere induced by the thin vortex ring may be adequately approximated by the velocity induced by a delta function of vorticity lying along the centerline of the ring. When the distance from the vortex to the sphere is of the same order as the vortex core radius c_r this approximation may no longer be valid. Of course the core size of a given steady solution depends on the internal structure of the vortex by means of equations (2.8) and (2.27). For a given steady location of the vortex ring near the sphere the ratio $\delta c_r/R$ is calculated, one could in principle choose a core structure (hence a δ) such that the core size is small enough to satisfy our approximations.

	(a)	(b)	(c)	(d)
$Z/a, R/a$	$2.473, 1.662$	$1.089, 1.356$	$0.997, 1.036$	$0.986, 0.694$
$\delta c_r/R$	0.08973	0.09192	0.091791	0.883900
$\Gamma/(Ua)$	-8.1306	-4.32309	-3.0436	-1.56399
$\pm\mu_o\frac{a}{U}$	$i0.0837$	$i0.30929$	$i0.55983$	$i1.19298$
$\pm\mu_1\frac{a}{U}$	0.3316	0.64272	0.858324	1.02720
$\pm\mu_2\frac{a}{U}$	$i0.4240$	$i0.59353$	0.026460	1.34451
$\pm\mu_3\frac{a}{U}$	$i1.0010$	$i1.67467$	$i1.85708$	$i1.31257$
$\pm\mu_4\frac{a}{U}$	$i1.4823$	$i2.51483$	$i2.94033$	$i2.95861$
$\pm\mu_5\frac{a}{U}$	$i1.8537$	$i3.13988$	$i3.73117$	$i4.10829$

Table 2.1: The first six growth rates μ_n corresponding to perturbations $\exp(in\theta)$ computed at four different steady solutions shown in Figure 3.5.

	(e)	(f)	(g)	(h)
$Z/a, R/a$	$0.780, 1.588$	$0.641, 1.222$	$0.689, 1.027$	$0.831, 0.785$
$\delta c_r/R$	0.04489	0.045215	0.04553	0.0477
$\Gamma/(Ua)$	-4.2867	-2.9752	-2.1707	-1.3297
$\pm\mu_o\frac{a}{U}$	$i0.17281$	$i3.17387$	$i0.57133$	$i1.0959$
$\pm\mu_1\frac{a}{U}$	0.51112	0.775162	0.97283	1.0139
$\pm\mu_2\frac{a}{U}$	$i0.80758$	0.217324	1.27313	1.93570
$\pm\mu_3\frac{a}{U}$	$i2.04214$	$i2.05502$	$i1.22269$	$i1.74478$
$\pm\mu_4\frac{a}{U}$	$i3.31178$	$i3.64643$	$i3.16675$	$i1.82264$
$\pm\mu_5\frac{a}{U}$	$i4.60039$	$i5.21764$	$i4.91942$	$i3.98436$

Table 2.2: The first six growth rates μ_n corresponding to perturbations $\exp(in\theta)$ computed at four different steady solutions shown in Figure 3.5.

2.4 Hamiltonian for axisymmetric problem

Pedrizetti and Novikov [28] present without derivation a particular Hamiltonian for a thin cored vortex ring interacting with a sphere, for which the velocity of the ring in absence of the sphere would be given by $U = \frac{\Gamma}{4\pi R}\left[\log(\frac{8R}{c_r}) + 3/2 - \log(8)\right]$. This speed is evidently particular to a certain class of core structures. In this section we construct a more general Hamiltonian corresponding to axisymmetric flow consisting of a vortex ring with swirl in the presence of a sphere moving at a constant speed. By examining the isolines of this Hamiltonian, we can make observations about axisymmetric interactions between a vortex ring and a sphere as well as the stability of a steady configurations to axisymmetric perturbations. Qualitatively, our investigation and results reflect that of two dimensional Föppl flow. We also present the Hamiltonian for the interaction of multiple vortex rings, each with their own core structure, in the presence of a body and background flow under the requirement of axisymmetry.

As in the chapter on Föppl flow, we examine the finite part of the kinetic energy ($K.E.$) in arriving at a Hamiltonian. We consider an axisymmetric flow consisting of a vortex ring with core radius c_r and centerline radius R interacting with a sphere embedded in otherwise potential flow. Let us start by computing the kinetic energy for axisymmetric flow with swirl about a body;

$$\begin{aligned} K.E. &= \frac{1}{2}\int_{fluid} \left(u^2+v^2+w^2\right)\rho\, d\rho d\phi dz \\ &= \pi \int \left(u^2+v^2+w^2\right)\rho\, d\rho dz, \end{aligned} \tag{2.43}$$

where we have exploited axisymmetry in performing one integration. We assume that the azimuthal velocity w is purely swirl so that u and v may be obtained from a Stokes stream function $\psi = \psi_o + \psi_v$. Here ψ_o represents the time-independent irrotational background flow and ψ_v produces the flow induced by the axisymmetric vortex ring. On the boundary of the body $\psi_o = \psi_v = 0$ and ψ_o tends to plain flow for large distances while ψ_v tends to a constant. Vorticity will point in the azimuthal

direction and may be obtained as

$$\omega = -\frac{1}{\rho}\frac{\partial^2 \psi_v}{\partial z^2} - \frac{1}{\rho}\frac{\partial^2 \psi_v}{\partial \rho^2} + \frac{1}{\rho}\frac{\partial \psi_v}{\partial \rho}. \tag{2.44}$$

To compute the finite part of the kinetic energy, which we will call T, we subtract the energy of the background flow ψ_o;

$$\begin{aligned} T &= \pi \int \left(u^2 + v^2 + w^2\right) \rho \; d\rho dz - \pi \int \frac{1}{\rho}\left(\frac{\partial \psi_o}{\partial \rho}\right)^2 + \frac{1}{\rho}\left(\frac{\partial \psi_o}{\partial z}\right)^2 d\rho dz \qquad (2.45) \\ &= \pi \int \frac{1}{\rho}\left(\left(\frac{\partial \psi_v}{\partial \rho}\right)^2 + 2\frac{\partial \psi_v}{\partial \rho}\frac{\partial \psi_o}{\partial \rho}\right) d\rho dz + \pi \int \frac{1}{\rho}\left(\left(\frac{\partial \psi_v}{\partial z}\right)^2 + 2\frac{\partial \psi_v}{\partial z}\frac{\partial \psi_o}{\partial z}\right) d\rho dz \\ &\quad + \pi \int w^2 \rho \; d\rho dz. \end{aligned}$$

After integration by parts and using the boundary conditions for ψ_o and ψ_v we find

$$T = \pi \int \left(2\psi_o + \psi_v\right) \omega \; d\rho dz + \pi \int w^2 \rho \; d\rho dz. \tag{2.46}$$

The integrations are over all fluid, but we expect the vorticity ω to only be non-zero in compact regions (the vortex filament). We reduce the generality of this expression for the finite part of the energy by requiring that the swirl velocity w and vorticity ω exist only with in the vortex ring. Furthermore, we split the streamfunction ψ_v into two parts;

$$\psi_v = \psi_{vortex} + \psi_{image} \tag{2.47}$$

where ψ_{vortex} represents the flow induced by a ring in unbounded fluid - away from the vortex core it has the approximate form given in expression (2.15). The remaining term ψ_{image} is the irrotational flow which allows ψ_v to meet the given boundary conditions on the sphere and at infinity; equation (2.19) gives ψ_{image}. The finite part of the kinetic energy may now be written as

$$T = \pi \int_{vortex} \left(2\psi_o + \psi_{image} + \psi_{vortex}\right) \omega \; d\rho dz + \pi \int_{vortex} w^2 \rho \; d\rho dz \tag{2.48}$$

where the integrations are over a cross-section of the ring.

We divide T into three parts which we compute separately;

$$T = T_{vortex} + T_o + T_{image}. \tag{2.49}$$

To leading order Saffman [32] has computed the kinetic energy due a single vortex ring T_{vortex} as

$$\begin{aligned} T_{vortex} &= \pi \int_{vortex} \left(\psi_{vortex}\omega + w^2\rho\right) d\rho dz \\ &\sim \frac{1}{2} R\Gamma^2 \left[\log\left(\frac{8R}{c_r}\right) - 2 + \frac{2\pi^2 c_r^2}{\Gamma^2}\overline{v^2} + \frac{2\pi^2 c_r^2}{\Gamma}\overline{w^2}\right], \end{aligned} \tag{2.50}$$

where the overbar denotes average across the ring cross-section. The kinetic energy T_o due to the interaction of the background flow with the vortex ring is computed as

$$\begin{aligned} T_o &= \pi \int_{vortex} 2\psi_o\omega \; d\rho dz \\ &\sim \pi\Gamma U \int \frac{\rho^2}{2}\left(1 - \frac{a^3}{\left(\rho^2 + z^2\right)^{3/2}}\right) \delta\left(z - Z\right) \delta\left(\rho - R\right) \; d\rho dz \\ &\sim \pi\Gamma U \frac{R^2}{2}\left(1 - \frac{a^3}{\left(R^2 + Z^2\right)^{3/2}}\right), \end{aligned} \tag{2.51}$$

where Z is the downstream distance of the ring. Similarly we compute T_{image}, the kinetic energy of the interaction between the image system and the vortex ring;

$$\begin{aligned} T_{image} &= \pi \int_{vortex} \psi_{image}\omega \; d\rho dz \\ &\sim -\Gamma^2 \frac{R^2 a}{4} \int_o^{2\pi} \frac{\cos\theta}{\sqrt{d^4 + 2a^2R^2\left(1 - \cos\theta\right)}} d\theta \end{aligned} \tag{2.52}$$

where $d^2 = R^2 + Z^2 - a^2$.

Imposing conservation of vortex core volume $\delta\left(Rc_r^2\right) = 0$ and vorticity $\delta\left(\Gamma\right) = 0$ Saffman [32] showed

$$\frac{\delta T_{vortex}}{\delta R} = 2\pi\Gamma R \; U_{self} \tag{2.53}$$

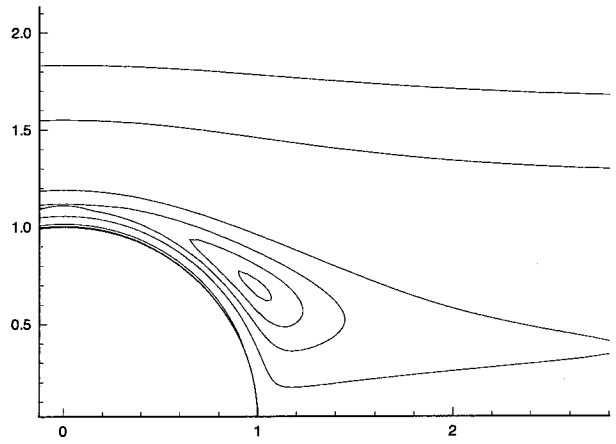

Figure 2.6: The contours of the Hamiltonian for a vortex ring and a sphere. Distances are non-dimensionalized on a. Here $\Gamma/(Ua) = -1.564$ and $\sigma = 0.0796$.

where U_{self} is the self induced velocity of a vortex ring, (2.7) and (2.8). It is now a simple matter to show that T will be conserved; using (2.53) and direct differentiation we can show

$$\frac{\delta T}{\delta R} = 2\pi\Gamma R\left(\frac{dZ}{dt}\right) \tag{2.54}$$

$$\frac{\delta T}{\delta Z} = -2\pi\Gamma R\left(\frac{dR}{dt}\right) \tag{2.55}$$

which takes Hamiltonian form if we make the identifications $p = \pi\Gamma R^2$ and $q = Z$.

For a uniform thin cored ring without swirl, the conserved quantity is given by

$$\begin{aligned} T = {} & 2\pi\Gamma U\frac{R^2}{2}\left(1 - \frac{a^3}{\left(R^2+Z^2\right)^{3/2}}\right) + \frac{1}{2}R\Gamma^2\left[\log\left(\frac{8R^{3/2}}{\sigma}\right) - 2 + \frac{1}{4}\right] \\ & -\Gamma^2\frac{R^2 a}{4}\int_o^{2\pi}\frac{\cos\theta}{\sqrt{d^4 + 2a^2R^2\left(1-\cos\theta\right)}}d\theta \end{aligned} \tag{2.56}$$

where $\sigma = c_r\left(0\right)\sqrt{R(0)}$, and results from conservation of volume.

We see in Figure 2.6 a similarity to the plot of the Kirchhoff-Routh function for the point vortex pair behind the cylinder.

We can, in analogy to the Kirchhoff-Routh function, give the Hamiltonian for

an axisymmetric constellation of N thin cored vortex rings each with their own internal structure interacting in the presence of a body and with a background flow. The locations of the vortex rings are given by (Z_j, R_j) and they have corresponding strengths Γ_j. Given the irrotational background flow $\psi_o(z,\rho)$, which is zero on the body boundary; we define

$$G(z,\rho|Z_j,R_j) = \frac{\rho R_j}{4\pi}\int_o^{2\pi} \frac{\cos\theta}{\sqrt{(z-Z_j)^2+\rho^2+R_j^2-2\rho R_j\cos\theta}}d\theta + g(z,\rho|Z_j,R_j) \tag{2.57}$$

by requiring $G(z,\rho|Z_j,R_j) = 0$ on the body boundary, $\nabla^2 g = 0$ in the fluid, and g tends to a constant at infinity. Following similar steps to those above, we find that the finite part of the kinetic energy is conserved and takes the form

$$\begin{aligned} H &= \sum_{k\neq j}\sum_{j}\Gamma_j\Gamma_k G(Z_j,R_j|Z_k,R_k) + \sum_j \Gamma_j^2 g(Z_j,R_j|Z_j,R_j) \\ &+ \sum_j \Gamma_j^2 T_j^s(Z_j,R_j) + 2\sum_j \Gamma_j\psi_o(Z_j,R_j) \end{aligned} \tag{2.58}$$

where T_j^s is related to the self induced energy of the j^{th} vortex ring

$$T_j^s = \frac{1}{2}R_j\left[\log\left(\frac{8R_j}{c_{r_j}}\right) - 2 + \frac{2\pi^2 c_{r_j}^2}{\Gamma_j^2}\overline{v_j^2} + \frac{2\pi^2 c_{r_j}^2}{\Gamma_j}\overline{w_j^2}\right]. \tag{2.59}$$

The individual rings evolve according to

$$\frac{\partial H}{\partial R_j} = 2\pi\Gamma_j R_j\left(\frac{dZ_j}{dt}\right) \tag{2.60}$$

$$\frac{\partial H}{\partial Z_j} = -2\pi\Gamma_j R_j\left(\frac{dR_j}{dt}\right). \tag{2.61}$$

In form, equation (2.58) differs from the Kirchhoff-Routh function only by the inclusion of the self induced energy terms. The finite core radius of the vortex rings leads to a finite self induced energy. In calculating the finite part of the kinetic energy for two dimensional flow in the last chapter, we removed the divergent self induced kinetic energy for point vortices.

Chapter 3 A two-dimensional bubble with point-vortex wake

3.1 Introduction

There has long been much interest in the problem of rising bubbles. In 1956 Saffman [31] presented a theory of zig-zagging bubbles which assumed irrotational flow near the front of the bubble, while Moore [18],[19] showed that when the Reynolds number is sufficiently high, the viscous effects are confined to a narrow boundary layer on the surface of a bubble. In his investigation of the shape and stability of an inviscid bubble rising at a constant speed in potential flow, Meiron [12] neglected both gravity and viscosity assuming that while the terminal velocity may be determined by the balance between small viscous and gravitational effects, the inviscid pressure forces and surface tension determine the shape and stability of the bubble. A parameter of interest in such a case is the ratio of inertial forces to surface tension, referred to as a Weber number. In his study Meiron examined the linear stability of three-dimensional perturbations to axisymmetric bubbles in potential flow; he found stability for all computed steady solutions. Ryskin and Leal [29],[30] first computed axisymmetric rising bubbles for a variety of Reynolds numbers, many with bound vorticity in the wake. The linear stability of such solutions remains an open question largely due to the computational intensity of the problem.

The case of two-dimensional bubbles rising in irrotational inviscid fluid has received its share of attention. McLeod [11] presented an exact analytic solution for a particular Weber number. Shankar [33] numerically computed the shape of steady-state bubbles with aspect ratio from 1 to ∞, identifying a maximum value of the Weber number (≈ 0.745) above which no steady symmetric two-dimensional solutions were found to exist. Nie and Tanveer [27] examined the stability of these bubbles

and found, as Meiron has for the three-dimensional analog, the bubbles to be linearly stable for all Weber numbers. From numerical integration of the nonlinear equations, Nie and Tanveer found that an initial condition that consists of a steady high aspect ratio bubble and a suitable symmetric eigenmode may result in pinching of the bubble neck as it tends to oscillate about the steady state. They present a estimate of the finite perturbation amplitude necessary for such an occurrence.

In this chapter we generalize the Föppl flow to a two-dimensional bubble with a simple recirculating wake formed by a vortex pair. In this way we extend the current work on two dimensional bubbles. We numerically solve the steady system and present solutions for a variety of vortex strengths and Weber number. We find the addition of the point vortex wake increases the maximum Weber number and affects the bubble shape by breaking the fore-aft symmetry. A numerical computation of linear stability shows such flows are unstable; both pure growth and oscillatory growth are found.

3.2 The physical considerations

In this section we derive equations which govern the evolution of a system consisting of a two dimensional incompressible bubble traveling at a constant rate in inviscid fluid and a counter-rotating vortex pair. As a simplification, the internal structure of the bubble is not specified; instead we assume a constant pressure P_o at the boundary of the bubble. This pressure will become a part of a Bernoulli constant and will not be an independent parameter. Physically one could interpret our results in terms of a drop rather than a bubble when P_o is not zero.

Differential equations relating the location of the vortices to the fluid flow will result from desingularizing the velocity field by removing the self induced infinite rotational velocity at each vortex. The bubble's shape will be determined by requiring that the interface be a material line, and from an application of a Bernoulli equation.

3.2.1 Nondimensionalization and the Weber number

We assume that our two-dimensional bubble is rising through a fluid of density ρ at a constant speed U_∞, which results from a balance of viscous drag and buoyancy. The bubble has area A and surface tension S at the interface.

Following Nie and Tanveer [27], we non-dimensionalize with respect to L, V^*, and ρ where

$$L = \sqrt{\frac{A}{\pi}} \tag{3.1}$$

$$V^* = \sqrt{\frac{S}{\rho L}}. \tag{3.2}$$

From these characteristic scales, we can construct the non-dimensional quantity referred to as the Weber number:

$$W_e = U_\infty \sqrt{\frac{\rho L}{S}}. \tag{3.3}$$

3.2.2 The vortex wake model

Selecting the centroid of the bubble as the origin and orienting the right handed coordinate axes in such a way that the x-axis points in the downstream direction, we adopt standard complex notation for two-dimensional flow, $z = x + iy$. Modeling the wake behind a bubble, we place a point vortex of strength Γ at z_+ and another of strength $-\Gamma$ at z_-. Define the non-dimensional strength γ as

$$\gamma = \Gamma/(V^* L). \tag{3.4}$$

We utilize the complex velocity potential formulation as in previous chapters. The complex potential, W, is related to the streamfunction, ψ, and velocity potential ϕ by

$$W(z) = \phi(z) + i\psi(z). \tag{3.5}$$

The fluid velocities may be obtained from W by

$$u - iv = \frac{\partial W}{\partial z}. \tag{3.6}$$

Recall that in unbounded flow a single point vortex at z_o with circulation γ corresponds to a complex potential $-i\gamma/(2\pi)\log(z - z_o)$. In general, the velocity field is singular at a point vortex. To relate the velocities of the point vortices at $z_\pm$ to our flow, we subtract the singular rotational velocities of the point vortices when evaluating the velocity field;

$$\overline{\left(\frac{\partial z_+}{\partial t}\right)} = \lim_{z \to z_+} \frac{\partial}{\partial z}\left(W + i\frac{\gamma}{2\pi}\log(z - z_+)\right) \tag{3.7}$$

$$\overline{\left(\frac{\partial z_-}{\partial t}\right)} = \lim_{z \to z_-} \frac{\partial}{\partial z}\left(W - i\frac{\gamma}{2\pi}\log(z - z_-)\right) \tag{3.8}$$

where the overbar denotes the complex conjugate. We refer to this desingularization as applying the non-self induction condition.

3.2.3 Boundary conditions at the bubble-fluid interface

The existence of viscosity is only implied in the idea of a terminal velocity for our bubble so we use the Euler equations. We limit ourselves to almost irrotational flow, allowing only the wake point vortices. Neglecting the body force gravity, the Euler equation reads

$$\frac{\partial \mathbf{u}}{\partial t} + \nabla\left(\frac{1}{2}|\mathbf{u}|^2 + \frac{P}{\rho}\right) = \mathbf{u} \times \boldsymbol{\omega}. \tag{3.9}$$

Away from the point vortices, we represent the flow as the gradient of a potential ϕ so the Euler equation implies

$$\nabla\left(\frac{\partial \phi}{\partial t} + \frac{1}{2}|\mathbf{u}|^2 + \frac{P}{\rho}\right) = 0. \tag{3.10}$$

Integrating gives

$$\frac{\partial \phi}{\partial t} + \frac{1}{2}|\mathbf{u}|^2 + \frac{P}{\rho} = C_1(t) \tag{3.11}$$

on the interface. We require that $\frac{\partial \phi}{\partial t}$ tends to zero at infinity.

We assume that the pressure inside the bubble at the interface is a constant, P_o. We make no further assumptions about the interior of the bubble. Continuity of force across the interface requires a jump in the pressure balanced by the product of the curvature κ and the surface tension S;

$$P - P_o = \kappa S. \tag{3.12}$$

Eliminating the pressure from Bernoulli's equation (3.11) gives

$$\phi_t + \frac{1}{2}|\mathbf{u}|^2 + \kappa S/\rho = (C_1(t) - P_o/\rho) \tag{3.13}$$

on the bubble interface.

There also is the kinematic condition which requires the interface to moves with the fluid;

$$\frac{\partial \phi}{\partial \eta} = V_n \tag{3.14}$$

where η is the outward normal and V_η is the velocity of the boundary in the direction of η. Together equations (3.13) and (3.14) relate the evolution of the bubble to the fluid.

3.3 The equations expressed in terms of a conformal map

To easily meet the boundary conditions, we view the physical z-plane as the image of a non-physical ζ-plane in which the boundary of the bubble is circular. The map, $Z(\zeta)$, which takes the unit circle to the boundary of the bubble will be an unknown for

which we solve. In the following subsection we examine the connection between the non-self-induction condition and the conformal map by addressing the relationship between the velocity of a vortex in the physical and non-physical planes. Then we re-write the interface conditions in terms of the conformal map.

3.3.1 The velocity of a vortex in the physical plane

Given a complex velocity potential W defined in the non-physical ζ-plane and a conformal map $z = Z(\zeta)$ to the physical z-plane, the map can be used to eliminate ζ in W and thus give a complex velocity potential in the z-plane. Away from any point vortices, the expression

$$U(z) - iV(z) = \frac{dW}{dz} \tag{3.15}$$

can be used to find the velocity of the flow. In general it is easier to forgo the elimination of ζ and simply compute

$$U - iV = \frac{dW}{d\zeta} / \frac{dZ}{d\zeta}. \tag{3.16}$$

So the velocity at a point in the physical plane is just the velocity of its pre-image multiplied by the factor $\left(\frac{dZ}{d\zeta}\right)^{-1}$. This relationship does not hold at point vortices.

Suppose in the ζ-plane we locally have a single point vortex and potential flow

$$W(\zeta) = -i\frac{\gamma}{2\pi}\log(\zeta - \zeta_+) + g(\zeta). \tag{3.17}$$

Were we to apply the non-self induction condition in the nonphysical ζ-plane, we would find the velocity of point vortex as simply

$$u_v - iv_v = \frac{dg}{d\zeta}\left(\zeta_+\right). \tag{3.18}$$

which might lead us to the *false* conclusion

$$\overline{\left(\frac{\partial z_+}{\partial t}\right)} = \left(u_v - iv_v\right) / \frac{dZ\left(\zeta_+\right)}{d\zeta_+} \tag{3.19}$$

where $z_+ = Z\left(\zeta_+\right)$.

To obtain the correct velocity of the point vortex we apply the non-self induction condition in the physical z-plane;

$$\overline{\left(\frac{\partial z_+}{\partial t}\right)} = \lim_{z \to z_+} \frac{\partial}{\partial z}\left(W + i\frac{\gamma}{2\pi}\log\left(z - z_+\right)\right). \tag{3.20}$$

In terms of ζ the velocity of the point vortex located at $z_+ = Z\left(\zeta_+\right)$ may be computed as

$$\overline{\left(\frac{\partial z_+}{\partial t}\right)} = \lim_{\zeta \to \zeta_+} \frac{\partial}{\partial \zeta}\left(W + i\frac{\gamma}{2\pi}\log\left(Z\left(\zeta\right) - Z\left(\zeta_+\right)\right)\right) / \frac{dZ}{d\zeta} \tag{3.21}$$

$$= \left(\frac{dg}{d\zeta} / \frac{dZ}{d\zeta} + \frac{i\gamma}{4\pi}\frac{d^2Z}{d\zeta^2} / \left(\frac{dZ}{d\zeta}\right)^2\right)|_{\zeta=\zeta_+}. \tag{3.22}$$

3.3.2 The interface conditions expressed in terms of the conformal map

In the previous section we related the velocity of a vortex point to the conformal map. In this section we give a form for the map which takes the unit circle in the ζ-plane to the boundary of our bubble in the z-plane. We give an expansion form for the complex potential in terms of ζ and rewrite Bernoulli's equation (3.13) and the kinematic boundary condition (3.14) in terms of the map and the potential. The equations we formulate reduce to those of Nie and Tanveer [27] when the point vortices are neglected.

We assume that a point in the fluid is the image of a point in the unit disk and the boundary of the bubble is the image of the unit circle itself under the conformal map $Z\left(\zeta, t\right)$.

We may simply express the unit normal n and the curvature κ in terms of the map. When evaluated on the bubble interface

$$n = \zeta\frac{\partial Z}{\partial \zeta} / \left|\frac{\partial Z}{\partial \zeta}\right|^2 \tag{3.23}$$

gives the unit normal to the boundary. Since the boundary of the bubble may be parameterized as given by $Z(\exp(i\theta),t) = X(\theta,t) + iY(\theta,t)$; the curvature, given by $\kappa = \left(Y''X' - X''Y'\right) / \left(X'^2 + Y'^2\right)^{3/2}$, takes the form

$$\kappa = \frac{1}{|Z_\zeta|}\left(1 + \Re\left(\zeta\frac{Z_{\zeta\zeta}}{Z_\zeta}\right)\right). \tag{3.24}$$

We assume the map has an expansion of the form

$$Z(\zeta,t) = \frac{a_{-1}(t)}{\zeta} + \sum_{j=0}^{\infty} a_j(t)\zeta^j. \tag{3.25}$$

Under this assumption, the non-dimensionalized area condition $A = \pi$ gives the simple relation

$$A = \pi a_{-1}^2\left(1 - \sum_{j=1}^{\infty} j\,|a_j|^2\right) = \pi. \tag{3.26}$$

We require that our bubble is rising at a constant rate, ostensibly determined by viscous drag and gravity balancing the buoyancy of the bubble. The flow at infinity tends to parallel flow of speed U_∞ in the positive x direction. Notice from definitions (3.2) and (3.3) that the ratio U_∞/V^* gives the Weber number W_e.

Assuming our bubble has no circulation, the velocity potential defined in the ζ-plane is given in general by

$$W(\zeta,t) = W_e\frac{a_{-1}}{\zeta} + \sum_{j=0}^{\infty} b_j(t)\zeta^j - i\frac{\gamma}{2\pi}\log\left(\frac{\zeta-\zeta_+(t)}{\zeta-\zeta_-(t)}\right) + i\frac{\gamma}{2\pi}\log\left(\frac{\frac{1}{\zeta}-\overline{\zeta}_+(t)}{\frac{1}{\zeta}-\overline{\zeta}_-(t)}\right) \tag{3.27}$$

where $\zeta_\pm(t)$ is in the unit disk and $Z(\zeta_\pm(t),t) = z_\pm$ gives the location of a point vortex with strength $\pm\gamma$.

Rewriting Bernoulli's equation (3.13) using the conformal map Z the complex velocity potential W and the curvature gives the nonlinear dynamic boundary condition

$$\Re\left(W_t - \frac{\partial W}{\partial \zeta}/\frac{\partial Z}{\partial \zeta} Z_t\right) = -\frac{1}{2}\left|\frac{\partial W}{\partial \zeta}/\frac{\partial Z}{\partial \zeta}\right|^2 - \frac{1}{|Z_\zeta|}\left(1 + \Re\left(\zeta \frac{Z_{\zeta\zeta}}{Z_\zeta}\right)\right) + C. \tag{3.28}$$

Since the dot product in complex notation has the form $a \cdot b = \Re(a\overline{b})$, we see that the normal fluid velocity at the interface becomes

$$\nabla\phi \cdot n = \Re\left(\zeta \frac{\partial W}{\partial \zeta}/\left|\frac{\partial Z}{\partial \zeta}\right|^2\right) \tag{3.29}$$

in terms of the map and we also find that the velocity of the boundary in the normal direction is

$$V_n = \Re\left(\frac{Z_t}{\zeta \frac{\partial Z}{\partial \zeta}}\right) \tag{3.30}$$

where we have used $\overline{\zeta} = 1/\zeta$ on the boundary. The kinematic boundary condition (3.14) as described by the map becomes

$$\Re\left(\zeta \frac{\partial W}{\partial \zeta}/\left|\frac{\partial Z}{\partial \zeta}\right|^2\right) = \Re\left(\frac{Z_t}{\zeta \frac{\partial Z}{\partial \zeta}}\right). \tag{3.31}$$

3.4 The steady problem

The evolution of a bubble interacting with point vortices located at $Z\left(\zeta_\pm(t), t\right)$ is given by map functions $a_j(t)$, complex potential functions $b_j(t)$, as well as the pre-images $\zeta_+(t)$ and $\zeta_-(t)$ which satisfy the boundary conditions, (3.28) and (3.31), and the velocity equations, (3.7) and (3.8). We look for steady solutions with symmetry about the x-axis which points in the downstream direction. Recall that the quantities P_o, L, and S are related to the bubble as the physical properties of the pressure within the bubble, the length based on the bubble area, and the surface tension while the fluid is described by its density ρ and upstream pressure P_∞ and velocity U_∞. These

all combine to form a single nondimensional number Ω we refer to as the Bernoulli constant. Following the streamline from infinity to the stagnation point at the front of the bubble fixes the constant in the Bernoulli equation (3.13); nondimensionalizing we find

$$\phi_t + \frac{1}{2}|\mathbf{u}|^2 + \kappa = \Omega \tag{3.32}$$

where $\Omega = \left(\frac{1}{2}\rho U_\infty^2 + P_\infty - P_o\right) L/S$. Other parameters for our problem are the Weber number $W_e = U_\infty \sqrt{\rho L/S}$ and the nondimensional strengths of the vortices $\gamma = \Gamma/\sqrt{SL/\rho}$.

3.4.1 Reduction of our equations for the steady problem

We may simplify our equations when searching for solutions to the symmetric steady problem. The symmetry of the bubble about the x-axis implies $\Im(a_j(t)) = 0$; we define $d_j = \Re(a_j)$ so that the map for the steady symmetric bubble may be written as

$$Z(\zeta, t) = Z_s(\zeta) = d_{-1}\left(\frac{1}{\zeta} + \sum_{j=0}^{\infty} d_j \zeta^j\right). \tag{3.33}$$

We also assume the point vortices behind the rising bubble are symmetrically situated about the x-axis, $z_+ = \overline{z}_-$. Real d_j then implies, that the pre-image of the vortices are also conjugates,

$$\zeta_+ = \overline{\zeta}_-. \tag{3.34}$$

The condition that the bubble boundary has the same normal velocity as the fluid simplifies the form of the complex potential (3.27); from an examination of the kinematic condition (3.31) we see that the complex potential for the steady problem has the general form

$$W(\zeta,t) = W_s(\zeta) = W_e\, d_{-1}\left(\frac{1}{\zeta}+\zeta\right) - i\frac{\gamma}{2\pi}\log\left(\frac{\zeta-\zeta_+}{\zeta-\overline{\zeta}_+}\right) + i\frac{\gamma}{2\pi}\log\left(\frac{\frac{1}{\zeta}-\overline{\zeta}_+}{\frac{1}{\zeta}-\zeta_+}\right). \tag{3.35}$$

The Bernoulli equation (3.13) evaluated on the boundary, $|\zeta| = 1$, reduces to

$$\Omega - \frac{1}{2}\left|\frac{\partial W_s}{\partial\zeta}/\frac{\partial Z_s}{\partial\zeta}\right|^2 - \left|\frac{\partial Z_s}{\partial\zeta}\right|^{-1}\left(1+\Re\left(\zeta\frac{\partial^2 Z_s}{\partial\zeta^2}/\frac{\partial Z_s}{\partial\zeta}\right)\right) = 0. \tag{3.36}$$

The equations for the steady symmetric vortex pair are complex conjugates and thus only one need be examined;

$$\lim_{\zeta\to\zeta_+}\frac{d}{d\zeta}\left(W(\zeta) + i\frac{\gamma}{2\pi}\log(Z(\zeta)-Z(\zeta_+))\right) = 0, \tag{3.37}$$

or explicitly

$$\begin{aligned} 0 \;=\; & W_e\, d_{-1}\left(1-\frac{1}{\zeta_+^2}\right) - i\frac{\gamma}{2\pi}\left(\frac{-1}{\zeta_+-\overline{\zeta}_+} + \frac{1}{\zeta_+}\frac{1}{1-|\zeta_+|^2} - \frac{1}{\zeta_+}\frac{1}{1-\zeta_+^2}\right) \\ & + \frac{i\gamma}{4\pi}\frac{d^2Z}{d\zeta^2}/\left(\frac{dZ}{d\zeta}\right). \end{aligned} \tag{3.38}$$

The area constraint takes the form

$$d_{-1}^2\left(1-\sum_{j=1}^{\infty} j d_j^2\right) = 1. \tag{3.39}$$

Solving the steady problem requires finding the vortex location $Z_s\left(\zeta_+\right)$ and real map constants d_j such that equations (3.36), (3.38) and (3.39) are satisfied.

3.4.2 The numerical problem

We truncate the map (3.33) which defines the bubble shape so that $d_j = 0$ for all $j > N-2$. To create the numerical problem, we evaluate the Bernoulli equation (3.36) at the discrete points $\zeta_k = \exp\left(ik\pi/(N-1)\right)$ for $k \in [0, N-1]$, giving N boundary equations. The steady vortex equation (3.38) and the area equation (3.39)

bring the number of equations up to $N+2$.

We treat Ω and γ as given and solve, using Newton's Method, for the unknowns W_e, d_j, and ζ_+. To do such, it was found to be most convenient to specify Ωd_{-1} and $\gamma/(d_{-1}W_e)$ and solve for $W_e^2 d_{-1}$, ζ_+, and d_j $(N > j > -1)$ using the boundary equations and the vortex equation, then use the area equation to determine d_{-1} and thus W_e.

At first glance the counting seems fine, $N+2$ equations and $N+2$ unknowns, but on further examination it becomes apparent that our equations are translationally invariant; specifically they are independent of d_0. Rather than impose a centroid condition, the pseudo inverse from Singular Value Decomposition was used when inverting the Jacobian in Newton's Method. After a steady shape was converged upon, d_0 was adjusted to place the centroid of the bubble at the origin. An analytic Jacobian allowed for quick computations.

3.4.3 Steady results

In computing the steady results we had no problem in obtaining L_1 errors less than 10^{-15} with a double precision code. The numerical accuracy of converged results was tested by reproducing the calculations with double the number of unknowns. Calculations at $N = 64$ confirmed the results found with only $N = 32$ shape expansion coefficients.

Notice that the ratio of vortex strength to the Weber number gives the vorticity non-dimensionalized on the flow at infinity and the characteristic radius of the bubble:

$$\frac{\gamma}{W_e} = \frac{\Gamma}{U_\infty L}. \tag{3.40}$$

We performed a continuation in the Bernoulli constant, Ω, for several different fixed values of γ/W_e. At each value of Ω we computed both W_e and the generalized aspect ratio, λ defined as

$$\lambda = \frac{Z_s(i) - Z_s(-i)}{Z_s(1) - Z_s(-1)}. \tag{3.41}$$

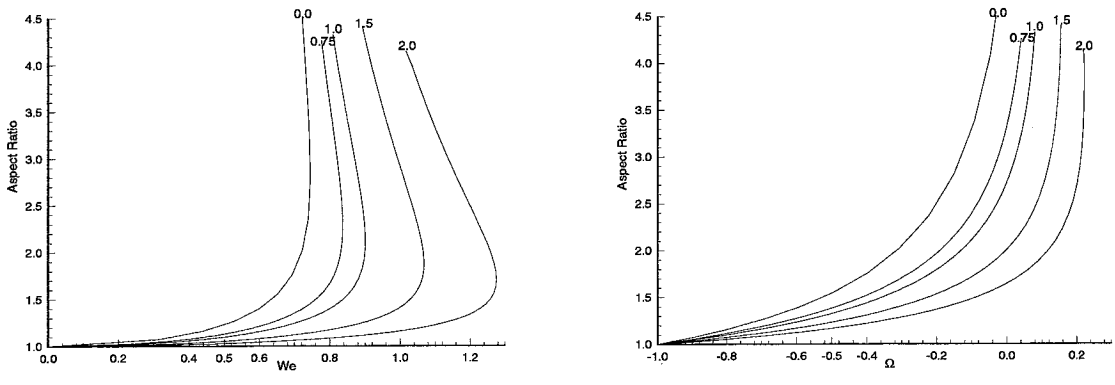

(a) (b)

Figure 3.1: Aspect ratio of the steady-state solution as a function of (a)W_e and (b) Ω. The curves are labeled by the fixed values of γ/W_e.

The folds in Figure 3.1 (a) indicate that more than one bubble may exist for a given vortex strength and Weber number, but in Figure 3.1 (b) we see that the Bernoulli constant together with the vortex strength will uniquely specify a bubble.

In the absence of vorticity it has been shown, Shankar [33], that symmetric steady bubbles exist for Weber numbers below a maximum (≈ 0.745). From an examination of Figure 3.1 (a) we see that the inclusion of the vortex pair wake increases the maximum Weber number.

As Figure 3.1 (b) shows, increasing the Bernoulli constant, while holding the vorticity constant, increases the aspect ratio, λ, of the bubble. Further plots (Figures 3.2, 3.3 and 3.4) of the streamlines show that as the aspect ratio increases the ends of bubble tilt forward giving the bubble a concave feature. We interpret this tilt as the result of the pressure maximums at the stagnation points. Similar bubble shapes have been computed for three dimensional axisymmetric bubbles in moderate Reynolds number flows, Ryskin and Leal [29],[30].

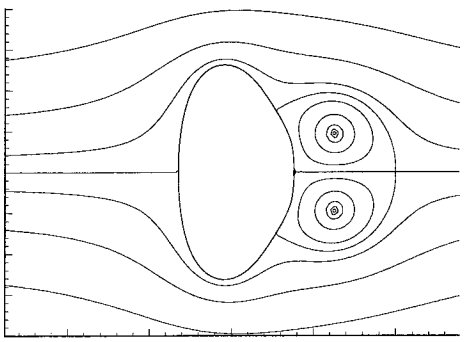

(a) $W_e = 0.823$, $\Omega = -0.233$

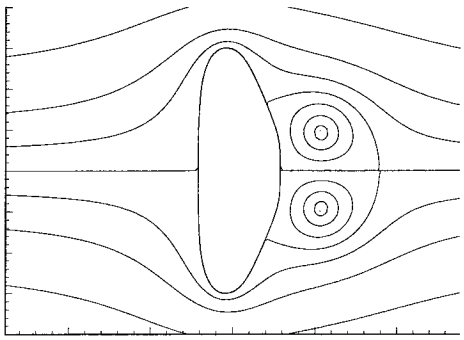

(b) $W_e = 0.820$, $\Omega = -0.023$

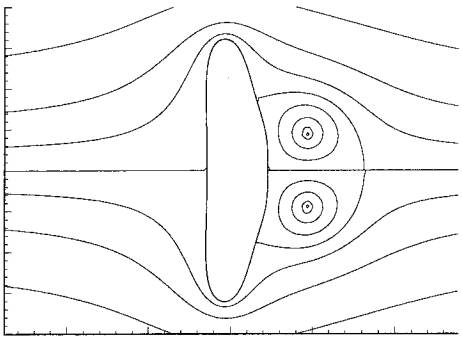

(c) $W_e = 0.772$, $\Omega = 0.043$

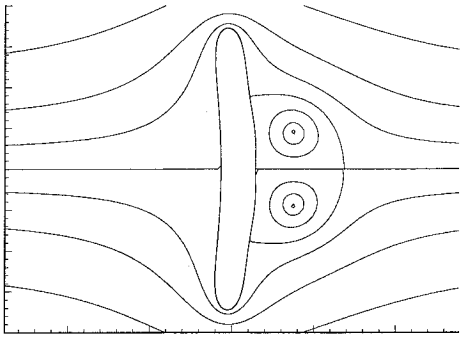

(d) $W_e = 0.681$, $\Omega = 0.078$

Figure 3.2: Streamlines for a range of Ω with $\gamma/W_e = 0.75$

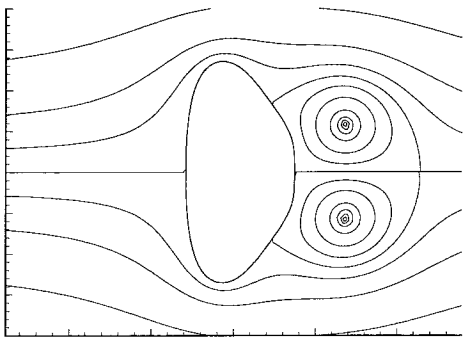

(a) $W_e = 0.9001$, $\Omega = -0.1172$

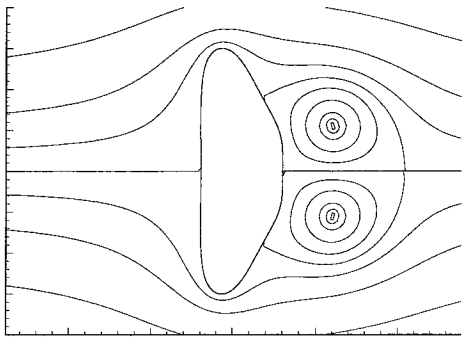

(b) $W_e = 0.8700$, $\Omega = 0.0256$

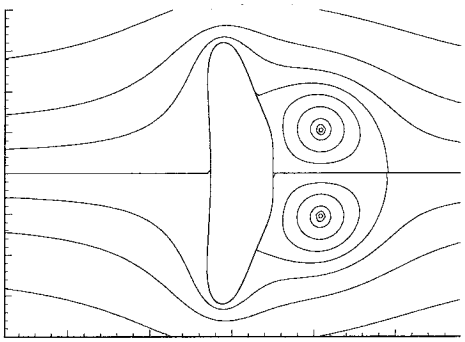

(c) $W_e = 0.8146$, $\Omega = 0.0763$

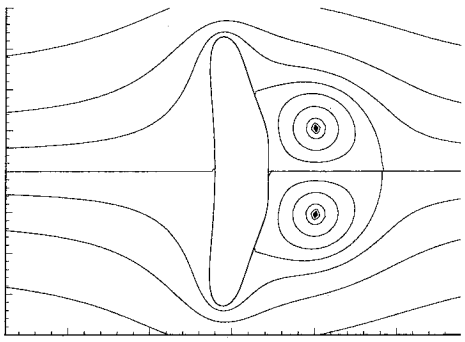

(d) $W_e = 0.7784$, $\Omega = 0.0901$

Figure 3.3: Streamlines for a range of Ω with $\gamma/W_e = 1.0$

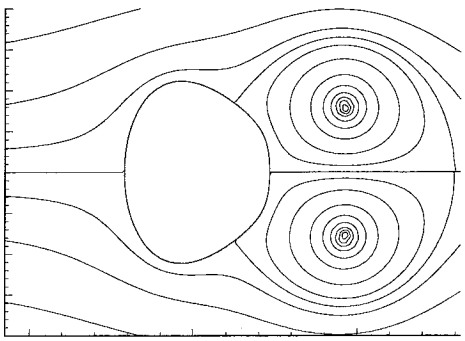

(a) $W_e = 0.8960$, $\Omega = -0.4743$

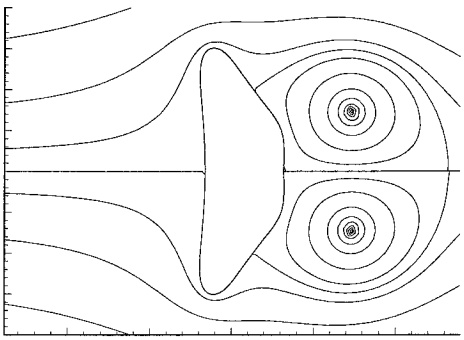

(b) $W_e = 0.9851$, $\Omega = 0.1283$

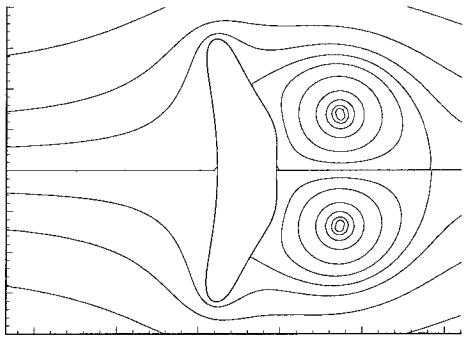

(c) $W_e = 0.8921$, $\Omega = 0.1540$

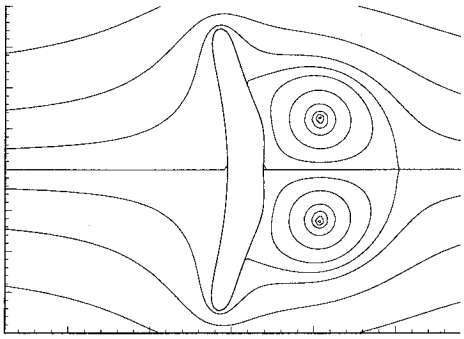

(d) $W_e = 0.7509$, $\Omega = 0.1409$

Figure 3.4: Streamlines for a range of Ω with $\gamma/W_e = 1.5$

3.5 Infinitesimal perturbations

In studying the stability of our two-dimensional bubbles, we infinitesimally perturb the shape of the bubble and locations of the point vortex pair while leaving the strength of the vortices and area of the bubble unchanged. By linearizing the governing equations about a given steady solution, we arrive at equations for the development of the perturbations. Those perturbations which do not grow with time are said to be stable, the others are unstable.

3.5.1 Linearization of the governing equations

To linearize the time-dependent equations we decompose the map and velocity potential in terms of a known steady solution and infinitesimal perturbation,

$$Z(\zeta,t) = Z_s(\zeta) + \epsilon\widehat{Z}(\zeta,t), \tag{3.42}$$

$$W(\zeta,t) = W_s(\zeta) + \epsilon\widehat{W}(\zeta,t), \tag{3.43}$$

We do likewise with the locations of the point vortexes in the ζ-plane,

$$\zeta_+(t) = \zeta_+ + \epsilon\widehat{\zeta}_+(t), \tag{3.44}$$

$$\zeta_+(t) = \bar{\zeta}_+ + \epsilon\widehat{\zeta}_+(t). \tag{3.45}$$

Substituting into the time dependent boundary equations, (3.28) and (3.31), and retaining only $O(\epsilon)$ terms yields the linearized equations. Requiring that $|\zeta| = 1$ on the bubble boundary leads to the following linearized equations:

$$\Re\left(\frac{\widehat{Z}_t}{\zeta\frac{dZ_s}{d\zeta}}\right) = \Re\left(\zeta\frac{\partial\widehat{W}}{\partial\zeta}\right) / \left|\frac{dZ_s}{d\zeta}\right|^2 \tag{3.46}$$

and

$$\Re\left(\widehat{W}_t - \widehat{Z}_t \frac{dW_s}{d\zeta}/\frac{dZ_s}{d\zeta}\right) = -\left|\frac{dW_s}{d\zeta}/\frac{dZ_s}{d\zeta}\right|^2 \Re\left(\frac{\partial \widehat{W}}{\partial \zeta}/\frac{dW_s}{d\zeta} - \frac{\partial \widehat{Z}}{\partial \zeta}/\frac{dZ_s}{d\zeta}\right) \tag{3.47}$$
$$+\left(1+\Re\left(\zeta\frac{d^2Z_s}{d\zeta^2}/\frac{dZ_s}{d\zeta}\right)\right)\Re\left(\frac{\partial \widehat{Z}}{\partial \zeta}/\frac{dZ_s}{d\zeta}\right)/\left|\frac{dZ_s}{d\zeta}\right|$$
$$-\Re\left(\zeta\frac{\partial^2 \widehat{Z}}{\partial \zeta^2}/\frac{dZ_s}{d\zeta} - \zeta\frac{d^2Z_s}{d\zeta^2}/\left(\frac{dZ_s}{d\zeta}\right)^2\frac{\partial \widehat{Z}}{\partial \zeta}\right).$$

From the original series expansion of the conformal map and the complex velocity potential we deduce that

$$\widehat{Z}(\zeta,t) = \frac{\widehat{a}(t)_{-1}}{\zeta} + \sum_{j=0}^{\infty}\widehat{a}(t)_j\zeta^j \tag{3.48}$$

and

$$\widehat{W}(\zeta,t) = W_e\frac{\widehat{a}(t)_{-1}}{\zeta} + \sum_{j=0}^{\infty}\widehat{b}_j(t)\zeta^j \tag{3.49}$$
$$-i\frac{\gamma}{2\pi}\left(\frac{1}{\zeta_+-\zeta}\widehat{\zeta}_+ + \frac{\zeta}{1-\zeta\zeta_-}\widehat{\overline{\zeta}}_- + \frac{1}{\zeta-\zeta_-}\widehat{\zeta}_- - \frac{\zeta}{1-\zeta\zeta_+}\widehat{\overline{\zeta}}_-\right)$$

where $\widehat{a}(t)_{-1}$ is real to preserve the original flow velocity at infinity. As a result of this conservation of flux at infinity, we expect the perturbations to conserve the bubble's area.

For the vortex which is the image of the point $\zeta_+(t) = \zeta_+ + \epsilon\widehat{\zeta}_+$, the linearized equation for this quantity's evolution is given by

$$\frac{d\widehat{\zeta}_+}{dt}\frac{dZ_s}{d\zeta}\,|_{\zeta=\zeta_+} + \frac{\partial \widehat{Z}}{\partial t}\,|_{\zeta=\zeta_+} = \overline{\left(\widehat{\Gamma}_1/\frac{dZ_s}{d\zeta}\right)}\,|_{\zeta=\zeta_+} \tag{3.50}$$

with

$$\widehat{\Gamma}_1 = \sum_{j=1}^{N-1}\widehat{b}_j(t)\zeta^{j-1}j - W_e\frac{\widehat{a}(t)_{-1}}{\zeta^2} + W_e d_{-1}\left(\frac{2}{\zeta_+^3}\right)\widehat{\zeta}_+ + \tag{3.51}$$
$$-i\frac{\gamma}{2\pi}\left(C_a\widehat{\zeta}_+ + C_b\widehat{\overline{\zeta}}_+ + C_c\widehat{\zeta}_- + C_d\widehat{\overline{\zeta}}_-\right) +$$

$$i\frac{\gamma}{4\pi}\left(C_e\widehat{\zeta}_- + C_f\frac{\partial^2\widehat{Z}}{\partial\zeta^2} + C_g\frac{\partial\widehat{Z}}{\partial\zeta}\right)$$

and where

$$\begin{aligned}
C_a &= \frac{1}{\left(\zeta_+ - \zeta_-\right)^2} + \frac{\zeta_+ - \zeta_-}{\left(\zeta_+^2 - 1\right)^2\zeta_+\left(1 - \zeta_+\zeta_-\right)} \\
&\quad + \frac{\zeta_+ - \zeta_-}{\left(\zeta_+^2 - 1\right)\zeta_+\left(1 - \zeta_+\zeta_-\right)^2} - \frac{2\zeta_+\left(\zeta_+ - \zeta_-\right)}{\left(\zeta_+^2 - 1\right)^2\left(1 - \zeta_+\zeta_-\right)} \qquad (3.52)\\
C_b &= \frac{1}{\left(1 - \zeta_+\bar{\zeta}_+\right)^2} \qquad (3.53)\\
C_c &= \frac{-1}{\left(\zeta_+ - \zeta_-\right)^2} \qquad (3.54)\\
C_d &= \frac{-1}{\left(1 - \zeta_+\bar{\zeta}_-\right)^2} \qquad (3.55)\\
C_e &= \frac{d^3Z_s}{d\zeta^3}/\frac{dZ_s}{d\zeta} - \left(\frac{d^2Z_s}{d\zeta^2}/\frac{dZ_s}{d\zeta}\right)^2 \qquad (3.56)\\
C_f &= 1/\frac{dZ_s}{d\zeta} \qquad (3.57)\\
C_g &= -\frac{d^2Z_s}{d\zeta^2}/\left(\frac{dZ_s}{d\zeta}\right)^2. \qquad (3.58)
\end{aligned}$$

The evolution for the linearized motion of the second vortex is similarly governed; simply exchange the subscripts + and −.

3.5.2 The numerical problem

In order to compute solutions to the linearized equations, we truncate the map perturbation (3.48) at $j = M - 2$ and the complex potential perturbation (3.49) at $j = M - 1$. We define as $\widehat{X}(t)$ the vector of unknown functions

$$\begin{aligned}
\widehat{X} = \{&\widehat{a}_{-1}, \Re(\widehat{a}_0)...\Re(\widehat{a}_{M-2}), \Im(\widehat{a}_0)...\Im(\widehat{a}_{M-2}), \Re(\widehat{b}_0)...\Re(\widehat{b}_{M-1}), \Im(\widehat{b}_1)...\Im(\widehat{b}_{M-1}), \\
&\Re(\widehat{\zeta}_1), \Im(\widehat{\zeta}_1), \Re(\widehat{\zeta}_2), \Im(\widehat{\zeta}_2)\}^T
\end{aligned} \qquad (3.59)$$

We evaluate the linearized boundary conditions, (3.46) and (3.47), at the discrete points $\zeta_k = \exp(i2k\pi/(M-1))$ for $k \in [0, M-1]$ to create a linear system of ODEs of the form

$$\mathbf{A}\frac{d\widehat{X}}{dt} = \mathbf{B}\widehat{X} \tag{3.60}$$

where $\mathbf{A}$ and $\mathbf{B}$ are two $2M-1 \times 2M-1$ real matrices. The substitution $\widehat{X}(t) = \widehat{X}_o e^{\sigma t}$ gives the generalized eigenvalue equation,

$$\sigma\mathbf{A}\widehat{X}_o = \mathbf{B}\widehat{X}_o. \tag{3.61}$$

Modes for which $\Re(\sigma) > 0$ are termed unstable. If $\Im(\sigma) \neq 0$ (hence the eigenvector $\widehat{X}_o$ is found to be complex) the solution of our differential equation is obtained by

$$\widehat{X}(t) = \Re\left(e^{\sigma t + i\varphi}\widehat{X}_o\right) \tag{3.62}$$

where φ is an arbitrary phase factor. Solutions to the generalized eigenvalue problem were obtained by use of the standard LINPACK routines.

3.5.3 Stability results and conclusions

Fixing the vortex strength γ/W_e (as 1/4, 3/4, 1 or 5/4) we computed the eigenvalues for a number of steady solutions corresponding to a range of the Bernoulli constant Ω. In every case we found unstable modes as well as a wide range of purely imaginary eigenvalues. An examination of the form of the computed eigenvectors shows that the perturbations may be classified as either symmetric or asymmetric. Recall that the bubble boundary perturbation is of the form

$$\widehat{Z}(\zeta, t) = \frac{\widehat{a}(t)_{-1}}{\zeta} + \sum_{j=0}^{\infty}\widehat{a}_j(t)\zeta^j \tag{3.63}$$

and that the perturbed vortices have the locations the non-physical plane

$$\zeta_+(t) \;=\; \zeta_+ + \epsilon\widehat{\zeta}_+(t) \tag{3.64}$$

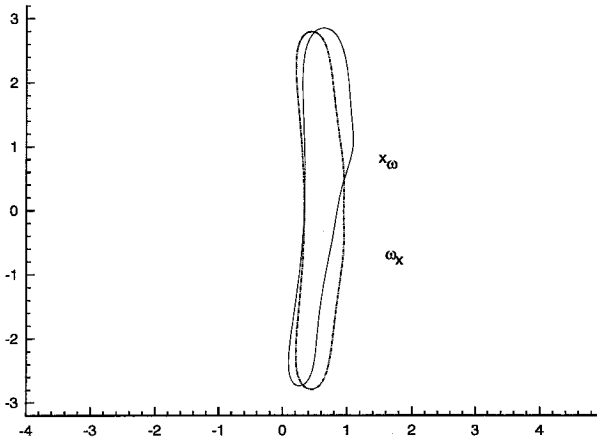

Figure 3.5: The tilting instability computed for $\gamma/W_e = 0.75$ and $\Omega = 0.07875$. The steady solution is shown for comparision, the steady vortex location is ω and x is the perturbed vortex location.

$$\zeta_-(t) \;=\; \bar{\zeta}_+ + \epsilon\widehat{\zeta}_-(t). \tag{3.65}$$

Those eigenfunctions of our linear equation for which all the expansion coefficients $\widehat{a}_j(t)$ are found to be real and $\widehat{\zeta}_+ = cong\left(\widehat{\zeta}_-\right)$, will be symmetric about the x-axis. For asymmetric perturbations the expansion coefficients $\widehat{a}_j(t)$ are imaginary and $\widehat{\zeta}_+ = -cong\left(\widehat{\zeta}_-\right)$.

The computed purely imaginary eigenvalues correspond to stable oscillations of the bubble shape. Both symmetric and asymmetric perturbations were found. Such oscillations in the presence of the vortex wake are a continuation of the symmetric and asymmetric stable modes computed by Nie and Tanveer [27] for a wakeless bubble.

The unstable modes are those for which the eigenvalue has a positive real part. Both purely real eigenvalues and complex unstable eigenvalues were computed. We assume that the eigenvalue with the largest real part will determine the dominant nature of the bubble's instability.

For any given steady bubble computed, exactly one positive real eigenvalue was calculated. An examination of the corresponding eigenmode shows the real eigenvalue corresponds to a generalization of the basic asymmetric instabilities calculated for the

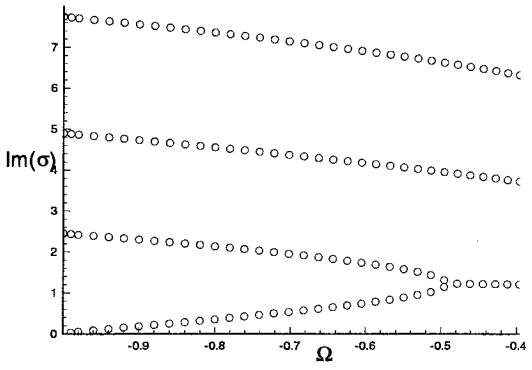

Figure 3.6: The imaginary part of the first four eigenvalues corresponding to symmetric perturbations for $\gamma/W_e = 0.75$

Föppl flow past a rigid elliptic cylinder: the bubble tilts as do the vortices as they are shed. Figure 3.5 is a plot of the perturbed boundary $Z = Z_s + \epsilon\widehat{Z}$, where $\widehat{Z}$ is the asymmetric unstable mode, and ϵ is taken to be 0.2 for effect.

On the other hand, for a given steady bubble, at most one complex unstable growth rate was computed. The complex instabilities were found to be symmetric perturbations. Recall that the form the perturbation for a complex growth rate involves an arbitrary phase factor as shown in expression (3.62). In figure 3.7 we have the boundaries corresponding to the addition of the steady solution with the unstable symmetric eigenmode evaluated with different phase factors. In this instability the point vortices spiral away from the steady locations and the bubble bends forward and back.

To gain insight into this symmetric instability we fix the vortex strength as $\gamma/W_e = 3/4$ and plot the first four symmetric eigenvalues as a function of Ω, see Figure 3.6. All four of these eigenvalues are initially purely imaginary; the upper three eigenvalues correspond to a continuation of the stable oscillation which exist in the absence of a vortex wake, the bottom eigenvalue relates to the stable symmetric perturbation of a vortex pair. The two higher eigenvalues displayed remain imaginary for the range of computed Ω. At $\Omega = -0.4781$ the two lower imaginary eigenvalues intersect at approximately $\sigma = i1.224$. For larger values of Ω these eigenmodes share an imaginary

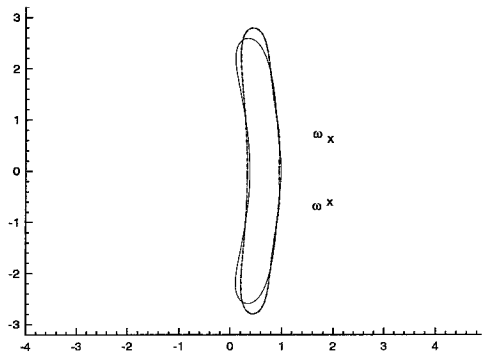

(a) $\varphi = 0$

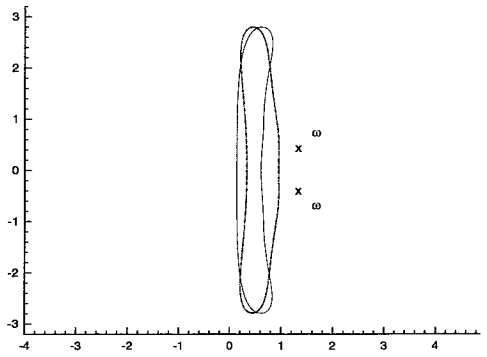

(b) $\varphi = \pi/2$

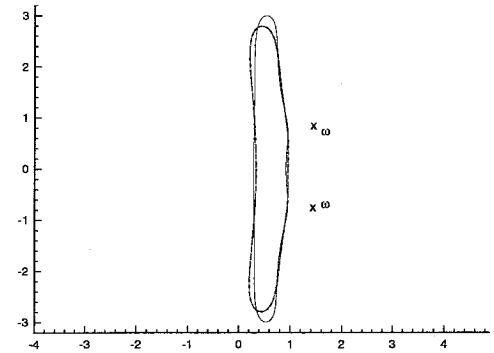

(c) $\varphi = \pi$

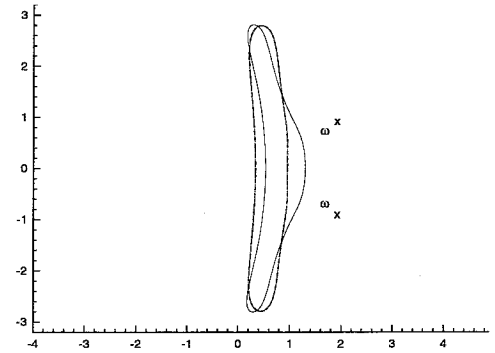

(d) $\varphi = 3\pi/2$

Figure 3.7: The oscillating symmetric instability computed for $\gamma/W_e = 0.75$ and $\Omega = 0.07875$. The steady solution is shown for comparision, the steady vortex location is ω and x is the perturbed vortex location.

part but have opposite real parts. We interpret this unstable symmetric perturbation as the cooperative interaction between the symmetric (stable) perturbations found in Föppl flow past a rigid elliptic cylinder with the symmetric (stable) oscillations of a wakeless bubble.

In Figures 3.8 (a) through (d) we have fixed value of the vortex strength, γ/W_e, and plotted the growth rate of the tilting eigenvalue, and the real part of the leading complex eigenvalue. We also present, in Figures 3.9 (a) through (d), plots of the imaginary part of the unstable complex eigenvalue. It was found that for small values of the Bernoulli constant Ω, corresponding to aspect ratios near unity, the tilting (real) instability dominated. As the Bernoulli constant increases the oscillating instability appears, and in some instances is the dominant instability.

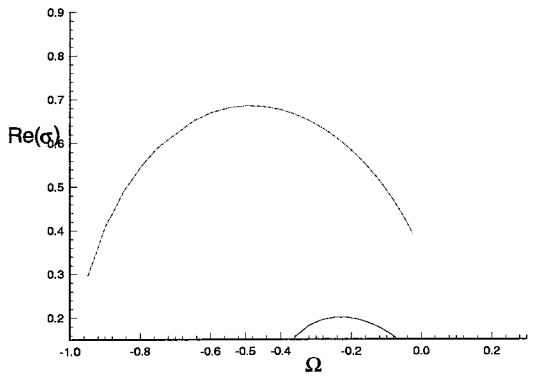

(a) $\gamma/W_e = 0.25$

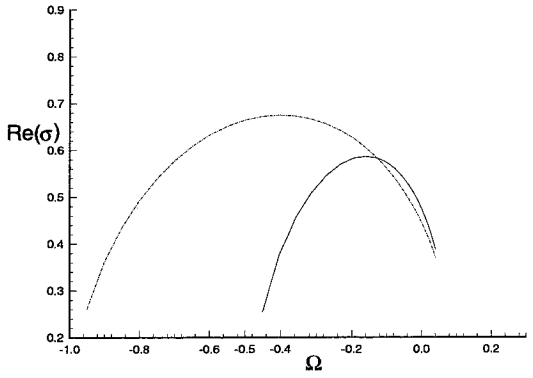

(b) $\gamma/W_e = 0.75$

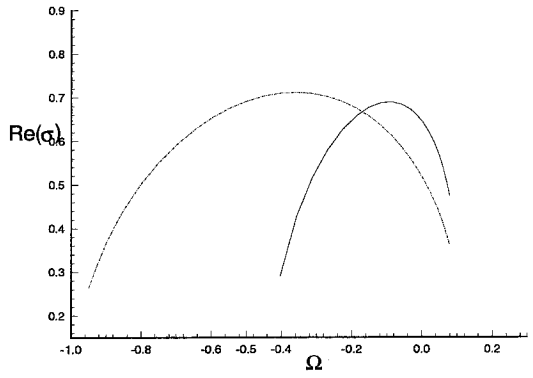

(c) $\gamma/W_e = 1.0$

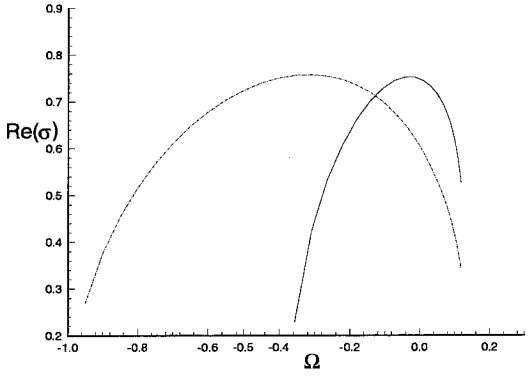

(d) $\gamma/W_e = 1.25$

Figure 3.8: The growth rates, $\Re(\sigma)$, for the two unstable modes as a function of the Bernoulli constant, Ω, with fixed vortex strength. The solid line corresponds to the symmetric instability and the dotted line is the asymmetric real instability.

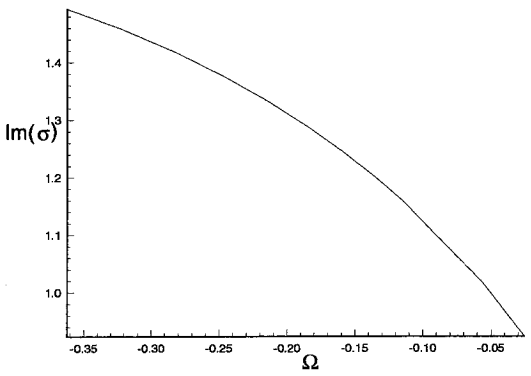

(a) $\gamma/W_e = 0.25$

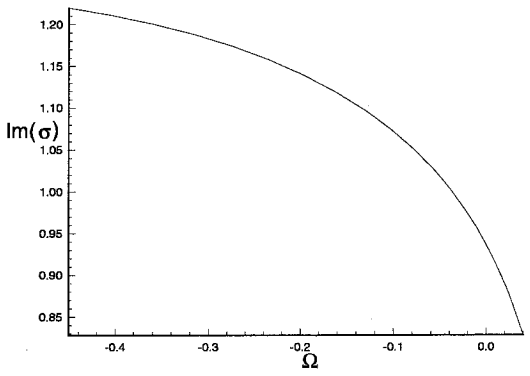

(b) $\gamma/W_e = 0.75$

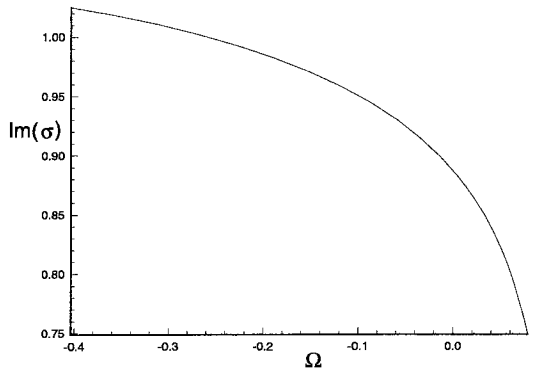

(c) $\gamma/W_e = 1.0$

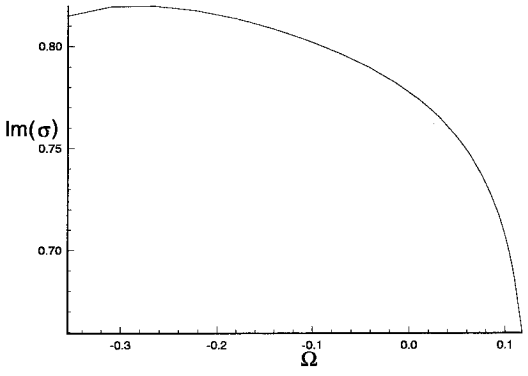

(d) $\gamma/W_e = 1.25$

Figure 3.9: The imaginary part, $\Im(\sigma)$, for the symmetric unstable mode as a function of the Bernoulli constant, Ω, with fixed vortex strength.

Chapter 4 Counter-Rotating vortex patches in shear

4.1 Introduction and the model system

We assume that the vortex sheet behind a lifting body has rolled up into two counter-rotating, parallel vortices. Typically, the separation distance between the vortices is an order of magnitude greater than their radius. To investigate the effects of a cross-stream shear on such a vortex configuration we examine the case of an ambient linear shear flow taken to be perpendicular to the vortex axes; we simplify our system by considering the flow as two dimensional with no variation along the length of the vortices. Furthermore, we assume the effects of viscosity and compressibility to be small and accordingly we neglect them. The two-dimensional incompressible Euler equations govern our system.

4.1.1 Point vortex model

One idealization of such a flow would be a point vortex system. Assuming delta functions of vorticity with strength $\pm\Gamma$ embedded in a linear shear flow of vorticity ω_∞ produces an instantaneous velocity field of the form

$$u - iv = i\frac{\omega_\infty}{2}(z - \bar{z}) + i\frac{\Gamma}{2\pi}\frac{1}{z - z_-} - i\frac{\Gamma}{2\pi}\frac{1}{z - z_+} \tag{4.1}$$

where, following standard complex notation, $z = x + iy$ and the overbar denotes the complex conjugate. Notice that the co-ordinate axes have been chosen with an orientation such that the shearing velocity is aligned with the x-axis and that the vortex located at $z_\pm$ has strength $\pm\Gamma$. The time-dependent locations of the vortices, z_+ and z_-, result from requiring each vortex to be advected by the shear and the

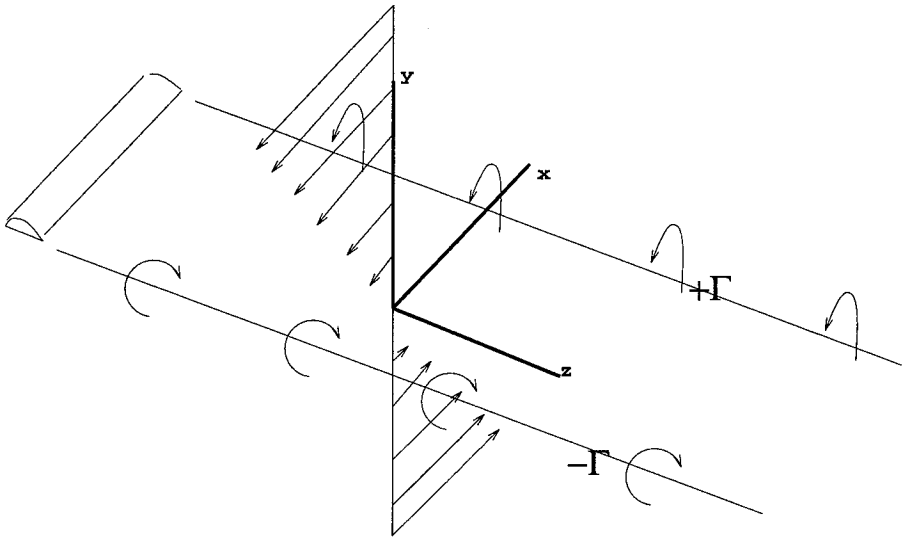

Figure 4.1: A simple sketch of trailing vortices with a cross shear perpendicular to the vortex axes.

velocity induced by the other vortex:

$$\frac{d}{dt}\bar{z}_+ = i\frac{\omega_\infty}{2}(z_+ - \bar{z}_+) + i\frac{\Gamma}{2\pi}\frac{1}{z_+ - z_-} \tag{4.2}$$

$$\frac{d}{dt}\bar{z}_- = i\frac{\omega_\infty}{2}(z_- - \bar{z}_-) + i\frac{\Gamma}{2\pi}\frac{1}{z_+ - z_-}. \tag{4.3}$$

It seems to have gone without notice in the literature that the general problem of a counter-rotating point vortex pair in arbitrary linear flow comprised of shear and strain can be analytically solved for any given initial condition. Such a solution is presented in Appendix C, but here we focus our attention on the simpler problem in which both the point vortices are initially on the x-axis and separated by a distance L, so that the mutually induced velocity of the vortex pair is orthogonal to the direction of the shear flow. For such initial conditions the equations (4.2) and (4.3) admit the solution

$$z_+ = \frac{\omega_\infty \Gamma}{4\pi L}t^2 + \frac{L}{2} - i\frac{\Gamma}{2\pi L}t \tag{4.4}$$

$$z_- = \frac{\omega_\infty \Gamma}{4\pi L}t^2 - \frac{L}{2} - i\frac{\Gamma}{2\pi L}t. \tag{4.5}$$

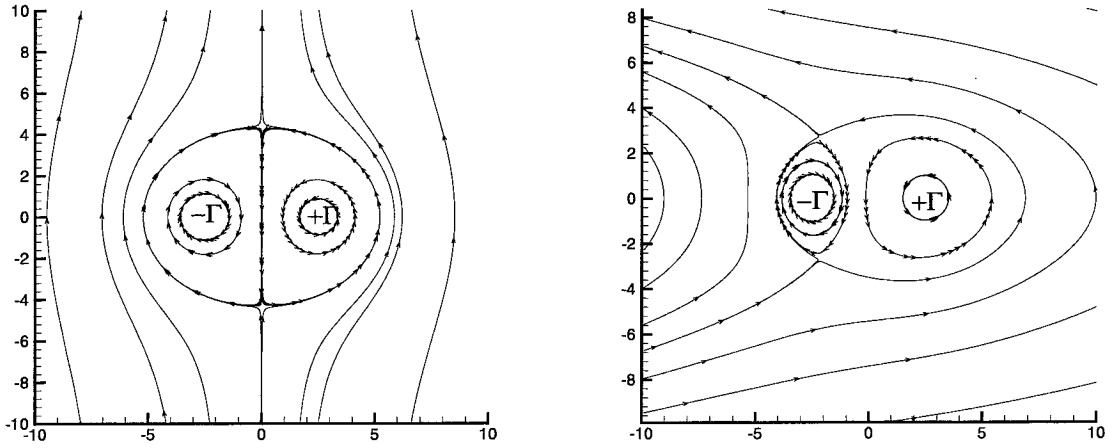

(a) No shear

(b) $\omega_\infty/\Gamma = 0.05$

Figure 4.2: The streamlines for point vortex pair in shear with $\Gamma = \pi$ and $L = 5$.

In this configuration the vortex initially at $+L/2$ has strength $+\Gamma$ and the strength of the vortex with initial location $-L/2$ is $-\Gamma$. Notice that the point vortices maintain a constant separation $z_+ - z_- = L$ while traversing a parabolic curve. Physically we anticipate $\Gamma > 0$, which implies that the vertical motion of the vortex pair is downward. In the frame of reference in which the point vortices are steady and located at $(x, y) = (\pm L/2, 0)$, the velocity field is given by

$$u - iv = -iV_\infty + i\frac{\omega_\infty}{2}(z - \bar{z}) + i\frac{\Gamma}{2\pi}\frac{1}{z + L/2} - i\frac{\Gamma}{2\pi}\frac{1}{z - L/2} \tag{4.6}$$

where $V_\infty = \Gamma/(2\pi L)$ balances the mutually induced downward velocity of the pair. In Figure (4.2) we present streamlines in the frame of the steady vortex pair. We observe that with the introduction of a shear with positive vorticity, the atmosphere of the $-\Gamma$ vortex decreases in size and is oriented with its major dimension parallel to the vertical axis. It is worth noting that while this solution of Euler's equation is not stable; infinitesimal perturbations only grow algebraically in time. For example

as part of the general solution, it is shown in Appendix C that

$$\tan\theta = \frac{\tan\theta_o}{1 - t\omega_\infty \tan\theta_o} \tag{4.7}$$

$$R = R_o \frac{\sin\theta_o}{\sin\theta} \tag{4.8}$$

where $z_+ - z_- = R\exp(i\theta)$. Since our steady solution corresponds to $(\theta_o, R_o) = (\pi, L)$, we see that perturbations which increase θ_o (rotate our vortex configuration counter-clockwise) are unstable with initially linear growth.

4.1.2 Vortex patch model

The point vortex model has a severe limitation; it is unable to predict instabilities of the vortex boundaries which in turn may lead to the destruction of a trailing vortex. The aim of this chapter is to study a generalization of the steady configuration. Specifically, instead of a point vortex, the cross-section of each trailing vortex is assumed to be a simply connected region of constant vorticity, referred to as a vortex patch. The constant shape of the patches and the mutually induced velocity, V_∞, are the unknowns for which we solve. Such solutions are obtained by following the methodology devised by Meiron, Saffman, and Shatzman [13], hereafter referred to as MSS.

In the frame of reference of the moving patches, the velocity field has the form

$$u - iv = -iV_\infty + i\frac{\omega_\infty}{2}(z - \bar{z}) + V_+(x - L/2, y) + V_-(x + L/2, y) \tag{4.9}$$

where $V_\pm$ are the velocities induced by each patch relative to their own centroid and tend to zero for large distances. It is assumed that the centroids have the same y coordinate. The curl of the velocity induced by a given patch is constant within the patch and zero outside of the patch. The patch of constant vorticity $+\omega_o$ induces the flow V_+ and has its centroid at $(x, y) = (+L/2, 0)$ while the patch with vorticity $-\omega_o$ is centered on $(-L/2, 0)$ and induces the flow V_-. To insure that the patches, like the point vortices, have equal effective strength in the shear flow, we require each patch

to have an equal magnitude of circulation relative to the shear vorticity ω_∞. This implies

$$(\omega_o - \omega_\infty) A_+ = (\omega_o + \omega_\infty) A_- \tag{4.10}$$

where A_+ is the area of the $+\omega_o$ patch and A_- gives the $-\omega_o$ patch area. Without loss of generality, we take ω_o and ω_∞ to be of the same sign. Solutions with the opposite direction of the shear, i.e. the other sign of ω_∞, may be obtained by a reflection of the flow about the y-axis.

One can show that for non-steady patch evolution, the vertical separation of the centroids of the patches will remain constant if the relative circulation relationship (4.10) is satisfied. Briefly, this result follows from that fact that the finite part of one component of the impulse is conserved, namely $\int_{All\ Space} y\,(\omega - \omega_\infty)\,dA = Const.$ By defining $y_\pm$ as the y coordinate of the $\pm\omega_o$ patch one can show that

$$y_+ - y_- = \frac{1}{(\omega_o - \omega_\infty) A_+} \int\limits_{All\ Space} y\,(\omega - \omega_\infty)\,dA - \frac{(\omega_o - \omega_\infty) A_+ - (\omega_o + \omega_\infty) A_-}{A_+ (\omega_o - \omega_\infty)} y_-. \tag{4.11}$$

It follows that

$$\frac{d\,(y_+ - y_-)}{dt} = -\frac{(\omega_o - \omega_\infty) A_+ - (\omega_o + \omega_\infty) A_-}{A_+ (\omega_o - \omega_\infty)} \frac{dy_-}{dt} \tag{4.12}$$

and we see that the vertical separation of the patches is a constant of the motion when the relative circulations of the patches are the same.

A dynamically consistent weak solution representing inviscid incompressible fluid flow must satisfy two conditions on the patch boundaries. First, the kinematic condition that the velocity be continuous everywhere including across the patch boundaries insures continuity of pressure. Second, the dynamic condition requires that the boundary of a given patch be a material surface. Let $Z\,(s,t)$ denote a parametric representation of the boundary of a patch so that requiring the difference between $\partial Z/\partial t$ and the fluid velocity at the boundary be parallel to the surface is equivalent

to the condition

$$\Im\left[\left\{\frac{\partial Z}{\partial t} - (u+iv)\right\}\frac{\partial \bar{Z}}{\partial s}\right] = 0. \tag{4.13}$$

By way of an introduction to the basic techniques we shall use, we begin with a derivation of the well known analytic equations, originally given in part by Chaplygyn [15] and rediscovered by Kida [8], which govern the evolution of a single elliptical patch embedded in a linear flow. Following this, we turn our attention to the problem at hand. A description of the two counter-rotating patches in shear is given in the form of general maps which define the patch boundaries. The direct calculation of the velocity induced by a given patch is discussed; by using Plemelj solutions to a Riemann-Hilbert problem the expressions of Contour Dynamics are derived as well as the Schwarz function expansion of the induced velocity. We then outline the numerical methods employed in determining steady patch shapes and formulate the equations which determine linear stability characteristics to two-dimensional boundary perturbations. Steady solutions are presented over a range of shear strengths for several fixed vortex separations. Confining our attention to perturbations which neither affect the areas nor displace the centroids of the patches; both a stable and an unstable solution branch are calculated. It is found that the eigenvalues agree well with the growth rates predicted by the dispersion relation Moore and Saffman [20] presented for a single patch. Based on the equations for a elliptically shaped patch in linear flow, a simple analytic model is formulated for the counter-rotating pair and its predictions are found to compare excellently with the numerics in the areas of study. Furthermore, from this elliptical patch model we are able to make some predictions about the nonlinear stability of the system. We show that certain initial conditions in the elliptical patch model evolve in such a way that the $-\omega_o$ patch is destroyed (its aspect ratio tends to infinity) while the $+\omega_o$ patch maintains its form.

4.2 An elliptical vortex patch in a linear background

Moore and Saffman [20] presented exact steady solutions of the Euler equation in the form of a single vortex patch of strength ω in the shape of an ellipse embedded in a linear background flow of strain and shear. They then used a representation in elliptical curvilinear co-ordinates to analyze stability to two-dimensional infinitesimal disturbances of the boundary shape; showing that the growth rate, μ, of an infinitesimal perturbation of mode number m to the boundary of a steady elliptic patch is given by

$$\left(\frac{\mu}{\omega}\right)^2 = -\frac{1}{4}\left\{\left(\frac{2m\lambda}{\lambda^2+1} - 1 + \frac{\omega_\infty}{\omega}\right)^2 - \left(1 - \frac{\omega_\infty}{\omega}\right)^2 \left(\frac{\lambda-1}{\lambda+1}\right)^{2m}\right\} \tag{4.14}$$

where $\lambda = a/b > 1$ is the aspect ratio of the patch and ω_∞ is the vorticity due to background shear. Kida [8] generalized Moore and Saffman's steady results by considering non-steady elliptic patches. He was able to demonstrate, by means of an ingenious transformation of the Kirchhoff vortex, that in the absence of perturbations a non-steady patch which is initially elliptic and embedded in linear flow remains elliptic. In doing so, Kida formulated differential equations, originally given by Chaplygyn [15], which describe the evolution of the orientation and aspect ratio of an elliptic patch embedded in a linear flow.

In this section we derive the equations which govern an elliptic vortex patch in a background flow consisting of linear shear and an arbitrarily oriented strain. Rather than following Kida's approach, we will use a Schwarz function method which we may easily generalize to multiple patches. While this example serves illustrative purposes, the results will be utilized later in this chapter as building blocks of a simple analytic approximation to the problem of a counter-rotating vortex pair in shear.

The constant vorticity in the background shear is taken as ω_∞ and the vorticity in the patch has the value ω_o. We exclude the trivial case of $\omega_o = \omega_\infty$. In the standard

complex notation, we take the background shear and strain field to be of the form

$$u_B - iv_B = i\frac{\omega_\infty}{2}(z - \bar{z}) + \sigma e^{i\phi} z \tag{4.15}$$

where ω_∞, σ, and ϕ are real. The first term represents a linear shear and the second term defines a straining flow. External to the patch the complex velocity is assumed to be of the form

$$u_E - iv_E = -\frac{i}{2}(\omega - \omega_\infty) G(z) + u_B - iv_B \tag{4.16}$$

where $G(z)$ is analytic outside the patch and its product with $-i(\omega_o - \omega_\infty)/2$ represents the induced flow due to the patch. While inside the patch the velocity has the form

$$u_I - iv_I = \frac{i}{2}(\omega - \omega_\infty) F(z) - i\frac{\omega_o}{2}\bar{z}, \tag{4.17}$$

and the function $F(z)$ is analytic within the patch.

In order to obtain solutions of Euler's equation, we begin by deriving the general form of the velocity induced by an arbitrarily shaped vortex patch. We then calculate the simple analytic form of this velocity for the case of an elliptic patch and impose a dynamic condition at the boundary of the patch to arrive at ordinary differential equations which govern the elliptic patch.

To find the velocity induced by the patch we impose continuity of velocity across the patch boundary, this implies

$$F(z) + G(z) + C_o z = \bar{z} \tag{4.18}$$

on the boundary. The constant C_o is given by

$$C_o = i2\frac{\left(i\omega_\infty/2 + \sigma e^{i\phi}\right)}{(\omega - \omega_\infty)}. \tag{4.19}$$

Notice that the function $G^+(z) \equiv G(z)$ is analytic everywhere outside of the patch, and the function $G^-(z) \equiv -F(z) - C_o z$ is analytic within the patch. We may now

re-write the continuity of velocity in the familiar form of a Riemann-Hilbert problem,

$$G^{+}(z) - G^{-}(z) = \bar{z} \tag{4.20}$$

on the patch boundary ∂A with the requirements that G^{+} be analytic exterior to the patch and decay for large z, while G^{-} be analytic everywhere within the boundary. In essence by identifying G^{+} and G^{-} we are splitting a function which is assumed to be analytic in the neighborhood of a closed curve with prescribed values of $\bar{z}(z)$ on the curve. Such a function is called a Schwarz function. The Schwarz function approach was originally suggested by Jimenez and implemented by MSS who found the induced flows by examining Laurent series. Here we note this problem may be simply solved by use of the Plemelj formula: for points outside the patch

$$G^{+}(z) = \frac{1}{2\pi i} \oint_{\partial A} \frac{-\bar{z}(\hat{z})}{\hat{z} - z} d\hat{z}, \tag{4.21}$$

while inside the patch

$$G^{-}(z) = \frac{1}{2\pi i} \oint_{\partial A} \frac{-\bar{z}(\hat{z})}{\hat{z} - z} d\hat{z}. \tag{4.22}$$

We see that for an arbitrarily shaped patch the velocity induced by the patch may be calculated as

$$u - iv = \frac{(\omega - \omega_{\infty})}{4\pi} \oint_{\partial A} \frac{\bar{z}(\hat{z})}{\hat{z} - z} d\hat{z}. \tag{4.23}$$

One could use Green's formula to derive from (4.23) the standard integrals of Contour Dynamics.

We now assume that the boundary of the patch is an ellipse. The boundary is the image in the z-plane of the unit circle in the ζ-plane under the map

$$z = \alpha\zeta + \beta/\zeta. \tag{4.24}$$

We define a as the length of major axis of the ellipse and b as the length of minor axis. The area of the ellipse is then given by πab. Measuring counter-clockwise from the positive x-axis to the major axis gives the angle θ. These three real quantities

are related to the complex map coefficients by

$$a\exp(i\theta) = \alpha+\beta \tag{4.25}$$

$$b\exp(i\theta) = \alpha-\beta. \tag{4.26}$$

To compute the induced velocity (4.23), we note that on the boundary of the patch

$$\bar{z} = \bar{\alpha}/\zeta + \bar{\beta}\zeta, \tag{4.27}$$

so that the induced velocity may be calculated as

$$u - iv = \frac{(\omega-\omega_\infty)}{4\pi}\oint_{|\zeta|=1}\frac{\left(\bar{\alpha}/\zeta+\bar{\beta}\zeta\right)}{(\alpha\zeta+\beta/\zeta-z_p)}\left(\alpha-\beta/\zeta^2\right)d\zeta. \tag{4.28}$$

After performing minor algebraic manipulations and evaluating the residue, we find that the induced flow for points outside of the patch is given by

$$u - iv = -i(\omega-\omega_\infty)\frac{ab}{z+\sqrt{z^2-4\alpha\beta}}. \tag{4.29}$$

By construction, the square root is continuous outside the patch and tends to z for large distances. The branch points $\pm 2\sqrt{\alpha\beta} = \pm\sqrt{a^2-b^2}\exp(i\theta)$ are on the major axis within the patch; the branch cut connects the branch points and remains in the patch. The complex velocity field outside and on the boundary of an elliptic vortex patch in a linear background flow is given by the following expression,

$$u_E - iv_E = -i(\omega-\omega_\infty)\frac{ab}{z+\sqrt{z^2-4\alpha\beta}} + i\frac{\omega_\infty}{2}(z-\bar{z}) + \sigma e^{i\phi}z. \tag{4.30}$$

On the boundary of the patch, this velocity can be expressed simply in terms of ζ as

$$u_E - iv_E = -i(\omega-\omega_\infty)\frac{ab}{2\alpha\zeta} + i\frac{\omega_\infty}{2}\left(\alpha\zeta+\beta/\zeta-\bar{\alpha}/\zeta-\bar{\beta}\zeta\right) + (\alpha\zeta+\beta/\zeta)\,\sigma e^{i\phi} \tag{4.31}$$

by means of the map (4.24).

Dynamically, the evolution of the vortex patch is governed by the requirement

that the boundary be a material line. That is to say the boundary of the patch moves with the flow. If s parameterizes the patch such that $Z(s,t)$ defines the boundary, the dynamic condition is equivalent to

$$\Im\left[\left\{\frac{\partial Z}{\partial t} - (u_E + iv_E)\right\}\frac{\partial \bar{Z}}{\partial s}\right] = 0 \tag{4.32}$$

evaluated on the patch boundary. We parameterize the patch by making the identification $\zeta = \exp(is)$ in the map (4.24) and we assume that the patch maintains elliptical form so that only the coefficients α and β are allowed to evolve with time. We will justify this assumption by finding closed equations for the evolution of α and β. In terms of ζ the tangent to boundary and the velocity of the boundary take the forms

$$\frac{\partial Z}{\partial s} = i\alpha\zeta - i\beta/\zeta \tag{4.33}$$

$$\frac{\partial Z}{\partial t} = \dot{\alpha}\zeta + \dot{\beta}/\zeta \tag{4.34}$$

where the overdot indicates the derivative with respect to time.

Substitution of (4.31) and (4.34) into (4.32) leads to an expression of the form

$$\bar{c}_2/\zeta^2 + c_o + c_2\zeta^2 = 0 \tag{4.35}$$

where c_o is real but c_2 is in general complex. Requiring $c_o = 0$ leads to conservation of area

$$\frac{d}{dt}(ab) = 0, \tag{4.36}$$

while $c_2 = 0$ gives an equation for the evolution of the aspect ratio, $\lambda = a/b$,

$$\frac{d}{dt}(\lambda) = 2\lambda\left(\sigma\cos(2\theta + \phi) - \frac{\omega_\infty}{2}\sin 2\theta\right) \tag{4.37}$$

and the patch orientation

$$\frac{d}{dt}\theta = \frac{\lambda}{(\lambda+1)^2}(\omega - \omega_\infty) + \frac{\omega_\infty}{2}\left(1 - \cos 2\theta \frac{\lambda^2+1}{\lambda^2-1}\right) - \frac{\lambda^2+1}{\lambda^2-1}\sigma \sin(2\theta + \phi). \quad (4.38)$$

These three differential equations, (4.36),(4.37), and (4.38), form a closed system describing the evolution of a vortex patch of elliptic shape in a linear flow; equivalently they determine α and β. The steady elliptic patches investigated by Moore and Saffman [20] corresponds to the stationary solutions of these equations. In the absence of strain, an examination of the steady equations shows that only for a finite range of ω_∞/ω_o are there steady solutions. In particular, two steady patch solutions of different aspect ratios exist when ω_∞/ω_o is in the range $\left\{\left(1-\sqrt{2}\right)/2, 0\right\}$ and only one solution when $\omega_\infty/\omega_o \in \{0, 1\}$.

4.3 The numerical approach

In this section we directly calculate the steady shapes and linear stability of counter-rotating vortex pairs in linear shear. In doing so we follow the basic approach implemented by MSS. As in the previous section, we express the boundary of each patch relative to its own centroid as a map of the unit circle and by requiring the coefficients in an expansion of the boundary conditions to be zero we satisfy the condition that patch boundaries be material lines. We also use a Schwarz function approach to calculate the flow induced by each patch, although a summation representation is chosen rather than the integral form of (4.23).

Recall that we are seeking the steady shapes of two counter-rotating vortex patches of constant vorticities $\pm\omega_o$ embedded in a background flow of the form

$$u - iv = -iV_\infty + i\frac{\omega_\infty}{2}(z - \bar{z}) \quad (4.39)$$

where the centroids are located on the x-axis separated by a fixed distance L. Ex-

plicitly, we take $z = +L/2$ to be the centroid of the $+\omega_o$ patch and $z = -L/2$ to be the centroid of the other patch. By counter-rotating, we mean that each patch has an area which gives it an equal strength relative to the background shear. To insure this, the area A_- of the $-\omega_o$ patch equals the area A_+ of the $+\omega_o$ patch scaled by $(\omega_o - \omega_\infty) / (\omega_o + \omega_\infty)$. The circulation due to a given patch beyond the value produced by the background shear has the magnitude $\Gamma = (\omega_o - \omega_\infty) A_+$. The shape of the vortex with vorticity $+\omega_o$ is assumed to be adequately described by a conformal map of the unit circle $|\zeta| = 1$ of the form

$$z_+ = R_+ \zeta \left\{ 1 + \sum_{j=1}^{N} \frac{a_{j,+}}{\zeta^j} \right\} \tag{4.40}$$

while the boundary of the vortex $-\omega_o$ has the expansion

$$z_- = R_- \zeta \left\{ 1 + \sum_{j=1}^{N} \frac{a_{j,-}}{\zeta^j} \right\}. \tag{4.41}$$

We anticipate that $z_+, z_- = 0$ corresponds to the patch centroids. These expansion coefficients and the vortex induced mutual velocity V_∞ are the unknowns of the system. The boundary shapes will result from requiring the boundary to be a material line. Before discussing the resulting system of equations, we describe the method of computing the flow induced by a patch. We choose not to perform the direct numerical integration suggested by the boundary integral form of the induced flow. Instead we use the exact analytic technique of arbitrary accuracy employed by MSS.

4.3.1 The induced flow

Given a vortex patch of vorticity ω embedded in a background flow with constant vorticity ω_∞, the flow external to the patch of arbitrary shape has the form

$$u_E - i v_E = -\frac{i}{2} (\omega - \omega_\infty) G^E(z) + i \frac{\omega_\infty}{2} (z - \bar{z}) + H(z), \tag{4.42}$$

and

$$u_I - iv_I = -\frac{i}{2}(\omega - \omega_\infty) G^I(z) + i\frac{\omega_\infty}{2} z - i\frac{\omega}{2}\bar{z} + H(z) \tag{4.43}$$

in the patch. The function $H(z)$ represents some locally analytic flow, perhaps induced by other patches. Continuity of velocity implies, by means of the Plemelj formulae,

$$G^E(z) = \frac{1}{2\pi i}\oint_{\partial A} \frac{-\bar{z}(\hat{z})}{\hat{z} - z} d\hat{z} \tag{4.44}$$

$$G^I(z) = \frac{1}{2\pi i}\oint_{\partial A} \frac{-\bar{z}(\hat{z})}{\hat{z} - z} d\hat{z} \tag{4.45}$$

where ∂A defines the boundary of the patch. Briefly, we relate our induced flow to a more common form, often found in Contour Dynamics, which reflects a summation of point vortices; by use of Green's theorem and Cauchy's theorem, we have for points z outside the patch

$$\frac{1}{2\pi i}\oint_{\partial A} \frac{-\bar{z}(\hat{z})}{\hat{z} - z} d\hat{z} = -\frac{1}{\pi}\iint_A \frac{d\hat{x}d\hat{y}}{\hat{z} - z}. \tag{4.46}$$

We can represent the induced velocities as sums whose coefficients have simple geometric interpretations. For large $|z|$ we can expand the integrand in G^E as a geometric sum

$$G^E(z) = \sum_{j=1} g_j z^{-j} \tag{4.47}$$

where

$$g_j = \frac{1}{2\pi i}\oint_{\partial A} z^{j-1}\bar{z} dz. \tag{4.48}$$

Likewise for small $|z|$ we can express G^I as

$$G^I(z) = -\sum_{j=0} f_j\, z^j \tag{4.49}$$

with

$$f_j = \frac{1}{2\pi i}\oint_{\partial A} z^{-j-1}\bar{z} dz. \tag{4.50}$$

Notice that if the function $\bar{z}(z)$ which takes the value $\bar{z}$ on the patch boundary has

a convergent Laurent series we would find

$$\bar{z}(z) = \sum_{j=1} g_j / (z)^j + \sum_{j=0} f_j \, z^j. \tag{4.51}$$

MSS provide a geometric interpretation for the coefficients g_j as moments of the shape of the vortex since

$$g_j = \frac{1}{2\pi i} \oint_{\partial A} z^{j-1} \bar{z} dz = \frac{1}{\pi} \iint_A (\hat{z})^{j-1} \, d\hat{x} d\hat{y}. \tag{4.52}$$

Notice that g_2 is proportional to the patch centroid, while πg_1 gives the patch area.

For the purposes of our numerical scheme, we choose to use the summation representation (4.47) in our calculations of the induced flow. To precisely calculate coefficients in the expansion of $u \pm iv$, we observe that the equation (4.48) for g_j taken with an expansion of the boundary $z(\zeta, t)$ in terms of ζ implies that

$$g_j = \text{coefficient of } \zeta^{-1} \text{ in the product } z^{j-1} \bar{z} \frac{dz}{d\zeta} \tag{4.53}$$

and

$$\bar{g}_j = -\text{coefficient of } \zeta^{-1} \text{ in the product } \bar{z}^{j-1} z \frac{d\bar{z}}{d\zeta}. \tag{4.54}$$

From the assumed forms of the shape expansions, (4.40) and (4.41), these quantities may be easily computed.

4.3.2 The steady system

The fact that the steady boundary of a patch is a material line, implies that at the boundary there is no normal fluid flow. Combining the induced flows calculated from the two patch shapes, (4.40) and (4.41), with the background flow, the velocities on the boundaries of patch $+\omega_o$ and $-\omega_o$ are respectively given by

$$u_+ - iv_+ = -iV_\infty + i\frac{\omega_\infty}{2}(z_+ - \bar{z}_+) + i\frac{\Gamma}{2}\left(\frac{1}{A_+} G_+^E(z_+) - \frac{1}{A_-} G_-^E(z_+ + L)\right) \tag{4.55}$$

$$u_- - iv_- = -iV_\infty + i\frac{\omega_\infty}{2}(z_- - \bar{z}_-) + i\frac{\Gamma}{2}\left(\frac{1}{A_+}G_+^E(z_- - L) - \frac{1}{A_-}G_-^E(z_-)\right) \quad (4.56)$$

where $G_+^E(z)$ is induced by the $+\omega_o$ patch and relative to its centroid, similarly $G_-^E(z)$ results from the $-\omega_o$ patch. Our steady boundary conditions implied by the kinematic condition may be expressed as

$$B_+(\zeta) \equiv (u_+ - iv_+)\frac{\partial z_+}{\partial \zeta}\zeta - (u_+ + iv_+)\frac{\partial \bar{z}_+}{\partial \zeta}\zeta = 0 \quad (4.57)$$

$$B_-(\zeta) \equiv (u_- - iv_-)\frac{\partial z_-}{\partial \zeta}\zeta - (u_- + iv_-)\frac{\partial \bar{z}_-}{\partial \zeta}\zeta = 0 \quad (4.58)$$

to be satisfied when $|\zeta| = 1$.

Unfortunately the summation which represents the velocitiy induced by a given patch may not converge on the boundary of that patch. If the sum (4.47) represents the velocity induced by a patch relative to the patch centroid, its domain of convergence will be $|z| \geq c_r$ where c_r is some critical radius. Such a critical radius is related to the branch points of the inverse of the function which maps the unit circle to the boundary. While all of these branch points are assumed to be within the patch, if the patch is far from circular there may be points on the patch boundary with magnitude less than c_r. To overcome this problem, we use the boundary expansion to re-express the velocity sum in terms of powers of ζ when evaluated on the patch boundary. One could think of this as evaluating the velocity in the ζ-plane where the patch is circular and the velocity sum converges everywhere on the boundary.

To form the numerical system corresponding to the steady equations we follow MSS by treating the shape coefficients and their conjugates as independent variables which creates $4N + 4$ complex unknowns: $R_+, a_{1+}, \ldots a_{N+}, \bar{R}_+, \bar{a}_{1+}, \ldots \bar{a}_{N+}$, and $R_-, a_{1-}, \ldots a_{N-}, \bar{R}_-, \bar{a}_{1-}, \ldots \bar{a}_{N-}$. We have two additional complex unknowns in the form of V_∞ and $\bar{V}_\infty$ which represent the mutually induced velocity of the pair. Steady solutions are obtained by Newton iteration, and only those in which $a_{j\pm} = conjugate(\bar{a}_{j\pm})$, $V_\infty = conjugate(\bar{V}_\infty)$ and $R_\pm = conjugate(\bar{R}_\pm)$ will have physical meaning. Such an approach simplifies the later stability calculation. The induced velocities are approximated by truncating the associated summations (4.47)

to include M terms where M is some integer chosen such that $M \geq N$.

In essence our numerical approach is a spectral method. Our system of equations result from expanding the boundary conditions, (4.57) and (4.58), as Laurent series in $\zeta = \exp(is)$;

$$B_+(\zeta) = \sum_{j=1} \frac{B_{-j,+}}{\zeta^j} + B_{0,+} + \sum_{j=1} B_{j,+}\zeta^j = 0 \tag{4.59}$$

$$B_-(\zeta) = \sum_{j=1} \frac{B_{-j,-}}{\zeta^j} + B_{0,-} + \sum_{j=1} B_{j,-}\zeta^j = 0, \tag{4.60}$$

and equating the first $2N+1$ coefficients with zero:

$$B_{j,+} = 0,\ B_{j,-} = 0 \quad (-N \leq j \leq N). \tag{4.61}$$

This provides $4N+2$ equations. In calculating these boundary condition coefficients, it is necessary on the boundary of each patch to express the velocity field induced by the other patch in powers of ζ. For example, we assume the summation form of G_-^E converges on the boundary of the $+\omega_o$ patch and use a discrete Fourier transform to expand $G_-^E(z_+ + L)$ in terms of $\zeta = \exp(is)$. To insure that the vortices are separated by a distance L, we require that the local origins within each patch coincide with the centroid of that patch; we treat this requirement as 4 complex equations

$$g_{2,+} = \bar{g}_{2,+} = g_{2,-} = \bar{g}_{2,-} = 0. \tag{4.62}$$

Two further equations result from the condition that the vortex patches have given areas;

$$A_+ = \pi R_+ \bar{R}_+ \left\{ 1 - \sum_{j=2}^{N} (j-1)(a_{j,+})(\bar{a}_{j,+}) \right\} \tag{4.63}$$

$$A_- = \pi R_- \bar{R}_- \left\{ 1 - \sum_{j=2}^{N} (j-1)(a_{j,-})(\bar{a}_{j,-}) \right\}. \tag{4.64}$$

Notice that within the maps defining the boundaries, the phase of ζ is arbitrary; this

is fixed by specifying the phases of R_+ and R_-. In particular, we will seek steady solutions in which R_+ and R_- are real:

$$R_+ = \bar{R}_+, \quad R_- = \bar{R}_-. \tag{4.65}$$

We briefly discuss the hidden constraints of the system. At this point we have $4N+10$ equations for $4N+6$ unknowns. In their paper MSS identified dependencies within the system of equations. A necessary observation is that the flow across ds, an infinitesimal length of a vortex boundary, is given by $u_n ds = B(\zeta)\, d\theta/2$, where u_n is the component of the fluid velocity normal to the boundary. Since the velocity field constructed is divergence free this implies

$$0 = \oint u_n ds = \int_0^{2\pi} B(\zeta)\, d\theta \tag{4.66}$$

and hence $B_{0,+}$ and $B_{0,-}$ are automatically zero. Since our system contains background vorticity in the form of linear shear, we modify the arguments of MSS to obtain further constraints. By identifying $\mathbf{a}$ with the velocity field minus the shear flow in the vector identity

$$\mathbf{a}\times(\boldsymbol{\nabla}\times\mathbf{a}) = \frac{1}{2}\boldsymbol{\nabla}\left(\mathbf{a}^2\right) - \mathbf{a}\cdot\boldsymbol{\nabla}\mathbf{a} \tag{4.67}$$

one can show that for our two-dimensional flow

$$\iint\limits_{\text{all fluid}} (\mathbf{u} + \omega_\infty y\mathbf{i}) \times (\boldsymbol{\omega} - \omega_\infty \mathbf{k})\, dxdy = 0. \tag{4.68}$$

This results from an application of Green's theorem in which the resulting surface integrals are taken to be at infinity. Recall that the patches have vorticity $\pm\omega_o$ so that equation (4.68) becomes

$$(\omega_o - \omega_\infty) \iint\limits_{A_+} (\mathbf{u} + \omega_\infty y\mathbf{i})\, dxdy - (\omega_o + \omega_\infty) \iint\limits_{A_-} (\mathbf{u} + \omega_\infty y\mathbf{i})\, dxdy = 0. \tag{4.69}$$

The y components of the patch centroids are equal to zero by our placement of the patches on the x-axis, so the integrations $\iint_A y\, dxdy$ contribute nothing. Another application of Green's theorem leads to

$$(\omega_o - \omega_\infty) \oint_{\partial A_+} \mathbf{x} u_n ds - (\omega_o + \omega_\infty) \oint_{\partial A_-} \mathbf{x} u_n ds = 0. \tag{4.70}$$

This equation may be expressed as

$$(\omega_o - \omega_\infty) \int_0^{2\pi} (z_+ \pm \bar{z}_+) B_+ (\zeta) - (\omega_o + \omega_\infty) \int_0^{2\pi} (z_- \pm \bar{z}_-) B_- (\zeta)\, d\theta = 0. \tag{4.71}$$

This is obviously a constraint between all the coefficients $B_{j,+}$ and $B_{j,-}$. If we apply the directly imposed boundary condition $B_+ (\zeta) = 0$, this implicit constraint (4.71) along with the boundary expansion for the second patch(4.41) gives

$$B_{-1,-} \pm B_{1,-} + \sum_{j=2} [a_{j,-} B_{j-1,-} \pm \bar{a}_{j,-} B_{1-j,-}] = 0 \tag{4.72}$$

where $a_{j,-}$ and $\bar{a}_{j,-}$ are the assumed small expansion coefficients in z_- and $\bar{z}_-$. We now see that is sufficient to eliminate our explicit equations $B_{-1,-} = B_{1,-} = 0$, as a converged solution of the reduced set of equations will automatically satisfy these conditions. We now have a system with $4N + 6$ equations and unknowns, which we solve by Newton iteration with an analytic Jacobian.

4.3.3 The stability calculation

In this subsection we formulate the equations which govern the response of a computed steady vortex patch pair to infinitesimal two-dimensional perturbations of the patch boundaries. Given that $Z(s,t)$ describes a boundary of a patch, the unsteady condition that the vortex boundaries are material lines takes the form

$$\Im \left[\left\{ \frac{\partial Z^*}{\partial t} - (u - iv) \right\} \frac{\partial Z}{\partial s} \right] = 0. \tag{4.73}$$

Using primed quantities to denote the perturbations, we assume that a perturbed boundary and its conjugate are of the form

$$Z = z(s) + z'(s,t) \tag{4.74}$$

$$\bar{Z} = z^*(s) + \hat{z}'(s,t) \tag{4.75}$$

where z denotes the undisturbed steady solution and z^*, its conjugate. Since the velocity field is determined in part by the shape of a given vortex patch, perturbing a patch produces a corresponding disturbance in the velocities. Linearization of expression (4.73) and the identification $\zeta = \exp(is)$ produces the equation

$$\frac{d\hat{z}'}{dt}\zeta\frac{dz}{d\zeta} - \frac{dz'}{dt}\zeta\frac{dz^*}{d\zeta} = \left\{\left(u' - iv'\right)\frac{dz}{d\zeta} - \left(u' + iv'\right)\frac{dz^*}{d\zeta} + (u - iv)\frac{dz'}{d\zeta} - (u + iv)\frac{d\hat{z}'}{d\zeta}\right\}\zeta \tag{4.76}$$

to be satisfied on the vortex boundary.

We introduce the disturbances to the steady shapes by perturbing the coefficients in the maps which describe the boundaries. We assume, for example, that the perturbation to the steady patch defined by z_+ in equation (4.40) has the expansion

$$z'_+ = R'_+(t)\,\zeta\left\{1 + \sum_{j=1}^{N}\frac{a_{j,+}}{\zeta^j}\right\} + R_+\zeta\sum_{j=1}^{N}\frac{a'_{j,+}(t)}{\zeta^j} \tag{4.77}$$

and that the perturbation of the conjugate of the steady patch, $\bar{z}_+$, is given by

$$\hat{z}'_+ = \hat{R}'_+(t)\,\frac{1}{\zeta}\left\{1 + \sum_{j=1}^{N}a^*_{j,+}\zeta^j\right\} + R^*_+\frac{1}{\zeta}\sum_{j=1}^{N}\hat{a}'_{j,+}(t)\,\zeta^j. \tag{4.78}$$

Similar expansions with the coefficients $R'_-, \hat{R}'_-, a'_{j,-}, \hat{a}'_{j,-}$ are assumed for the perturbation to the boundary of the other steady patch. We explicitly note that the response of the velocities to a perturbation of the vortex boundaries can be expressed in terms of these perturbation coefficients, for example to calculate the infinitesimal

velocity change produced by a perturbation of the boundaries

$$u' - iv' = \left\{ R'_+ \frac{d}{dR_+} + R'_- \frac{d}{dR_-} + \hat{R}'_+ \frac{d}{dR^*_+} + \hat{R}'_- \frac{d}{dR^*_-} \right\} (u - iv) \tag{4.79}$$
$$+ \sum_j^N \left\{ a'_{j,+} \frac{d}{da_{j,+}} + a'_{j,-} \frac{d}{da_{j,-}} + \hat{a}'_{j,+} \frac{d}{da^*_{j,+}} + \hat{a}'_{j,-} \frac{d}{da^*_{j,-}} \right\} (u - iv) .$$

We see that by means of expansions like (4.77),(4.78) and (4.79), the boundary condition on each patch, (4.76), is linear in the unknown time-dependent perturbation coefficients. Solutions are searched for in which all primed quantities are proportional to $exp(\sigma t)$. In doing so, we choose to treat z' and $\hat{z}'$ as independent functions producing $4N+4$ unknowns. Representing these unknowns, $R'_+, a'_{j,+}, R'_-, a'_{j,-}, \hat{R}'_+, \hat{a}'_{j,+}, \hat{R}'_-, \hat{a}'_{j,-}$ by a vector $\boldsymbol{\phi}$ allows the linear condition on each boundary to take the form of a generalized eigenvalue equation

$$\sigma \mathbf{N}(\zeta) \boldsymbol{\phi} = \mathbf{M}(\zeta) \boldsymbol{\phi}. \tag{4.80}$$

In a manner similar to that used in the computations of the steady boundaries, $4N+2$ equations are obtained by expanding the linear boundary conditions as Laurent series and equating the coefficients of ζ^n to zero for n in the range $-N \leq n \leq N$. Two of the unknowns of our system are eliminated by fixing the phase of the perturbations by requiring $R'_+ = \hat{R}'_+$ and $R'_- = \hat{R}'_-$. The stability problem has now been reduced to calculating the eigensytem of a $4N+2$ generalized system. Only perturbations which do not affect the patch areas will be considered in assessing the stability of the configuration.

At this point we make a comment to justify our treatment of z' and $\hat{z}'$ as independent functions. If a physically realistic perturbation has the form $z'_p = fe^{\sigma t} + g^* e^{\sigma^* t}$ then its actual complex conjugate would be $z^{*'}_p = ge^{\sigma t} + f^* e^{\sigma^* t}$. As the time exponentials are linearly independent our method will compute the two related solutions, $(z', \hat{z}') = e^{\sigma t}(f, g)$ and $(z', \hat{z}') = e^{\sigma^* t}(g^*, f^*)$, from which we could re-create the physical perturbation modes.

4.3.4 Numerical results

The steady equations were solved by Newton's method with an analytic Jacobian. Most computations were done with $N = 15$ shape coefficients for each vortex, and were duplicated with double the number of unknowns. It was found that $N = 15$ was sufficient for obtaining solutions with double precision accuracy. Only seconds were required on a Sun Sparc5 workstation to compute a steady solution.

In performing the numerical calculations, length was non-dimensionalized with respect to the characteristic radius of the $+\omega_o$ patch, $r_c = \sqrt{A_+/\pi}$, and the time unit was defined by $1/\omega_o$. After preforming such scalings we find the problem has only two free parameters, these are the distance between patches and the strength of the shear. Steady solutions were computed for a wide range of L/r_c and ω_∞/ω_o. The separations distance L/r_c between the patches was fixed at either $5, 10$, or 15 while solutions were continued in the relative strength of the background vorticity ω_∞/ω_o. Recall that ω_o and ω_∞ are taken to be of the same sign so that the fluid elements in the $+\omega_o$ patch rotate with the background shear, but the fluid in the $-\omega_o$ patch rotates against the shear.

The steady solutions computed correspond to patches with nearly elliptical shapes symmetric about the x-axis; as an example a typical solution is plotted in Figure 4.3, in this case for $L/r_c = 5$ and $\omega_\infty/\omega_o = 0.135$. Generally, such solutions can be sufficiently described by the orientation angle and aspect ratio of the patches for a given separation. All computed $-\omega_o$ patches had major axes parallel to the y-axis, and in general the $+\omega_o$ patches were oriented with their major axis on the x-axis. In terms of the coefficients which describe the patch shapes, we define the generalized aspect ratios,

$$\lambda_+ = \frac{1 - a_{1,+}}{1 + a_{1,+}} \tag{4.81}$$

$$\lambda_- = \frac{1 - a_{1,-}}{1 + a_{1,-}} \tag{4.82}$$

where λ_+ corresponds to the $+\omega_o$ patch and λ_- gives the ratio for the $-\omega_o$ patch. A

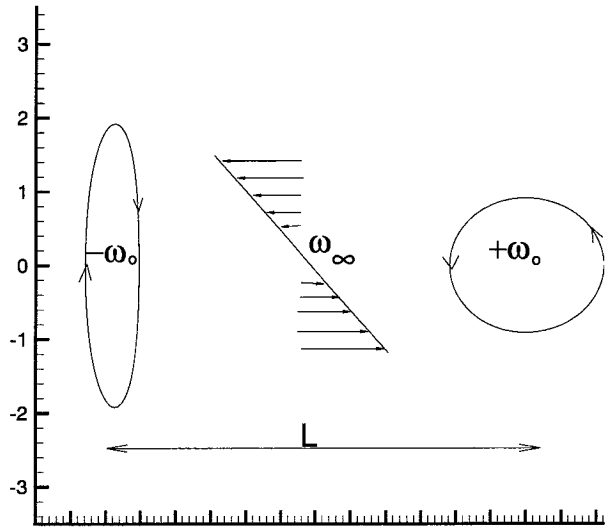

Figure 4.3: The boundaries of steady patches whose centroids are separated by a distance $L/r_c = 5$ with background shear $\omega_\infty/\omega_o = 0.135$. The patches have aspect ratios $\lambda_+ = 1.20422$ and $\lambda_- = 4.87017$.

series of plots, Figures 4.4, 4.5, and 4.6, is presented which summarize the computed solutions. As the separation distance increases, the maximum value of ω_∞/ω_o for which solutions are found tends to $(\sqrt{2}-1)/2$. This is not a surprise as beyond this value there is no analytic solution representing an isolated stationary elliptic patch of vorticity $-\omega_o$ embedded in unbounded linear shear with vorticity ω_∞. It should be noted that for very small background vorticities, the aspect ratio of the $+\omega_o$ patch decreases to one and then increases as the patch changes from being oriented with major axis parallel to the x-axis to having the major axis aligned with the y-axis as the $+\omega_o$ patch becomes the image of the $-\omega_o$ patch in the case of no shear. This feature is most visible in Figure 4.4(b) for $L/r_c = 5$. The plots indicate two solution branches which meet at a point that appears as a fold. Since the radius of convergence of induced velocities is closely related to the aspect ratio of a given patch, steady solutions were not calculated for $\lambda_- > L/r_c$. For such values one finds the velocity induced by the $-\omega_o$ patch ceases to converge on the boundary of the $+\omega_o$ patch. One could calculate solutions with $\lambda_- > L/r_c$ by use of the integral representation

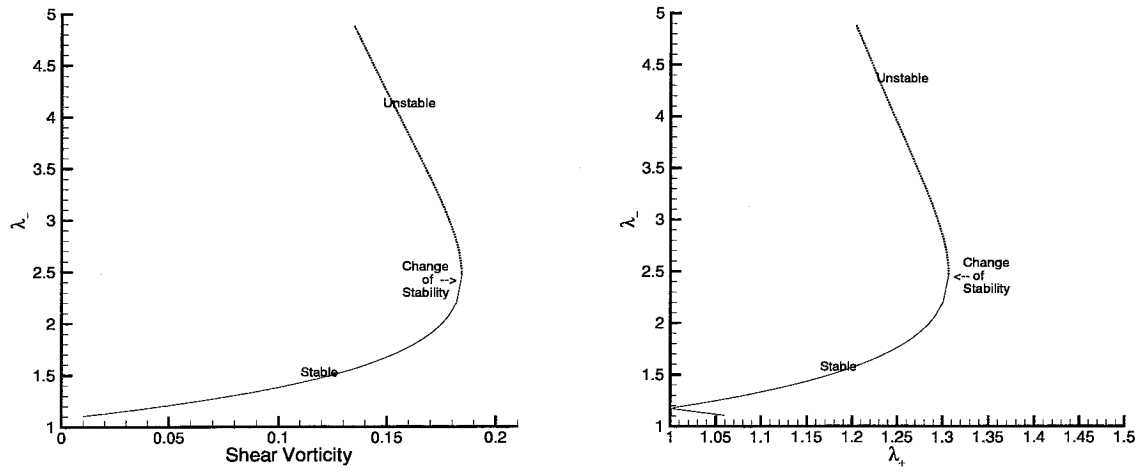

(a) λ_- vs ω_∞/ω_o (b) λ_+ vs λ_-

Figure 4.4: The aspect ratios of the steady patches for $L/r_c = 5$.

of the induced flow rather than the summation we employed, but much additional computation time would be required; as this appears to be an unstable branch such calculations were not performed.

Stability analysis indicates that the solution with the more elongated $-\omega_o$ patch, corresponding to the upper branch, is unstable. The lower branch with the more circular $-\omega_o$ patch is found to be stable to perturbations which do not affect the area or displace the centroid. A comparison of computed eigenvalues with the growth rates predicted by the dispersion relation for a single elliptic patch in unbounded flow, restated here for convenience

$$\left(\frac{\mu}{\omega}\right)^2 = -\frac{1}{4}\left\{\left(\frac{2m\lambda}{\lambda^2+1} - 1 + \frac{\omega_\infty}{\omega}\right)^2 - \left(1 - \frac{\omega_\infty}{\omega}\right)^2 \left(\frac{\lambda-1}{\lambda+1}\right)^{2m}\right\}, \tag{4.83}$$

suggests that the perturbations may be interpreted in terms of unrelated oscillation on the boundaries of the individual patches. To investigate the idea that a given eigenmode primarily affects the shape of one patch we indroduce a measure of the coupling between the shape perturbations. Recall that the perturbation to the patch

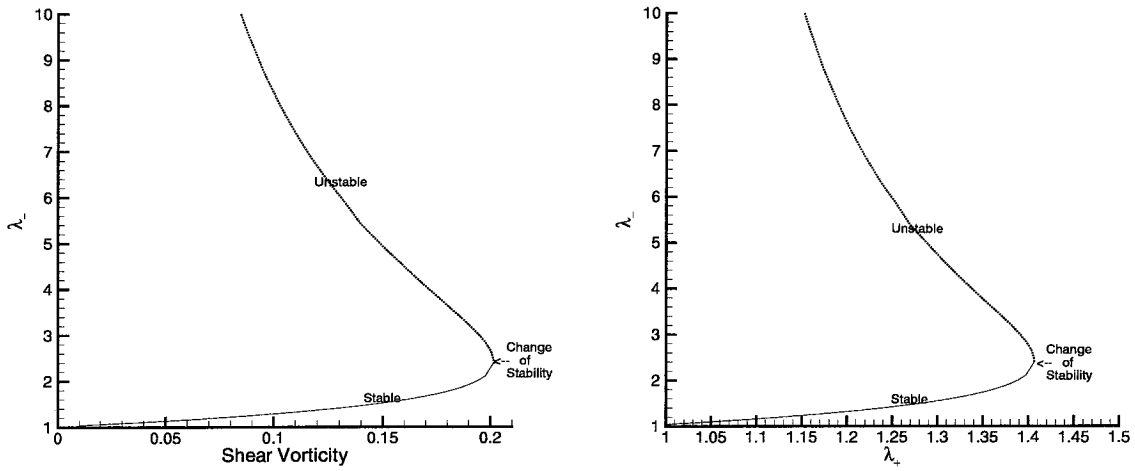

(a) λ_- vs ω_∞/ω_o (b) λ_+ vs λ_-

Figure 4.5: The aspect ratios of the steady patches for $L/r_c = 10$.

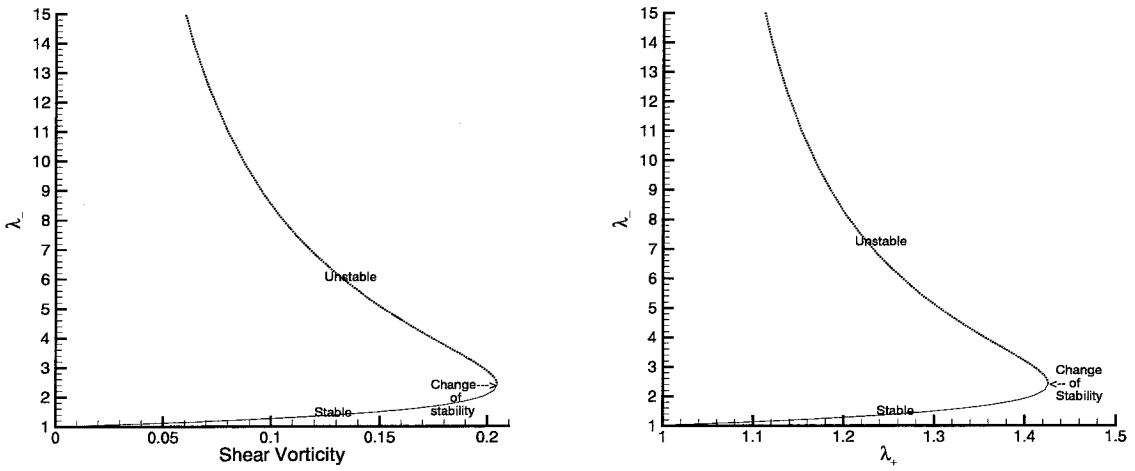

(a) λ_+ vs ω_∞/ω_o (b) λ_- vs λ_+

Figure 4.6: The aspect ratios of the steady patches for $L/r_c = 15$.

L/r_c = 5, λ_+ = 1.23481, λ_- = 4.23650		L/r_c = 10, λ_+ = 1.29014, λ_- = 4.93457		L/r_c = 15, λ_+ = 1.30158, λ_- = 5.07538	
σ/ω_o	c_{pl}	σ/ω_o	c_{pl}	σ/ω_o	c_{pl}
± 0.1764789	$1.8\ 10^{-2}$	± 0.1711631	$2.3\ 10^{-3}$	± 0.173240	$9.2\ 10^{-5}$
$i0.3151811$	$2.8\ 10^{-3}$	± 0.1665352	$5.1\ 10^{-4}$	± 0.169222	$7.1\ 10^{-4}$
$-i0.3151811$	$7.4\ 10^{-5}$	$i0.1729736$	$1.2\ 10^{-4}$	$i0.1428217$	$2.3\ 10^{-5}$
$i0.5483986$	$2.5\ 10^{-2}$	$-i0.1729736$	$5.9\ 10^{-6}$	$-i0.1428217$	$1.9\ 10^{-6}$
$-i0.5483986$	$4.0\ 10^{-4}$	$i0.3935393$	$8.1\ 10^{-6}$	$i0.3657090$	$6.1\ 10^{-7}$
$i0.5531450$	$1.8\ 10^{2}$	$-i0.3935393$	$6.5\ 10^{-7}$	$-i0.3657090$	$7.6\ 10^{-8}$
$-i0.5531450$	2.6	$i0.5433638$	$6.9\ 10^{3}$	$i0.5411926$	$2.4\ 10^{4}$
$i0.7752003$	$2.7\ 10^{4}$	$-i0.5433638$	$1.0\ 10^{2}$	$-i0.5411926$	$3.5\ 10^{3}$

Table 4.1: The first eight eigenvalues and corresponding c_{pl} solutions on the unstable branch at three different speration distances L/r_c with $\omega_\infty/\omega_o = 0.15$. Real growth rates indicate instability

shapes are defined as

$$z'_{\pm} = R'_{\pm}(t)\,\zeta\left\{1+\sum_{j=1}^{N}\frac{a_{j,\pm}}{\zeta^j}\right\} + R_{\pm}\zeta\sum_{j=1}^{N}\frac{a'_{j,\pm}(t)}{\zeta^j}. \tag{4.84}$$

We define the coupling ratio c_{pl} by

$$c_{pl}^2 = \frac{\left|R'_+\right|^2\left\{1+\sum_{j=1}^{N}\left|a_{j,+}\right|^2\right\} + \left|R_+\right|^2\sum_{j=1}^{N}\left|a'_{j,+}\right|^2}{\left|R'_-\right|^2\left\{1+\sum_{j=1}^{N}\left|a_{j,-}\right|^2\right\} + \left|R_-\right|^2\sum_{j=1}^{N}\left|a'_{j,-}\right|^2}; \tag{4.85}$$

for a given eigenmode c_{pl} compares the size of the perturbation to each patch. Very large c_{pl} indicates the eigenmode is relatively isolated to the $+\omega_o$ patch and very small c_{pl} corresponds to eigenmodes which affects mainly the $-\omega_o$ patch. In Table 4.1 we present the first eight eigenvalues and the corresponding c_{pl} for steady solution with three different separations; such calculations show the eigenmodes affect primarily a single patch. It is interesting to note that while eigenvalues come in $\pm$ pairs, the eigenfunctions related to an imaginary eigenvalue and its conjugate have different forms as indicated by different values of coupling measure.

Rather than present copious tables and plots of eigenvalues, we remark that the

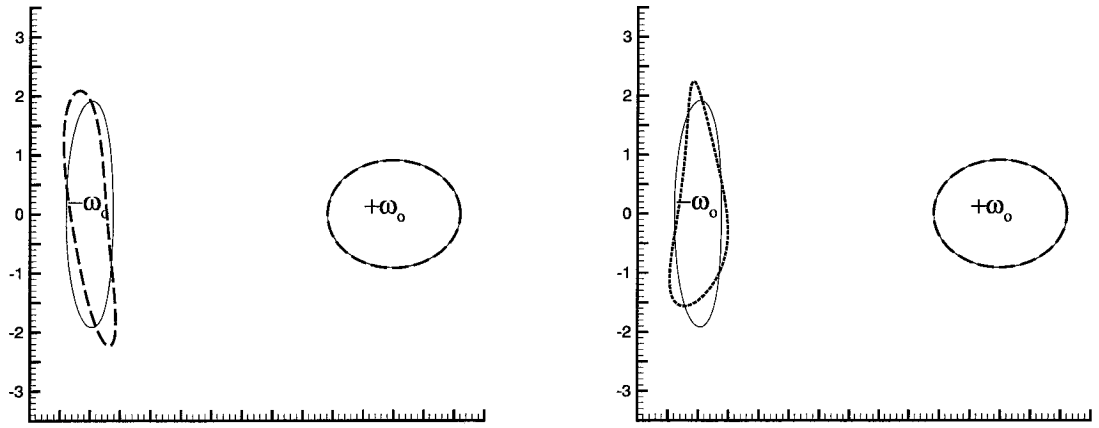

(a) $\sigma/\omega_o = 0.17181$ (b) $\sigma/\omega_o = 0.15205$

Figure 4.7: The unstable eigenfunctions for a solution on the upper branch with $L/r_c = 5$ and $\omega_\infty/\omega_o = 0.135$ The solid lines represent the steady solution and the dark dashed lines give the steady solution plus 0.2 times the eigenmode. The perturbed $+\omega_o$ patch is indistinguishable from the steady solution.

analytic dispersion relation accurately reproduced the numerically computed growth rates for perturbations to the calculated steady solutions. As an example Table 4.2 contains the computed eigenvalues for a specific steady numerical solution and the growth rates calculated from the aspect ratios by expression (4.83). For an explanation of the excellent agreement, recall that relative to a patch centroid, the velocity induced by a patch has the form

$$u - iv = \sum_{j=1} g_j / z^j \tag{4.86}$$

where g_1 and g_2 are proportional to the patch area and centroid respectively. We see that modal perturbations to a patch boundary induce velocities that must decay as $O(1/z^3)$ which implies that the boundary perturbations are relatively uncoupled. To further investigate the nature of the eigenfunctions, the unsteady modes are ploted in addition to the steady solution, see Figure 4.7. Here we have used the steady

Computed Eigenvalues	μ/ω_o for $\lambda = 1.40628$	μ/ω_o for $\lambda = 2.38878$
$\pm i0.04807$	$\pm i0.54516$	$\pm i0.04791$
$\pm i0.46610$	$\pm i1.01756$	$\pm i0.46606$
$\pm i0.54517$	$\pm i1.48985$	$\pm i0.82392$
$\pm i0.82396$	$\pm i1.96200$	$\pm i1.18027$
$\pm i1.01757$		
$\pm i1.18033$		
$\pm i1.48985$		

Table 4.2: The first seven eigenvalues compared with the $m = 2, 3, 4, 5$ modes of isolated patches with the same aspect ratios as the steady solution. The steady solution is given by $\lambda_+ = 1.40628$, $\lambda_- = 2.38878$, $L/r_c = 10$, and $\omega_\infty/\omega_o = 0.20143$.

solution already displayed in Figure 4.3; it has two unstable eigenvalues $\sigma/\omega_o \simeq 0.15205, 0.17181$. The dominant eigenfunction is shown Figure 4.7 (a); it appears as an elliptical perturbation elongating and tilting the $-\omega_o$ patch and its corresponding coupling factor is $c_{pl} = 1.9\ 10^{-2}$. The perturbation in Figure 4.7 (b) has eigenvalue $\sigma/\omega_o \simeq 0.15205$ and $c_{pl} = 8.2\ 10^{-3}$, we see that is corresponds to a mode number $m = 3$ disturbance to the $-\omega_o$ patch.

At the fold point in our solution curves, Figures 4.4, 4.5, and 4.6, the stable and unstable branches meet. At this point the two computed eigenvalues related to an elliptical ($m = 2$) perturbation to the $-\omega_o$ patch cross at the origin, changing from purely imaginary on the lower branch to purely real on the upper branch. At points along the upper branch other modes also become unstable as the $\pm$ imaginary eigenvalue pairs pass through the origin and become real eigenvalue pair. These eigenvalues correspond to higher ($m > 2$) modal perturbations to the $-\omega_o$ patch. Such points along the solution curve indicate bifurcations to patch shapes which are not primarily elliptical, but since such solutions would necessarily still be unstable to the $m = 2$ mode, they were not studied.

4.4 The elliptical patch model

Motivated by the fact that our results described elliptically shaped vortex patches, we now produce a simple low dimensional model for the interaction of the counter-rotating vortex pair in shear based on the equations which govern a single elliptical patch in unbounded linear flow.

We begin by deriving the equations which approximately describe the evolution of a group of elliptical patches of different constant vorticities and areas embedded in linear shear. In doing so we assume that each patch *sees* a strain field corresponding to an approximation of the induced flow from the other patches as well as the background shear. In Appendix D we present a Hamiltonian for this system independently given by Ngan, Meacham and Morrision [26]. Our specific case of two counter-rotating vortex patches of equal strength is then studied. The predictions from this simple model compare excellently with the numerically computed steady solutions of the last section. Augmenting this elliptical patch model with the dispersion relation for a single elliptical patch allows us to calculate very good approximate stability results.

4.4.1 The interaction of elliptical patches in shear

In this subsection we use an elliptical vortex approximation to produce a series of coupled equations which describe the interaction of a constellation of elliptic vortex patches in shear. In particular we assume that the separation between patches is large enough that on the boundary of a given patch, the induced velocities from all the other patches can be adequately approximated by a linear strain. The velocity of the center of a patch is given by averaging the external velocity through the patch. This implies the well known result that if z_c gives the centroid of an elliptical patch in a background flow defined by the complex potential W, then

$$\frac{d}{dt}\left(\bar{z}_c\right) = \left(\frac{dW}{dz}\right)_{z_c} + \frac{1}{8\pi}\left|A_c\right|\left(\lambda_c - 1/\lambda_c\right)e^{i2\theta_c}\left(\frac{d^3W}{dz^3}\right)_{z_c} \tag{4.87}$$

where $|A_c|$ is the patch area, λ_c gives the aspect ratio and θ_c is the angle measured counter clockwise from the horizontal to the major axis.

To formulate the equations of motion for a system of elliptically shaped patches interacting in an external shear, we examine the action of a given patch in the flow induced by all the other patches as well as the background. In the neighborhood of a vortex patch with centroid z_i, the velocity field resulting from the other elliptically shaped patches with centroids $z_k = X_k + iY_k$, as well as a constant shear and translation, is given by

$$u_E - iv_E = -iV_\infty + i\frac{\omega_\infty}{2}(z - \bar{z}) + \sum_{k \neq i} \frac{-i(\omega_k - \omega_\infty)|A_k|}{\pi} F_{i,k} \tag{4.88}$$

with

$$F_{i,k} = \left(z - z_i + z_{i,k} + \sqrt{(z - z_i + z_{i,k})^2 - |A_k|(\lambda_k - 1/\lambda_k)\, e^{i2\theta_k}/\pi} \right)^{-1}. \tag{4.89}$$

The quantity $z_{i,k} = z_i - z_k = R_{i,k} \exp(i\theta_{i,k})$ represents the vector between the centroid of our vortex patch and another patch in the ensemble. Assuming the characteristic radius of each patch is small compared to the separation distance between patches we may make the local approximation

$$F_{i,k} \simeq \frac{1}{2z_{i,k}} + \frac{1}{8}\frac{|A_k|}{z_{i,k}^3 \pi} e^{i2\theta_k}(\lambda_k - 1/\lambda_k) - \frac{1}{2z_{i,k}^2}(z - z_i) + \frac{1}{2z_{i,k}^3}(z - z_i)^2. \tag{4.90}$$

The equations describing the motion of the centroid of our patch may be obtained by identifying $u_E - iv_E$ with dW/dz in equation (4.87);

$$\begin{aligned} \frac{d}{dt}(\bar{z}_i) &= -iV_\infty + i\frac{\omega_\infty}{2}(z_i - \bar{z}_i) - i\sum_{k \neq i}(\omega_k - \omega_\infty)\frac{|A_k|}{z_{i,k}}\frac{1}{2\pi} \\ &\quad -i\sum_{k \neq i}\frac{(\omega_k - \omega_\infty)}{8\pi^2}\frac{|A_k|}{z_{i,k}^3}\left(|A_k|\, e^{i2\theta_k}(\lambda_k - 1/\lambda_k) + |A_i|(\lambda_i - 1/\lambda_i)\, e^{i2\theta_i}\right). \end{aligned} \tag{4.91}$$

We assume that the evolution of the boundary of the patch is determined by the induced flow from the other patches as approximated by a local strain. The strain

field contributed by all other patches then has the approximate form

$$u - iv \simeq (z - z_i)\, i \sum_{k \neq i} \frac{(\omega_k - \omega_\infty)\,|A_k|}{2\pi R_{i,k}^2} e^{-i2\theta_{i,k}} = \sigma e^{i\phi}\,(z - z_i)\,. \tag{4.92}$$

Inserting this strain into the equation governing the development of the aspect ratio of a single patch (4.37) gives

$$\frac{d}{dt}\lambda_i = \lambda_i \sum_{k \neq i} \left\{ \frac{(\omega_k - \omega_\infty)\,|A_k|}{\pi R_{i,k}^2} \sin 2\,(\theta_{i,k} - \theta_i) \right\} - \lambda_i \omega_\infty \sin 2\theta_i. \tag{4.93}$$

Likewise this local strain implies from (4.38) that the orientation angle will develop as

$$\begin{aligned} \frac{d}{dt}\theta_i \;=\; & \frac{(\omega_i - \omega_\infty)\,\lambda_i}{(1+\lambda_i)^2} + \frac{\omega_\infty}{2}\left(1 - \frac{\lambda_i^2 + 1}{\lambda_i^2 - 1}\cos 2\theta_i\right) \\ & + \frac{1+\lambda_i^2}{1-\lambda_i^2} \sum_{j \neq i} \left[\frac{|A_j|\,(\omega_j - \omega_\infty)}{2\pi R_{i,j}^2} \cos 2\,(\theta_i - \theta_{i,j}) \right]. \end{aligned} \tag{4.94}$$

Taken together, equations (4.91) (4.93) and (4.94) define a model for the interaction of a system of elliptical vortex patches interacting via their induced flow in a strain field.

4.4.2 Two counter-rotating patches in shear

Turning our attention to the problem of two counter-rotating vortex patches in shear, we seek solutions to our approximate equations which are steady in a frame of reference moving with the patches. Recall that the patches are taken to each have vorticity $\pm\omega_o$ and are situated with the centroids aligned with the shear. In particular we assume that in our co-ordinate system the background flow representing both shear and vortex induced translation is of the form

$$u - iv = -iV_\infty + i\frac{\omega_\infty}{2}\,(z - \bar{z})\,. \tag{4.95}$$

Without loss of generality we take $+\omega_o$ and ω_∞ to be of the same sign. In this configurations we refer to the $+\omega_o$ patch as rotating with the shear and the $-\omega_o$ patch as rotating against the shear. We seek steady solutions for which the centroid of the $+\omega_o$ patch z_+ is found at $L/2$ and the centroid of the $-\omega_o$ patch is given by $z_- = -L/2$. Recall also, to insure that the patches have equal strength relative to the background vorticity, the area A_- of the $-\omega_o$ patch is related to the $+\omega_o$ patch area A_+ by

$$A_+ (\omega_o - \omega_\infty) = A_- (\omega_o + \omega_\infty) . \tag{4.96}$$

The magnitude of additional vorticity due to a patch defines $\Gamma = (\omega_o - \omega_\infty) A_+$. Under the elliptical patch approximation, time independent patch configurations are the steady solutions of the evolution equations: (4.91), (4.93), and (4.94).

From equation (4.91), the vertical component of the velocity of the vortex pair

$$\begin{aligned} \frac{dy_+}{dt} &= \frac{dy_-}{dt} \\ &= V_\infty - \frac{1}{2\pi}\frac{\Gamma}{L} - \frac{1}{8\pi^2}\frac{\Gamma}{L^3}\left(A_- \frac{\lambda_-^2 - 1}{\lambda_-} \cos 2\theta_- + A_+ \frac{\lambda_+^2 - 1}{\lambda_+} \cos 2\theta_+ \right) \end{aligned} \tag{4.97}$$

in conjunction with the stationary requirement $\dot{y}_\pm = 0$ produces the translational velocity V_∞ which balances the self-induced downward motion of the vortex pair. Notice that the leading term gives the velocity of a point vortex pair, while the following terms are geometric corrections related to the finite areas of the patches. The horizontal velocity of the vortex pair may be computed from equation (4.91) as

$$\begin{aligned} \frac{dx_+}{dt} + \omega_\infty y_+ &= \frac{dx_-}{dt} + \omega_\infty y_- \\ &= \frac{-\Gamma}{8\pi^2 L^3}\left(A_- \frac{\lambda_-^2 - 1}{\lambda_-} \sin 2\theta_- + A_+ \frac{\lambda_+^2 - 1}{\lambda_+} \sin 2\theta_+ \right) . \end{aligned} \tag{4.98}$$

In our configuration with the centroids aligned on the same horizontal, the elliptical patches develope independently; according to equations (4.93) and (4.94) the patch

which rotates with the shear evolves according to

$$\frac{d\lambda_+}{dt} = \lambda_+ \left(\frac{\Gamma}{\pi L^2} - \omega_\infty \right) \sin 2\theta_+ \tag{4.99}$$

$$\frac{d\theta_+}{dt} = \frac{\Gamma \lambda_+}{A_+ (1+\lambda_+)^2} + \frac{\omega_\infty}{2} + \frac{1}{2} \frac{1+\lambda_+^2}{1-\lambda_+^2} \left(\omega_\infty - \frac{\Gamma}{\pi L^2} \right) \cos 2\theta_+ \tag{4.100}$$

while the elliptical patch which rotates against the shear obeys

$$\frac{d\lambda_-}{dt} = -\lambda_- \left(\frac{\Gamma}{\pi L^2} + \omega_\infty \right) \sin 2\theta_- \tag{4.101}$$

$$\frac{d\theta_-}{dt} = \frac{-\Gamma \lambda_-}{A_- (1+\lambda_-)^2} + \frac{\omega_\infty}{2} + \frac{1}{2} \frac{1+\lambda_-^2}{1-\lambda_-^2} \left(\omega_\infty + \frac{\Gamma}{\pi L^2} \right) \cos 2\theta_- . \tag{4.102}$$

From the equations (4.99) and (4.101), we observe that two possible orientations for each patch, $\theta = 0$ or $\pi/2$, insure steady aspect ratios. By means of formula (4.98), these orientation angles also imply $\dot{x}_\pm = 0$. By definition, only aspect ratios greater than one will be considered admissible solutions. We assume that $\theta_+ = 0$ and $\theta_- = \pi/2$; if an aspect ratio $\lambda < 1$ is calculated, it will be interpreted as an aspect ratio of $1/\lambda$ with an orientation increased by $\pi/2$.

Re-writing the steady orientation angle expressions $\dot{\theta}_+ = \dot{\theta}_- = 0$, gives the following algebraic equations for the aspect ratios

$$\frac{\omega_o}{\omega_\infty} = \frac{1 + (1 - 2\,(L/r_c)^2)\lambda_+ + (1 + 2\,(L/r_c)^2)\lambda_+^2 + \lambda_+^3}{\left(1 + 2\,(L/r_c)^2 + \lambda_+\right)\left(1 + \lambda_+^2\right)} \tag{4.103}$$

$$\frac{-\omega_o}{\omega_\infty} = \frac{1 + \left(1 + 2\,(L/r_c)^2\right)\lambda_- + \left(1 - 2\,(L/r_c)^2\right)\lambda_-^2 + \lambda_-^3}{\left(\left(2\,(L/r_c)^2 - 1\right)\lambda_- - 1\right)\left(1 + \lambda_-^2\right)} \tag{4.104}$$

where $r_c = \sqrt{A_+/\pi}$. Over the range of vortex separations and aspect ratios we studied numerically, the curves equations (4.103) and (4.104) define are visually indistinguishable from the computed solution curves displayed in Figures 4.4, 4.5 and 4.6.

As an example of the accuracy of the analytic model, we use the aspect ratios it produces and the analytic dispersion relation for a single patch in unbounded flow, equation (4.83), to predict the location of the fold, where the $m = 2$ eigenvalue

		m=2		m=3	
		analytic	numeric	analytic	numeric
L=15	ω_∞/ω_o	0.204608	0.204609	0.175181	0.175174
	λ_+	1.42615	1.42618	1.35783	1.35786
	λ_-	2.41922	2.41942	3.98510	3.95890
L=10	ω_∞/ω_o	0.201464	0.201472	0.172075	0.172031
	λ_+	1.40623	1.40638	1.33870	1.33897
	λ_-	2.42554	2.42558	3.96752	3.96952
L=5	ω_∞/ω_o	0.184094	0.184357	0.154927	0.154497
	λ_+	1.30336	1.30635	1.23957	1.24409
	λ_-	2.46087	2.46465	4.01799	4.04888

Table 4.3: Locations in solution space of the fold, $m = 2$, and first bifurcation, $m = 3$ analytically predicted and numerically calculated.

becomes unstable, and the location on the upper branch where the next eigenvalue, $m = 3$, becomes unstable. Table 4.3 shows that the analytic predictions agree very well with the numerically calculated values, indicating the accuracy of the elliptical vortex model. It is quite remarkable that the elliptic vortex patch model augmented with Moore and Saffman's dispersion relation for a single patch can effectively replace much more complicated numerical procedures.

4.4.3 The non-linear evolution of the elliptic model

In this subsection we make some observations about the nonlinear stability of the elliptic patch model defined by equations (4.96)-(4.102) which govern the location, orientation, and aspect ratio of each patch. We show that certain initial conditions in the elliptical patch model evolve in such a way that the aspect ration of the $-\omega_o$ patch tends to infinity while the $+\omega_o$ patch maintains compact form. In such a case the shear causes the destruction of the $-\omega_o$ patch.

As the patches evolve, the patch centroids may not follow a simple parabolic path since the aspect ratios $\lambda(t)_\pm$ and the patch orientations $\theta(t)_\pm$ are involved in calculating the location of the centroids of the patches via equations (4.97) and (4.98). In turn the aspect ratios and orientations depend on the relative locations of the patches. For certain initial conditions the relative locations of the patches is constant.

The equations for the patch centroids imply that if the patches are initially separated by a distance L and are horizontally aligned, the separation distance will be constant and the patches will remain horizontally aligned; mathematically if $x(0)_+ - x(0)_- = L$ and $y(0)_+ - y(0)_- = 0$ then $x(t)_+ - x(t)_- = L$ and $y(t)_+ - y(t)_- = 0$. We shall assume our patches are initially thus aligned.

As we have shown the separation distances between patches is constant for our patches; an examination of equations (4.99) - (4.102) shows that the geometry of the patches evolve separately. In Appendix D we constructed from consideration of the excess energy a Hamiltonian for a constellations of interacting elliptically shaped patches. For our system of two aligned patches the Hamiltonian reduces to the sum of two conserved quantities, H_+ and H_-; each defines the evolution of the geometry of a patch. For the $+\omega_o$ patch, which has the same signed vorticity as the shear,

$$H_+ \frac{4\pi}{\Gamma^2} = -\frac{1}{2}\log\left(\frac{(\lambda_+ + 1)^2}{\lambda_+}\right) - \frac{1}{2}\frac{\omega_\infty}{\omega_o}\frac{1+\lambda_+^2}{2\lambda_+} - \frac{1}{4}\left(\frac{\lambda_+^2 - 1}{2\lambda_+}\right)\left(\frac{\omega_\infty}{\omega_o} - \frac{A_+}{\pi L^2}\right)\cos 2\theta_+ \tag{4.105}$$

defines the conserved quantity H_+ while

$$H_- \frac{4\pi}{\Gamma^2} = -\frac{1}{2}\log\left(\frac{(\lambda_- + 1)^2}{\lambda_-}\right) + \frac{1}{2}\frac{\omega_\infty}{\omega_o}\frac{1+\lambda_-^2}{2\lambda_-} + \frac{1}{4}\left(\frac{\lambda_-^2 - 1}{2\lambda_-}\right)\left(\frac{\omega_\infty}{\omega_o} + \frac{A_-}{\pi L^2}\right)\cos 2\theta_- \tag{4.106}$$

defines the quantity H_- which is conserved for the patch whose vorticity is signed against the shear. As a check, direct differentiation and comparison with the equations which govern the evolution of the elliptical patches shows

$$\frac{\partial H_\pm}{\partial \lambda_\pm} = \pm\frac{|A_\pm|\,\Gamma}{8\pi}\frac{\left(1-\lambda_\pm^2\right)}{\lambda_\pm}\frac{d\theta_\pm}{dt} \tag{4.107}$$

$$\frac{\partial H_\pm}{\partial \theta_\pm} = \mp\frac{|A_\pm|\,\Gamma}{8\pi}\frac{\left(1-\lambda_\pm^2\right)}{\lambda_\pm}\frac{d\lambda_\pm}{dt} \tag{4.108}$$

which implies $H_\pm$ are conserved.

In Figure 4.8 we choose $L/r_c = 10$ and $\omega_\infty/\omega_o = 0.15$ and plot the constant contours of the Hamiltonians in λ, θ space for both patches. Due to the symmetry

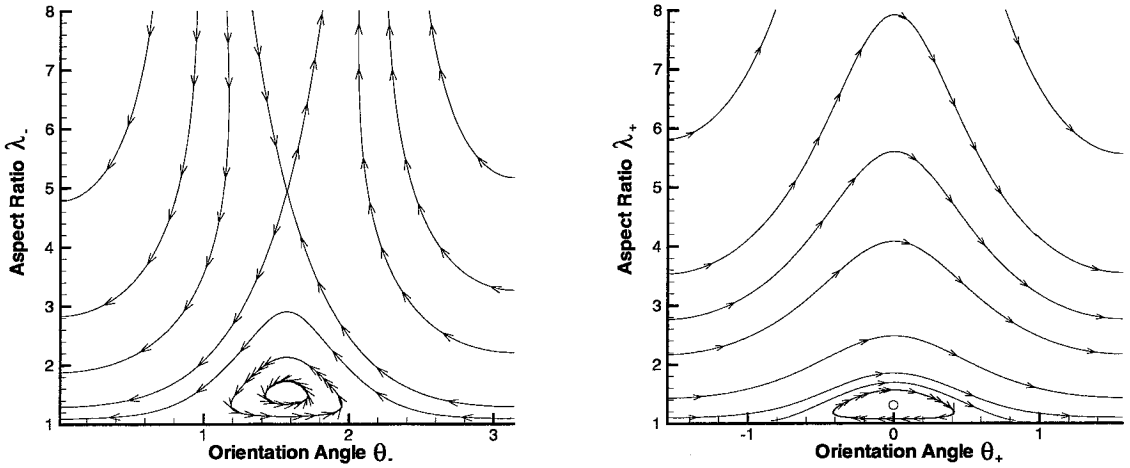

(a) The $-\omega_o$ patch: θ_- vs λ_-

(b) The $+\omega_o$ patch: θ_+ vs λ_+

Figure 4.8: The trajectories of non-linear patch evolution for $L/r_c = 10$ and $\omega_\infty/\omega_o = 0.15$

of an ellipse, the Hamiltonians are periodic in θ with period π. Notice from Figure 4.8 (b) that there is one steady orientation and aspect ratio for the patch whose fluid elements rotate with the shear, and this patch is stable in sense that its aspect ratio remains bounded. But the patch whose fluid elements rotate against the shear has two steady points in Figure 4.8 (a), a nonlinear center and saddle. Since the geometry of each patch evolves independently with for our aligned system, we may predict the evolution of any initial orientation and aspect ratio. For instance, by combining the center for the $+\omega_o$ patch with either the center or saddle for the $-\omega_o$ patch, we can create a steady solution on the stable or unstable branches which we first identified numerically. Notice that some small perturbations from the saddle point lead to an unbounded aspect ratio as the $-\omega_o$ patch is pulled apart by the shear, yet at the same time the $+\omega_o$ patch remains compact.

Part II

Wave generation

Introduction

A possible mechanism for the generation of water waves arrises from the instability of an initially planar free surface in the presence of a parallel, sheared, inviscid flow. In such an model the free surface represents an air-water interface and the parallel flow may be chosen to describe wind blowing across the water, a drift layer in the water or both. In the simplest models the steady parallel flow is described by a piecewise-linear function; such a profile is referred to as a "stick profile".

Only two-dimensional motion is considered as for every unstable three-dimensional disturbance there is a corresponding two-dimensional disturbance with larger growth rate; this follows from the inviscid form of Squire's theorem for coupled free-surface flows. Perturbation analysis is conducted by aligning the free surface with the x axis and examining the response to two-dimensional perturbations proportional to $e^{i\kappa(x-ct)}$, where κ is a the wavenumber and c is the wavespeed. Requiring that the air-water interface be a material line and imposing continuity of force leads to an eigenvalue problem defining the dispersion relation $c(\kappa)$. For general profiles perturbation and wavespeed may be found by simple numerical techniques. Waves with real wavespeeds are said to be stable.

Howard's semicircle theorem is a powerful result in the analysis of the unstable wavespeeds. Assuming that $U_{\max}$ and $U_{\min}$ are the maximum and minimum velocities of the steady parallel flow, the semicircle theorem says that wavespeeds c with positive imaginary part lie in the semicircle in the upper-half c-plane with origin $\frac{1}{2}(U_{\min}+U_{\max})$ and radius $\frac{1}{2}(U_{\max}-U_{\min})$. Originally a result for inviscid channel flow, the theorem was extended to a flow with a free surface by Yih [45] and further extended to coupled free-surfaces flows by Morland and Saffman [23]. A proof of this theorem with the addition of surface tension at the free surface interface can be found in Appendix E.

In the absence of surface tension, Morland and Saffman [23] investigated the linear stability analysis of inviscid parallel flow of air over stagnant water. They used several smooth profiles and made comparisons with results predicted by the critical

layer theory of Miles [16]. Miles' approximate formula was found to overestimate the growth rate by a factor of two.

A drift layer in the water is a current with shear ostensibly due to the drag of wind over the water (of course it could be created by running a stream over the surface). The drift layer instability was originally investigated by Stern and Adam [35] and Voronovich *et al.* [41] who employed a piecewise-linear velocity profile in the water and ignored the surface tension and the dynamics of the wind. Morland, Saffman and Yuen [24] extended this model by including surface tension and using a variety of smooth velocity profiles. In all cases it was found that the fluid surface velocity must exceed the minimum wavespeed of stagnant fluid for instability to occur. Unstable growth rates were found to be relatively insensitive to which smooth profile was used but significantly smaller than those associated with the stick profile.

Piecewise-linear profiles in the air and the water were used by Caponi *et al.* [2] to model wind blowing across a drift layer in water. To reduce the number of parameters in this model, they assumed a characteristic ratio of wind speed to drift layer speed and related the thickness of the drift layer to the shape of the wind profile by assuming continuity of tangential stress across the air-water interface. Analysis of the eigenvalue equation for the wavespeed c lead to the identification of two non-overlapping regions of instability related to the drift layer instability and wind driven instability.

In Chapter Five we extend this model of wind blowing across a drift layer by including surface tension and replacing the stick profiles by smooth profiles. In particular we represent the wind and drift layer by exponential profiles, the form of which allows for analytic simplifications. Working in a frame of reference where the fluid velocity at the air-water interface is zero, we classify unstable waves as right-traveling (in the range of the wind profile) or left-traveling (in the range of the drift layer). We separately investigate the behavior of these waves. In terms of layer thicknesses and windspeeds, we determine stability boundaries by an application of Howard's semicircle theorem. We directly compute unstable wavespeeds and compare with the results from the stick profile. For a given set of independent parameters (e.g. windspeed, layer thickness etc.) the wavenumbers calculated by the stick and exponential

profiles corresponding to the most unstable waves are found to be in good qualitative agreement.

Chapter 5 Infinitesimal waves in the presence of wind and drift layers

5.1 Mathematical formulation

We choose to use a right handed Cartesian coordinates system with the x-axis lying along the undisturbed interface between the water and air. The force of gravity points in the negative y direction and has modulus g. We assume that at any instant the free surface can be described as a single valued function of x, and that it is given by $y = \eta(x,t)$. The assumption that the flow in question is incompressible and two dimensional implies that the fluid velocity $\mathbf{u} = (u,v)$ and the pressure p are governed by the Euler equations and equation of continuity,

$$\mathbf{u}_t + \mathbf{u}\cdot\boldsymbol{\nabla}\mathbf{u} = -\frac{1}{\rho}\boldsymbol{\nabla}p - g\widehat{\mathbf{j}} \tag{5.1}$$

$$\boldsymbol{\nabla}\cdot\mathbf{u} = \mathbf{0}, \tag{5.2}$$

where ρ represents the density of the air or water. When necessary the indices "a" and "w" may be used to indicate air and water. The free surface develops under two requirements: the interface is a material line and force is continuous across the interface. These requirements take the form of the following two equations evaluated on the free surface $y = \eta$;

$$\eta_t + \mathbf{u}\cdot\boldsymbol{\nabla}\eta = 0 \tag{5.3}$$

$$[p]_w^a = T\frac{\eta_{xx}}{\left(\sqrt{1+\eta_x^2}\right)^3}, \tag{5.4}$$

where T is the surface tension and the notation $[p]_w^a$ represents the jump in the pressure at the interface, $p_a - p_w$.

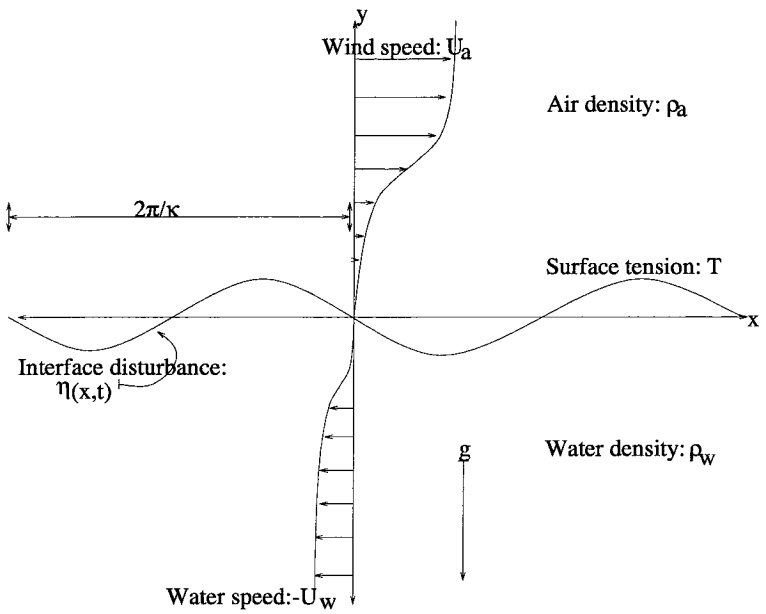

Figure 5.1: The wind-water shear flows with waves

We wish to linearize about a simple steady solution that represents wind and a drift layer in the water. Such a solution consists of a planar surface $\eta = 0$, with parallel flow $\mathbf{u} = (U(y), 0)$ and hydrostatic pressure $p = -\rho g y$. Linearized equations are obtained by assuming small time dependent perturbations to the velocity and pressure as well as the interface: $\mathbf{u} = \left(U(y) + u', v'\right), p = -\rho g y + p'$, and $y = \eta'$. Linearizing produces the equations governing the velocity perturbations,

$$u'_t + U u'_x + U_y v' = -p'_x/\rho \tag{5.5}$$

$$v'_t + U v'_x = -p'_y/\rho \tag{5.6}$$

$$u'_x + v'_y = 0, \tag{5.7}$$

and the interface conditions to be applied on the unperturbed surface $y = 0$,

$$\eta'_t + U\eta'_x - v' = 0 \tag{5.8}$$

$$\left[v'\right]_w^a = 0 \tag{5.9}$$

$$\left[p'\right]_w^a = g(\rho_a - \rho_w)\eta' + T\eta'_{xx}. \tag{5.10}$$

Furthermore, we require that the velocity perturbations tend to zero at $y \to \pm\infty$. In order to study the evolution of infinitesimal periodic waves, we seek normal mode solutions of the linearized equations. Analysis requires that

$$u' = \phi_y e^{i\kappa(x-ct)} \tag{5.11}$$

$$v' = -i\kappa\phi e^{i\kappa(x-ct)} \tag{5.12}$$

$$p' = \rho\left(\phi_y\left(c-U\right)+\phi U_y\right)e^{i\kappa(x-ct)} \tag{5.13}$$

$$\eta' = \frac{\phi\left(0\right)}{c-U\left(0\right)}e^{i\kappa(x-ct)}. \tag{5.14}$$

With out loss of generality, the wavenumber κ is taken to be positive. Elimination of the pressure terms from the linearized form of Eulers equation leads to the Rayleigh equation,

$$\phi_{yy} - \left(\kappa^2 + \frac{U_{yy}}{U-c}\right)\phi = 0. \tag{5.15}$$

This equation is to be solved in the fluids, subject to the requirement $\phi \to 0$ as $y \to \pm\infty$ and to the boundary conditions which result from the linearized interface conditions. These boundary interface conditions, given by the following equations evaluated at $y = 0$, represent a jump in the tangential velocity and continuity of normal velocity;

$$\left[\rho\phi U_y + \rho\left(c-U\right)\phi_y\right]_w^a = \frac{\phi}{c-U}\left\{g\left(\rho_a-\rho_w\right)-\kappa^2 T\right\} \tag{5.16}$$

$$\phi\left(0^+\right) = \phi\left(0^-\right). \tag{5.17}$$

The Rayleigh equation in the fluids and the boundary interface conditions together with the requirement $\phi \to 0$ as $y \to \pm\infty$ form an eigenvalue problem. For a given background flow $U\left(y\right)$ we assume that the wavenumber κ is specified so that the wavespeed c is the eigenvalue. After one has found continuous bounded solutions to the Rayleigh equation, the boundary interface condition (5.16) will define an implicit dispersion relation. A wavespeed with an imaginary part indicates that the amplitude of an infinitesimal wave of the given wave length grows or decays exponentially

while the wave travels with speed $\Re(c)$. Notice that time reversal and a reflection about the y-axis implies that complex eigenvalues come in conjugate pairs. We define perturbations with real wavespeeds c as stable.

5.2 An exponential profile for wind and drift layer

As pointed out by Miles in an appendix to Moreland and Saffman [23], the Rayleigh equation may be analytically solved in the case that the velocity profile for the parallel flow is given by simple exponentials. Representing a simple continuous wind and water profile with exponentials, we take

$$U(y) = \left\{ \begin{array}{ll} U_a\left(1 - \exp\left[-2y/\Delta_a\right]\right) & y > 0 \\ U_w\left(\exp\left[2y/\Delta_w\right] - 1\right) & y < 0 \end{array} \right\}. \tag{5.18}$$

Notice that the velocity of the water and wind is zero at the undisturbed interface, $y = 0$; the wind increases monotonically to the speed U_a at infinity, while the water velocity decreases to $-U_w$ at minus infinity. Most of the velocity profile change occurs in a thin layer above and below the interface; the lengths Δ_a, $\Delta_w > 0$ are the centroids of vorticity in the air and water and will be referred to as the thickness of the wind layer and the drift layer. In general we assume some relationship between the steady profile in the wind and in the water resulting from physical considerations. We define the nondimensional ratios $\gamma = U_w/U_a$ and $\omega = \Delta_a/\Delta_w$ as well as the ratio $s = \rho_a/\rho_w$ of the air and water densities; s has the approximate value 0.001226. For the parallel flows given (5.18), the Rayleigh equation has the form

$$\phi_{yy} - \left(\kappa^2 + \left(\frac{2}{\Delta_a}\right)^2 \frac{U_a e^{-2y/\Delta_a}}{U_a e^{-2y/\Delta_a} - (U_a - c)}\right)\phi = 0; \quad y > 0 \tag{5.19}$$

$$\phi_{yy} - \left(\kappa^2 + \left(\frac{2}{\Delta_w}\right)^2 \frac{U_w e^{2y/\Delta_w}}{U_w e^{2y/\Delta_w} - (U_w + c)}\right)\phi = 0; \quad y < 0. \tag{5.20}$$

As mentioned earlier, such equations may be solved by means of complex Hypergeometric functions $F(a, b, c, z)$. Imposing decay at $\pm\infty$ as well as continuity across the

undisturbed interface $y = 0$ produces the solution

$$\phi = e^{-\kappa|y|} \left\{ \begin{array}{ll} \frac{F(p,q,p+q+1,U_a \exp(-2y/\Delta_a)/(U_a-c))}{F(p,q,p+q+1,U_a/(U_a-c))} & y > 0 \\ \frac{F(l,m,l+m+1,U_w \exp(2y/\Delta_w)/(U_w+c))}{F(l,m,l+m+1,U_w/(U_w+c))} & y < 0 \end{array} \right\} \tag{5.21}$$

where the parameters are given by

$$p = \kappa\Delta_a/2 + \sqrt{(\kappa\Delta_a/2)^2 + 1} \tag{5.22}$$

$$l = \kappa\Delta_w/2 + \sqrt{(\kappa\Delta_w/2)^2 + 1} \tag{5.23}$$

and $q = -1/p$, $m = -1/l$. Recall that the wavenumber κ is taken to be positive. We have yet to satisfy the interface condition representing the jump in the tangential velocities at $y = 0$. In a notation we will continue to use throughout this chapter, we suppress the parameters in the Hypergeometric functions and introduce the subscripts "a" and "w" to distinguish between the solutions in the air and water. The boundary interface condition now takes the form

$$\frac{2(s-\gamma\omega)U_a}{\kappa\Delta_a c} + \frac{1}{c^2}\left(g\frac{1-s}{\kappa} + \kappa\frac{T}{\rho_w}\right) = 1 + s + \frac{2}{\kappa\Delta_a}\omega Z_2 \frac{F_w'(Z_2)}{F_w(Z_2)} + s\frac{2}{\kappa\Delta_a} Z_1 \frac{F_a'(Z_1)}{F_a(Z_1)} \tag{5.24}$$

where $Z_1 = U_a/(U_a - c)$, $Z_2 = U_w/(U_w + c)$, and the primes denote differentiation. This equation can be considered to be an implicit dispersion relation.

The exponential decay of the form $\exp(-\kappa|y|)$ found in the velocity perturbation is characteristic of interface waves and can be directly deduced from the Rayleigh equation. Recall that κ is the wavenumber of the perturbation, this exponential suggests that a wave exist on a vertical scale proportional to its wavelength. With this in mind we briefly examine the dispersion relation (5.24) in two limits of the ratio of wave length to layer thickness: very short waves and very long waves. We show that in the limit of large layer thicknesses the dispersion relation tends to the ordinary gravity-capillary dispersion relation, and in the limit of small layer thicknesses we reclaim the unstable Kelvin-Helmholtz dispersion relation.

5.2.1 The gravity-capillary limit: $\kappa\Delta_a \to \infty$

In examining the implicit dispersion relation for the large $\kappa\Delta_a$ limit in which the ratio of layer thicknesses $\omega = \Delta_a/\Delta_w$ is held constant, it is useful to first nondimensionalize with respect to the gravity-capillary wavespeed, $c_o(\kappa)$;

$$c_o^2 = \left(g\frac{(1-s)}{\kappa} + T\frac{\kappa}{\rho_w}\right)/(1+s). \tag{5.25}$$

In the absence of a background flow, i.e. $U_a = U_w = 0$, equation (5.25) defines the dispersion relation for infinitesimal perturbations; notice such perturbations are stable. For this dispersion relation we see that there exists a wave of minimum speed $U_{\min}$ with wavenumber $\kappa_{\min}$,

$$U_{\min} = \left(\frac{4Tg}{\rho_w}\right)^{1/4}\left(\frac{1-s}{(1+s)^2}\right)^{1/4} \tag{5.26}$$

$$\kappa_{\min} = \sqrt{g(1-s)\frac{\rho_w}{T}}. \tag{5.27}$$

For an air-water interface $U_{\min} \sim 23.2\ cm/s$ and $\kappa_{\min} \sim 3.6\ 1/cm$. By defining the nondimensional quantities $\widehat{c} = c/c_o$ and $\widehat{U} = U_a/c_o$, we may rewrite our dispersion relation (5.24) as

$$s - \omega\gamma + \kappa\Delta_a\frac{1+s}{2\widehat{U}}\left(\frac{1}{\widehat{c}} - \widehat{c}\right) = \frac{\widehat{c}}{\widehat{U}}\left(sZ_1\frac{F_a'(Z_1)}{F_a(Z_1)} + \omega Z_2\frac{F_w'(Z_2)}{F_w(Z_2)}\right). \tag{5.28}$$

We see that as $\kappa\Delta_a \to \infty$, the dominate term in the dispersion relation requires $1/\widehat{c} - \widehat{c} \to 0$. In other words, the dispersion relation for very short waves tends to the dispersion relation one would find in the absence of a background flow $U(y)$. This result may be anticipated since short waves don't *see* very far into the flow and in a vertical strip much smaller than the layer thicknesses and centered on the undisturbed interface, $y = 0$, the background profile is approximately zero.

5.2.2 The Kelvin-Helmholtz limit: $\kappa\Delta_a \to 0$

To investigate the behavior of the dispersion relation for wave lengths much longer than the layer thickness, we use an asymptotic expansion for the Hypergeometric function for small $\kappa\Delta_a$;

$$\frac{F'(p,q,p+q+1,Z)}{F(p,q,p+q+1,Z)} = -\frac{1}{1-Z} + \kappa\Delta_a \frac{2-Z}{2(1-Z)^2} + O(\kappa\Delta_a)^2, \tag{5.29}$$

recall that $pq = -1$ and $p = \kappa\Delta_a/2 + \sqrt{(\kappa\Delta_a/2)^2 + 1}$. Surprisingly, standard references only present expansions of the Hypergeometric function about the singular points of the defining differential equation; equation (5.29) was obtained directly from the Hypergeometric differential equation.

As $\kappa\Delta_a \to 0$ with $\omega = \Delta_a/\Delta_w$ held constant, the dominant term in the expansion of the general dispersion relation (5.24) becomes

$$\frac{1}{c}\left(g\frac{1-s}{\kappa} + T\frac{\kappa}{\rho_w}\right) = c\left(1 + s + Z_2\frac{2-Z_2}{(1-Z_2)^2} + sZ_1\frac{2-Z_1}{(1-Z_1)^2}\right), \tag{5.30}$$

where $Z_1 = U_a/(U_a - c)$ and $Z_2 = U_w/(U_w + c)$. Solving for the wavespeed c we arrive at the Kelvin-Helmholtz dispersion relation;

$$c = \frac{sU_a - U_w}{1+s} \pm \frac{1}{1+s}\sqrt{g\frac{(1-s^2)}{\kappa} + T(1+s)\frac{\kappa}{\rho_w} - s(U_a + U_w)^2}. \tag{5.31}$$

This is the dispersion relation one would compute for infinitesimal perturbations when the background velocity profile is a step function; $U(y) = (U_a + U_w)H(y) - U_w$. Notice that the Kelvin-Helmholtz dispersion relation may be unsteady for a certain range of wavenumber. We can say that in the small $\kappa\Delta_a$ limit, the transitional wind and drift layers about the interface are too small to be noticed by the relatively much longer waves; instead the waves see a step velocity profile.

5.3 Stability regions

In Appendix F we examine stability boundaries for two simple models of wind blowing across a flat free surface: an exponential wind profile over stationary water and a constant wind over a drift layer in water. In this section we assume a wind profile and a drift layer, both modeled by exponentials. We choose a frame of reference such that the velocity at the undisturbed interface is zero and study the stability boundaries associated with this flow. As we have already stated in expression (5.18), the undisturbed profile in the air and water is given by

$$U(y) = \left\{ \begin{array}{ll} U_a \left(1 - \exp\left[-2y/\Delta_a\right]\right) & y > 0 \\ U_w \left(\exp\left[2y/\Delta_w\right] - 1\right) & y < 0 \end{array} \right\}. \tag{5.32}$$

We proceed to reduce the number of parameters in this profile in the manner in which Caponi, Caponi, Saffman and Yuen [2] related stick wind profiles to stick water profiles. We assume speeds of air and water relative to the stationary undisturbed interface are related by $U_w/U_a = \gamma$ where γ is a known number; Valenzuela [40] suggest typical values of 0.044 and 0.057. Although the steady flow $\mathbf{u} = (U(y), 0)$, with $U(y)$ given by (5.32), is not an exact solution to the equations of motion when viscosity is included; the thickness of the drift layer is assumed to be related to the size of the layer in the wind by imposing continuity of tangential stress: $\rho_a \nu_a U_a/\Delta_a = \rho_w \nu_w U_w/\Delta_w$, where for water and air $\rho_a/\rho_w = s \simeq 0.001226$ and $\nu_a/\nu_w \simeq 14.94$. Choosing a typical value for the velocity ratio γ determines the layer thickness ratio $\Delta_a/\Delta_w = \omega$. For the purpose of making plot in this section, we shall proceed with $\gamma = 0.057$. Only two parameters are now required to specify the undisturbed profile: the wind velocity U_a and the wind layer thickness Δ_a.

After nondimensionalizing with respect to the minimum gravity-capillary wavespeed $U_{\min}$ and its corresponding wavenumber $\kappa_{\min}$, the dispersion relation which we earlier

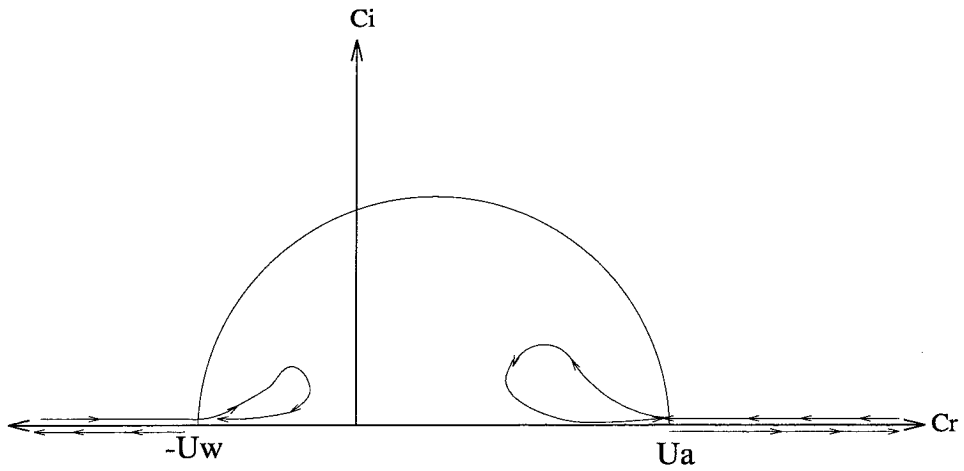

Figure 5.2: Sketch of the compex wave speed $c(\kappa)$ for wind and drift layer entering and exiting the Howard semicircle.

derived (5.24) takes the form

$$\frac{2}{kd_a}\frac{U}{C}(s-\gamma\omega)+\frac{1}{C^2}\frac{(1+s)}{2}\left(\frac{1}{k}+k\right)=1+s+\frac{2}{kd_a}\omega Z_2\frac{F_w'(Z_2)}{F_w(Z_2)}+s\frac{2}{kd_a}Z_1\frac{F_a'(Z_1)}{F_a(Z_1)} \tag{5.33}$$

where $U=U_a/U_{\min}, C=c(\kappa)/U_{\min}, d_a=\Delta_a\kappa_{\min}$, and $k=\kappa/\kappa_{\min}$. Recall that the functions denoted by F are the complex Hypergeometric functions of the second kind and represent the y dependence of the air and water eigenfunctions, as indicated in expression (5.21), and also that $Z_1=1/(1-c/U_a)$ and $Z_2=1/(1+c/U_w)$.

From the Howard semicircle theorem presented in Appendix E, we know that the real part of the complex wavespeed associated with an unstable wave will be in the range of the parallel flow: $U_a>\Re[c(\kappa)]>-U_w$, or in terms of our nondimesonalized quantities $U>\Re[C]>-\gamma U$. Unlike the profile in Appendix F, the Howard semicircle may be entered from either side, see Figure 5.2.

Depending on the value of U, the dispersion relation (5.33) can lead to right and left traveling unstable waves. Since unstable right-traveling waves have speeds in the range of the air profile, $\{0,U_a\}$, we anticipate a stability boundary near $U=1$ as the wind speed overtakes the slowest right-traveling wave. Likewise we expect the slowest left-traveling waves to become unstable near $\gamma U=1$.

We choose to examine right and left traveling waves separately. We will first

determine the stability regions for the right-traveling waves and then for left-traveling waves.

5.3.1 Right-traveling waves: in the range of the wind

To find the wavenumbers k at which the complex wavespeed for the right-traveling waves enters and exits the Howard semicircle, we substitute $C = U$ into our dispersion relation (5.33). The implicit equation for such wavenumbers takes the form

$$\frac{2}{kd_a}(s-\gamma\omega)+\frac{1}{U^2}\frac{(1+s)}{2}\left(\frac{1}{k}+k\right)=\frac{2}{kd_a}\omega\frac{\gamma}{\gamma+1}\frac{F_w'\left(\gamma/(\gamma+1)\right)}{F_w\left(\gamma/(\gamma+1)\right)}+s\sqrt{1+\left(\frac{2}{kd_a}\right)^2}. \tag{5.34}$$

Unfortunately, we can not solve explicitly for the layer thickness as a function of wavenumber because the Hypergeometric functions depend on layer thickness in a complicated manner. Recall that $F_w(Z) = F(l, m, l+m+1, Z)$, where $l = kd_a/(2\omega) + \sqrt{(kd_a)^2/(4\omega^2)+1}$ and $ml = -1$. Instead we solve equation (5.34) for U and make contour plots in the (k, a) plane corresponding to different wind speeds; see Figure 5.3. For a given layer thickness and windspeed, we find at most two nondimensional wavenumbers k_{a1} and k_{a2} such that $C(k_{a1}) = C(k_{a2}) = U$. Those wavenumbers between k_{a1} and k_{a2} are correspond to unstable right-traveling waves.

We find that when $U < \sqrt{1+s}/(1+\gamma)$ all right traveling waves are stable. For values of wind speed U such that $1 > U > \sqrt{1+s}/(1+\gamma)$ there is a region of instability for a range of layer thicknesses beginning in the Kelvin-Helmholtz limit (layer thickness $d_a = \Delta_a \kappa_{\min} \to 0$) and extending to a finite layer thickness dependant on U. The stability boundary for a given wind velocity in this range forms an inverted u-shaped curve $d_a(k)$ with the endpoints $d_a(k_a^-) = 0$, and $d_a(k_a^+) = 0$ and with a maximum value which tends to infinity as $U \to 1$. The area beneath this curve is an unstable region. The values of $k_a^{\pm}$ may be determined directly from equation (5.34) or by solving the Kelvin-Helmholtz dispersion relation (5.31) for $c = U_a$ and

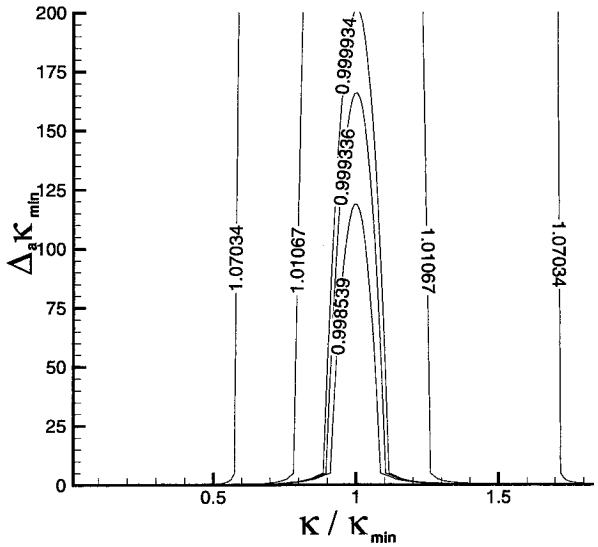

Figure 5.3: Stability boundaries $d(k)$ for right-traveling perturbations labeled by nondimensional windspeed $U = U_a/U_{min}$. These curves correspond to waves which travel at the wind speed, $c = U_a$

nondimensionalizing; one finds

$$k_a^{\pm} = \frac{U^2(1+\gamma)^2}{1+s} \pm \frac{\sqrt{U^4(1+\gamma) - (1+s)^2}}{1+s}. \tag{5.35}$$

When the wind velocity is faster than the minimum gravity-capillary wavespeed, i.e. $U > 1$, there exists unstable wavenumbers for any layer thickness. The unstable region stretches between the Kelvin-Helmholtz limit ($d_a = \Delta_a \kappa_{\min} \to 0$) and the gravity-capillary regime ($d_a = \Delta_a \kappa_{\min} \to \infty$). For $U > 1$, the stability boundary in the (k, d_a) plane appears as two curves and the area between which is unstable. The curves connects $(k_a^-, 0)$ with $\left(k_1^-, \infty\right)$ and $(k_a^+, 0)$ with $\left(k_1^+, \infty\right)$, where $k_a^{\pm}$ is given above and $k_1^{\pm}$ has the form

$$k_1^{\pm} = U^2 \pm \sqrt{U^4 - 1}. \tag{5.36}$$

By calculating the maximum of $d_a(k)$ as a function of the drift speed U, a curve can be drawn in the space of wind speed vs. layer thickness. Such a curve is shown in Figure 5.4. This curve separates the region in which any right-traveling perturbation

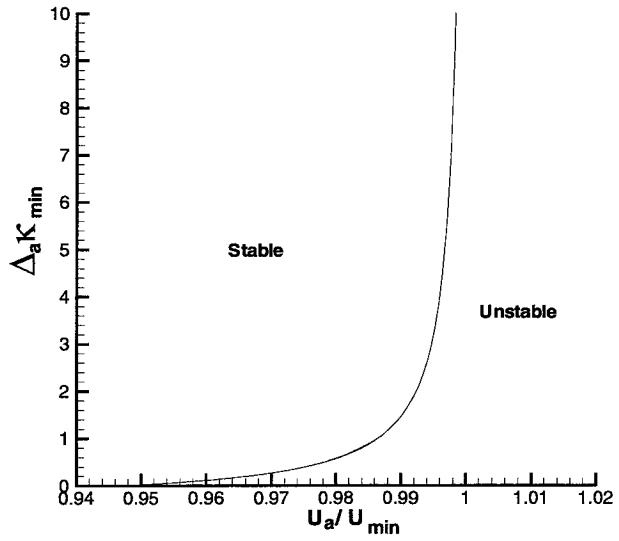

Figure 5.4: Stability boundary for right-traveling perturbations in the $(U, \Delta k)$ plane.

is stable from that in which there exist unstable right-traveling wavenumbers. In the transitional range of wind speeds, in this case $1 > U > \sqrt{1+s}/(1+\gamma)$, increasing the wind layer thickness can stabilize a flow. This is unlike the results we obtained with a wind profile over still water in Appendix F. We mention that this is a very small range of wind speeds as $\sqrt{1+s}/(1+\gamma) \sim 0.95$ for the typical values $\gamma \equiv U_w/U_a = 0.057$ and $s \equiv \rho_a/\rho_w = 0.001226$.

5.3.2 Left-traveling waves: in the range of the water

To find the wavenumbers k at which the complex wavespeed for the left-traveling waves enters and exits the Howard semicircle, we substitute $C = -\gamma U$ into our dispersion relation. Recall that the range of the profile in the water is $\{-\gamma U, 0\}$. The implicit equation for the entry and exit wavenumbers takes the form

$$\frac{2(s-\gamma\omega)}{\gamma k d_a} - \frac{(1+s)}{2\gamma^2 U^2}\left(\frac{1}{k}+k\right) = -\frac{2}{kd_a}\frac{s}{1+\gamma}\frac{F_a'(1/(1+\gamma))}{F_a(1/(1+\gamma))} - s - \sqrt{1+\left(\frac{2\omega}{kd_a}\right)^2}. \tag{5.37}$$

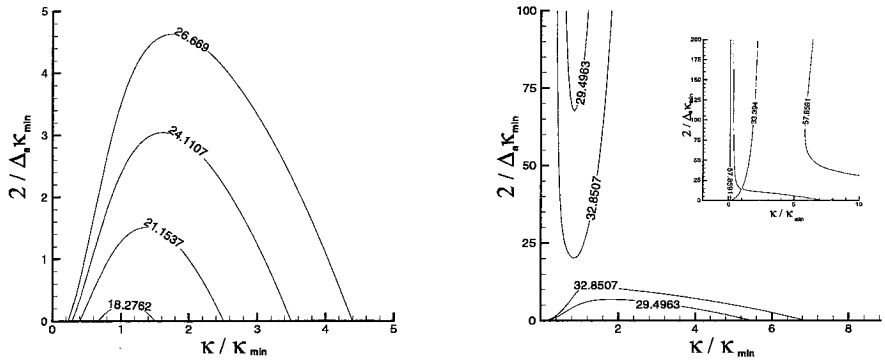

(a) $\sqrt{(1+1/s)}/(1+\gamma) > U > \gamma^{-1}$ (b) $U > \sqrt{(1+1/s)}/(1+\gamma)$

Figure 5.5: Stability boundaries for left-traveling perturbations labeled by nondimensional windspeed $U = U_a/U_{min}$. These curves correspond to waves which travel at the drift layer speed, $c = -\gamma U_a$. The wind-drift speed ratio $\gamma = .057$ was used.

Again, we can not solve explicitly for the layer thickness as a function of wavenumber due to the Hypergeometric functions in this equation. Recall that $F_a(Z) = F(p, q, p+q+1, Z)$, where $p = kd_a/2 + \sqrt{(kd_a)^2/4 + 1}$ and $pq = -1$.To investigate the unstable region, we define the inverse layer $a = 2/d_a$ and use equation (5.37) to make plots for various wind speeds in the (k, a) plane; see Figure 5.5. For a given wavespeed and layer thickness we may determine the entry and exit wavenumbers $C(k_{w1}) = C(k_{w2}) = -\gamma U$ and conclude that the wavenumbers between k_{w1} and k_{w2} are unstable left-traveling waves.

We find that when the slowest gravity-capillary wave is faster than drift layer speed, i.e. $1 > \gamma U$, the dispersion relation does not enter the semicircle from the left implying that all left-traveling waves are stable. For values of wind speed U such that $\sqrt{(1+1/s)}/(1+\gamma) > U > \gamma^{-1}$ there is a region of instability for a range of layer thicknesses starting in the gravity-capillary limit (layer thickness $d_a = \Delta_a \kappa_{\min} \to \infty$) and extending to a finite layer thickness dependant on U; thin layers remain stable. The stability boundary when the wind velocity is in this range is an inverted u-shaped curve $a(k)$ with the endpoints $a(k_2^-) = 0$, and $a(k_2^+) = 0$ and with a maximum value which increases with increasing U, see Figure 5.5. The area under this curve for a given

U is an unstable region. The values of $k_2^{\pm}$ may be determined directly from equation (5.37) or by solving the gravity-capillary dispersion relation (5.25) for $c = -\gamma U_a$ and nondimensionalizing; one finds

$$k_2^{\pm} = (\gamma U)^2 \pm \sqrt{(\gamma U)^4 - 1}. \tag{5.38}$$

Notice in Figure 5.5 that for wind speeds greater than $\sqrt{(1+1/s)}/(1+\gamma)$ there is a second unstable region which extends down from the Kelvin-Helmholtz limit ($d_a = \Delta_a \kappa_{\min} \to 0$) as well as the original unstable region which reaches up from the gravity-capillary region ($d_a = \Delta_a \kappa_{\min} \to \infty$). When the wind speed is in the range $U_c > U > \sqrt{(1+1/s)}/(1+\gamma)$, where U_c is a critical speed, these two unstable regions are not connected. For wind speeds U in this range, the sperate regions of instability indicates that thick and thin layer are unstable and that there exists an intermediate range of layer thickness for which all waves are stable. For a windspeed ratio of $\gamma = 0.044$ we observe from computations that $U_c \simeq 41.28$, while for $\gamma = 0.057$, $U_c \simeq 33.39$. The stability boundary for this second unstable region is defined by a u-shaped curve with endpoints $(k, a) = \left(k_b^{\pm}, \infty\right)$. The wavenumbers $k_b^{\pm}$ correspond to the Kelvin-Hemlholtz waves which travel at the speed $-\gamma U_a$:

$$k_b^{\pm} = \frac{U^2 (1+\gamma)^2 s}{1+s} \pm \frac{\sqrt{U^4 (1+\gamma)^4 s^2 - (1+s)^2}}{1+s}. \tag{5.39}$$

We produce a curve in the space of wind speed vs. layer thickness for $\gamma = 0.044$ shown in Figure 5.6. This curve separates the region in which any perturbation is stable from that in which there exist unstable wavenumbers. As the layer thickness Δ_a tends to infinity, the curve tends to $U_a/U_{\min} = 1/\gamma \simeq 22.73$. Notice that this curve has a fold corresponding to the point at which the two unstable regions in Figure 5.5 (b) meet.

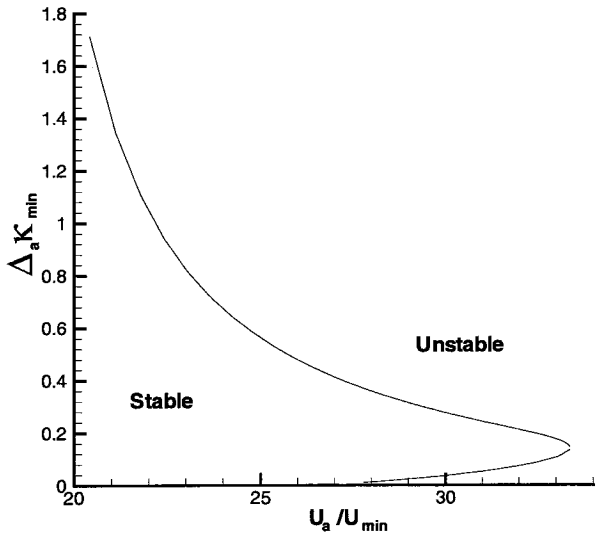

Figure 5.6: Stability boundary in the $(U, \Delta k)$ for left-traveling waves.

5.4 Complex wavespeed results

In this section we study the unstable wavenumbers resulting from the simple model discussed in the previous section. That is, we calculate the complex wavespeed c resulting from unstable perturbations $\eta = \exp(i\kappa(x - ct))$ to the interface between wind and a drift layer. Recall that the number of parameters in our background profile,

$$U(y) = \left\{ \begin{array}{ll} U_a \left(1 - \exp\left[-2y/\Delta_a\right]\right) & y > 0 \\ U_w \left(\exp\left[2y/\Delta_w\right] - 1\right) & y < 0 \end{array} \right\}, \tag{5.40}$$

was reduced by the assumptions of continuity of tangential stress and of proportionality of wind and drift speeds: $\rho_a \nu_a U_a/\Delta_a = \rho_w \nu_w U_w/\Delta_w$ and $U_w/U_a = \gamma$. For air and water, the ratios of densities and viscosities assume the values $\rho_a/\rho_w = s \simeq 0.001226$ and $\nu_a/\nu_w \simeq 14.94$. To maintain consistency with the previous section, we choose the speed ratio $\gamma = 0.057$. As we have shown, the implicit dispersion relations resulting

from this profile may be written as

$$\frac{2\left(s-\gamma\omega\right)U_a}{\kappa\Delta_a c}+\frac{1}{c^2}\left(g\frac{1-s}{\kappa}+\kappa\frac{T}{\rho_w}\right)=1+s+\frac{2}{\kappa\Delta_a}\omega Z_2\frac{F_w'\left(Z_2\right)}{F_w\left(Z_2\right)}+s\frac{2}{\kappa\Delta_a}Z_1\frac{F_a'\left(Z_1\right)}{F_a\left(Z_1\right)} \tag{5.41}$$

where $\omega=\Delta_a/\Delta_w$, $Z_1=1/\left(1-c/U_a\right)$ and $Z_2=1/\left(1+c/U_w\right)$.

Also in this section, we will make comparisons with the complex waves speeds resulting from a simpler velocity profile studied by Caponi *et al.* [2] known as a "stick profile." Such a profile is a piecewise continuous velocity profile defined as

$$U\left(y\right)=\left\{\begin{array}{ll} U_a & y>\Delta_a \\ U_a y/\Delta_a & \Delta_a>y>0 \\ U_w y/\Delta_w & 0>y>-\Delta_w \\ -U_w & -\Delta_w>y \end{array}\right\}. \tag{5.42}$$

Notice that the stick profile was constructed to have the same vorticity centroids (the integral of yU_y over the air or the water) as the smooth profile. Compared with equation (5.41) the implicit dispersion relation for the stick profile is relatively simple in that the dependence on c is only algebraic:

$$\begin{aligned} &\frac{\kappa\Delta_a\left(\gamma+c/U_a\right)-\gamma\omega e^{-\kappa\Delta_a/\omega}\cosh\left(\kappa\Delta_a/\omega\right)}{\kappa\Delta_a\left(\gamma+c/U_a\right)-\gamma\omega e^{-\kappa\Delta_a/\omega}\sinh\left(\kappa\Delta_a/\omega\right)} \\ =\;&\frac{\left(s-\gamma\omega\right)U_a}{\kappa\Delta_a c}+\frac{1}{c^2}\left(g\frac{1-s}{\kappa}+\kappa\frac{T}{\rho_w}\right)-s\frac{\kappa\Delta_a\left(1-c/U_a\right)-e^{-\kappa\Delta_a}\cosh\left(\kappa\Delta_a\right)}{\kappa\Delta_a\left(1-c/U_a\right)-e^{-\kappa\Delta_a}\sinh\left(\kappa\Delta_a\right)}. \end{aligned} \tag{5.43}$$

We mention that unlike the spectra for the exponential profile, there may be stable perturbations with wavespeed in the range of the stick profile since such behavior does not necessarily introduce a singularity in Rayleighs equation, $\phi_{yy}-\left(\kappa^2+U_{yy}/(U-c)\right)\phi=0$, as U_{yy} is zero almost everywhere. We also mention that in their study of drift layers, Morland, Saffman and Yuen [24], observed that stick profiles generally predict much higher growth rates than smooth profiles.

Before we calculate the unstable wavespeeds resulting from perturbations to the smooth profile (5.40); recall that in the absence of wind and drift, the dispersion

relation produces the gravity-capillary waves speed $\pm c_o(\kappa)$ defined by

$$c_o(\kappa) = \sqrt{\left(g\frac{(1-s)}{\kappa} + T\frac{\kappa}{\rho_w}\right)/(1+s)} \tag{5.44}$$

where g and T represent gravity and surface tension. This dispersion relation has a minimum wavespeed $U_{\min}$ occurring at the wavenumber $\kappa_{\min}$. In our examination of stability regions resulting from the wind and drift profile, we determined that left and right traveling perturbations may be unstable. These perturbations could be thought of as continuations of $+c_o(k)$ and $-c_o(k)$ respectively. Such an observation motivates nondimensionalizing the implicit dispersion relation on the speed $c_o(k)$. We did this earlier when examining the large layer limit, $\Delta\kappa \to \infty$, and found that the implicit dispersion relation, equation (5.41), becomes

$$s - \omega\gamma + \kappa\Delta_a\frac{1+s}{2\widehat{U}}\left(\frac{1}{\widehat{c}} - \widehat{c}\right) = \frac{\widehat{c}}{\widehat{U}}\left(sZ_1\frac{F_a'(Z_1)}{F_a(Z_1)} + \omega Z_2\frac{F_w'(Z_2)}{F_w(Z_2)}\right) \tag{5.45}$$

with $Z_1 = 1/\left(1-\widehat{c}/\widehat{U}\right)$, $Z_2 = \gamma/\left(\gamma+\widehat{c}/\widehat{U}\right)$ and where $\widehat{c} = c/c_o(\kappa)$, $\widehat{U} = U_a/c_o(\kappa)$. We observe that $\widehat{c}$ is just a function of two parameters: $\widehat{U}$ and $\kappa\Delta_a$. Contour plots of $\Re(\widehat{c})$ and $\Im(\widehat{c})$, see Figures 5.7 (a) and (b), allow us to identify and summarize the behavior of unstable perturbations for various wind speeds and layer thicknesses. For comparison we have included the contour plot of $\Im(\widehat{c})$ generated by the stick profile. Notice that there are qualitative similarities between the unstable regions for the smooth and stick profiles (Figure 5.7 (b) and Figure 5.8 respectively) but the stick profile has compact unstable regions and predicts much higher growth rates.

We proceed in the manner of Caponi *et al.* [2] and examine the response of specific wavenumbers. To make predictions about the response of given wavenumber as wind speed increases while the layer thickness is held constant, one examines the horizontal line $\Delta_a\kappa = const.$ For instance, if we fix $\Delta_a\kappa = 0.5$, such a model predicts that as wind speed increases, the right-traveling wave with wavenumber κ become unstable when $U_a/c_o(\kappa)$ is near one. Initially the growth rate of such waves increases until $U_a/c_o(\kappa) \sim 8$ and then decreases. At $U_a/c_o(\kappa) \sim 27$ the left-traveling wave

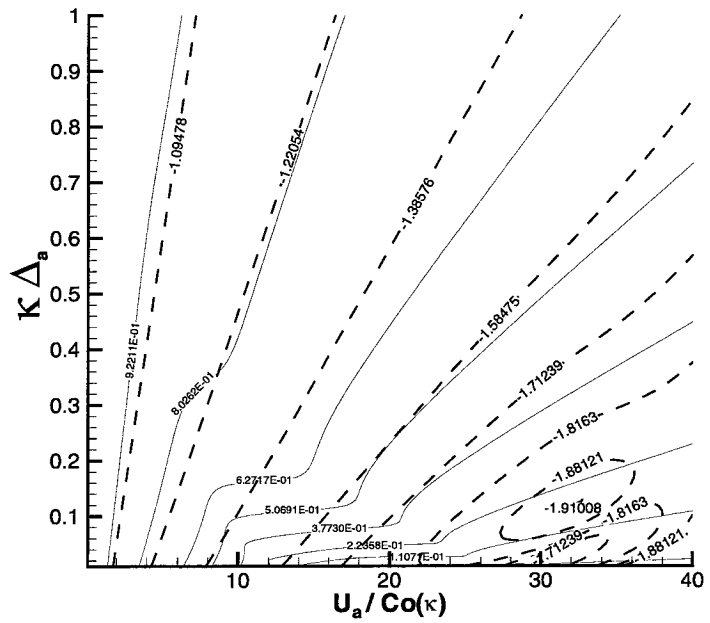

(a) The real wave speed, $Re(c)$ for $\gamma = 0.057$

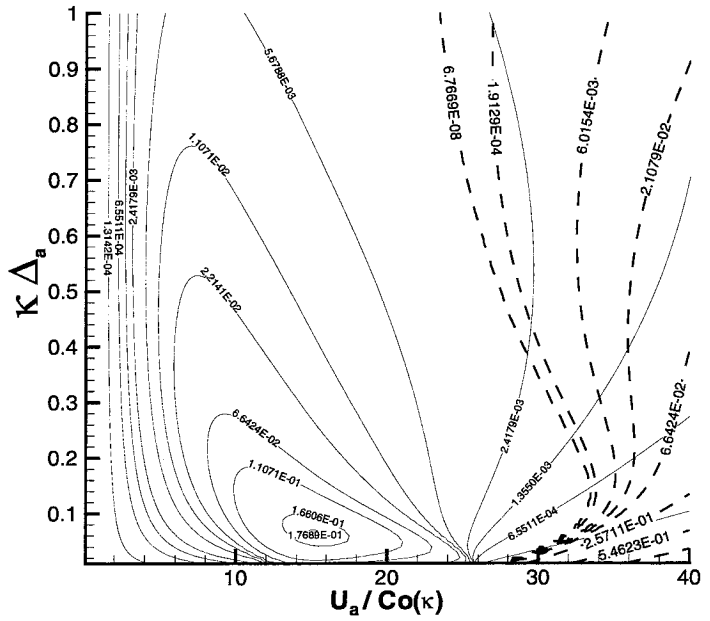

(b) $Im(c)$ for $\gamma = 0.057$

Figure 5.7: Contour plot of nondimensional eigenvalues, $c/c_o(\kappa)$, for $\gamma = 0.057$. Solid lines are right-traveling and dotted lines are left-traveling.

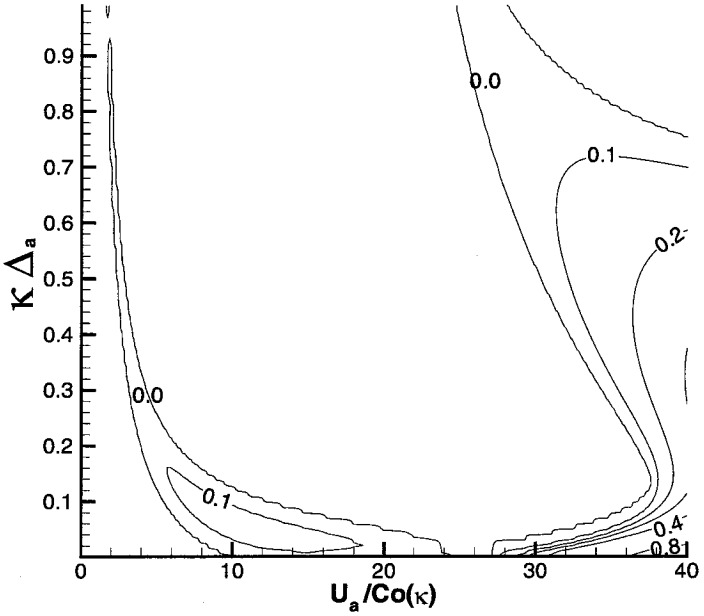

Figure 5.8: Contour plots of $Im(c/c_o(\kappa))$ for $\gamma = 0.057$ produced by the stick profile.

becomes unstable and quickly surpasses the right-traveling wave in growth rate. This suggests that as one watches a gust of wind blowing across water, initially waves of a given wavelength appear, then disappear only to be replaced by the same wave length traveling at a different speed. In a similar manner, one could also consider an idealization of the generation of an initial spectrum by a constant wind as the air and water layers grow with time. As the layer thickens, the response of an individual wavenumbers κ for fixed wind speed U_a is predicted by looking along the vertical line defined by $U_a/c_o(\kappa) = const.$

A few qualitative observations about the unstable dispersion relation can be made from Figure 5.7 (b) with fixed wind speed U_a and layer thickness Δ_a. In order to make these observations we must first notice that the curve $(U_a/c_o(\kappa), \Delta_a\kappa)$ parameterized by $\kappa \in (0, \infty)$ has two branches which meet at a fold located at $(U_a/U_{\min}, \Delta_a\kappa_{\min})$. The lower branch corresponds to gravity waves, $0 < \Delta_a\kappa < \Delta_a\kappa_{\min}$; it connects the origin and the fold. The upper branch, $\Delta_a\kappa_{\min} < \Delta_a\kappa < \infty$, represents capillary waves and it connects the fold to the limit $(U_a/c_o(\kappa), \Delta_a\kappa) = (0, \infty)$. Looking at

Figure 5.7 (b), when the fold $(U_a/U_{\min}, \Delta_a\kappa_{\min})$ is to the left of the unstable region for left-going waves, only the right-traveling waves will be unstable. In this case we will find two distinct peaks in the growth rates for these waves. These two peaks correspond to the gravity and capillary branches of the curve $(U_a/c_o(\kappa), \Delta_a\kappa)$ passing over the most unstable regions for right-traveling waves in Figure 5.7 (b). When the fold is moved to a point with in the unstable region for left-traveling waves, there will still be the gravity and capillary peaks in the right-traveling spectra; but there will now also be a peak associated with the left-traveling waves with wavenumbers near the fold.

To gain a better understanding of the growth rates $\Im(\sigma) \equiv \Im(\kappa c) / (\kappa_{\min} U_{\min})$ for fixed U_a and Δ_a, a series of plots has been constructed from the dispersion relation for the exponential profiles in air and water. In Figure 5.9 the wind speed $U_a/U_{\min}$ is held at 44 while the layer thickness $\Delta_a\kappa_{\min}$ is varied; (a) and (b) show the gravity and capillary peaks for right going wave, while (c) shows the peak for left-going waves. Notice that the peaks diminish and move to lower wavenumbers as the layer thickness increases. Also notice that the left-traveling waves are the most unstable and the gravity right-going waves become more unstable than the capillary right-traveling waves as the depth increases. In Figure 5.10 the layer thickness $\Delta_a\kappa_{\min}$ is held at 0.6 while the wind velocity, and hence drift speed, is varied. We see in Figure 5.10 (a) and (b) that the gravity and capillary peaks for the right-traveling waves separate as wind speed increases. Higher values of the wind speed lead to unstable left-going waves; see Figure 5.10 (c).

As we mentioned earlier, the stick profile may lead to growth rates $\Im(\sigma)$ which are much larger than those predicted by smooth profiles. The wavenumbers corresponding to the maximally unstable waves, i.e. the peaks of $\Im(\sigma)$, on the other hand, are in reasonable agreement. As an example, in Table 5.1 we compare the maximal growth rates and corresponding wavenumbers for left-traveling waves resulting from both profiles for various layer thicknesses. In Table 5.2 we compare the right-traveling gravity and capillary peaks of the exponential profile; also included for comparison are the gravity peaks predicted by the stick profile.

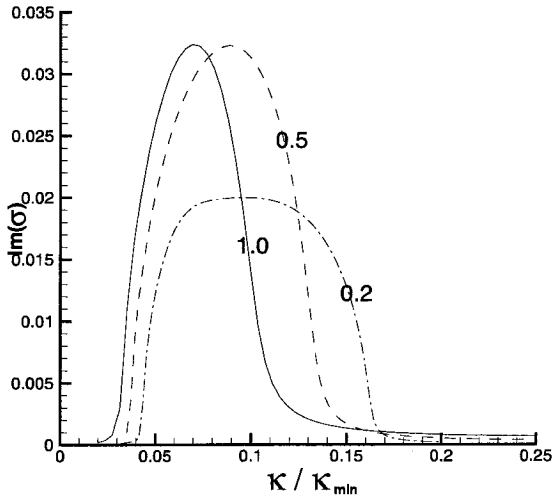

(a) The gravity peak for right-traveling waves

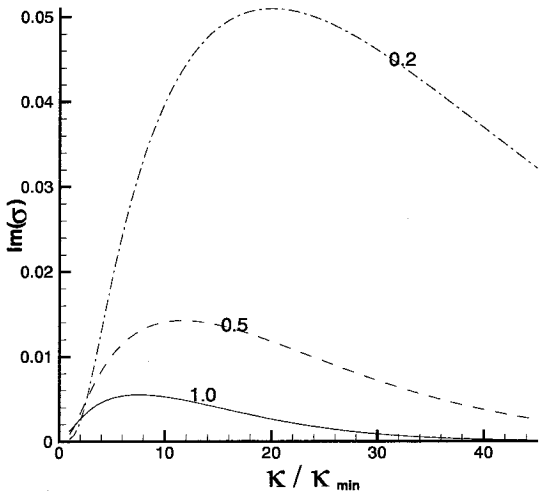

(b) The capillary peak for right-traveling waves

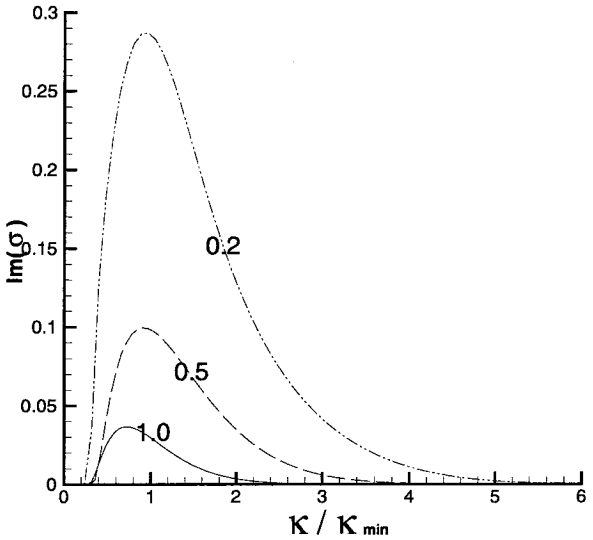

(c) The peak for left-traveling waves

Figure 5.9: Growthrate peaks computed for various depths $\Delta_a \kappa_{min}$ and fixed wind speed $U_a/U_{min} = 44$.

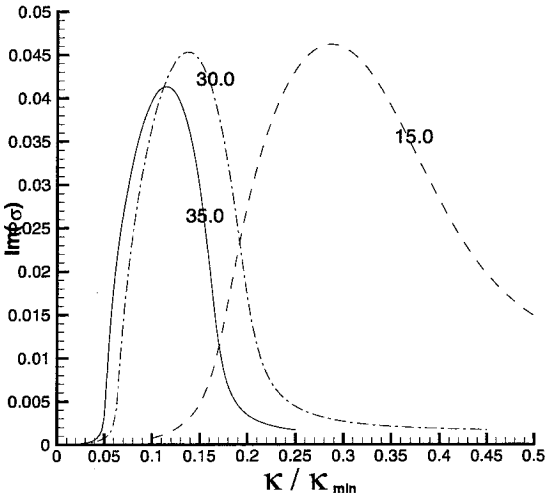

(a) The gravity peak for right-traveling waves

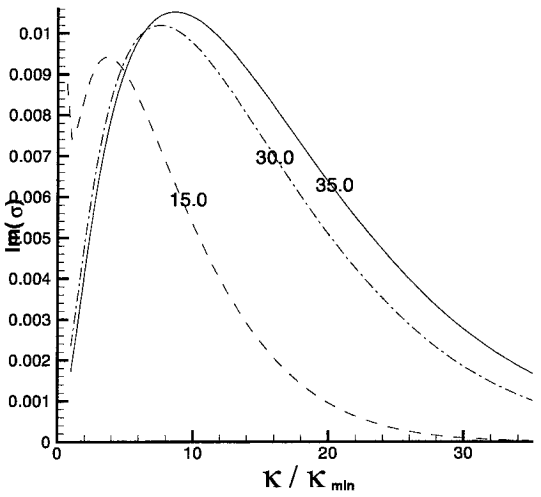

(b) The capillary peak for right-traveling waves

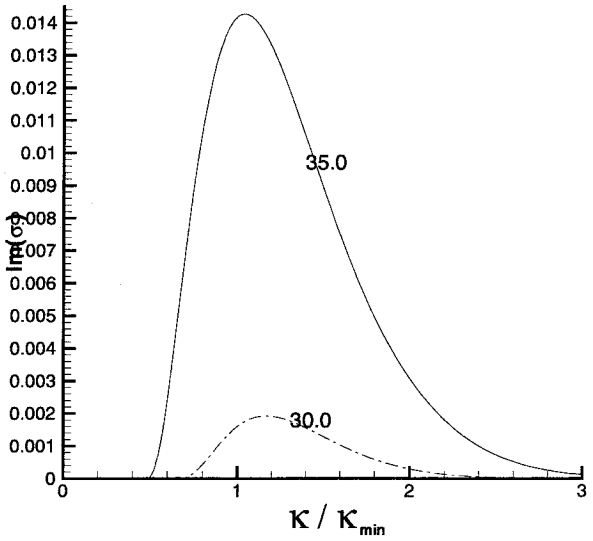

(c) The peak for left-traveling waves

Figure 5.10: Growthrate peaks computed for various wind speeds U_a/U_{min} and fixed layer depths $\Delta_a \kappa_{min} = 0.6$.

	(a)		(b)	
$\Delta_a \kappa_{\min}$	$k_{\max}$	$\Im(\sigma)$	$k_{\max}$	$\Im(\sigma)$
0.1	1.1135	0.57807	1.5242	0.5776
0.2	0.9305	0.28716	2.1745	0.6015
0.3	0.9452	0.17878	1.5332	0.4724
0.5	0.9134	0.09954	0.9561	0.2963
0.6	0.8703	0.07909	0.8146	0.2447
0.7	0.8277	0.06406	0.7114	0.2065
0.8	0.7885	0.05264	0.6396	0.1773
0.9	0.7533	0.04376	0.5816	0.1542
0.0001	3.4121	3.0215	3.4051	3.0160

Table 5.1: The most unstable left-traveling waves for various depths calculated by (a) the exponential profile and (b) the stick profile. Quantities have been nondimensionalized with respect to U_{min} and κ_{min}. The wind speed U_a is fixed at $44U_{min}$.

	(a)		(b)		(c)	
$\Delta_a \kappa_{\min}$	$k_{\max}$	$\Im(\sigma)$	$k_{\max}$	$\Im(\sigma)$	$\kappa_{\max}$	$\Im(\sigma)$
0.1	0.0636	0.0123	29.0073	0.13655	0.0710	0.0181
0.2	0.0967	0.0200	19.9596	0.05963	0.0803	0.0270
0.3	0.0970	0.0265	15.8004	0.02889	0.0734	0.0302
0.4	0.0934	0.0303	13.3202	0.01938	0.0669	0.0310
0.5	0.0890	0.0322	11.6405	0.01433	0.0614	0.0309

Table 5.2: The most unstable right-traveling waves for various depths. The peaks for the gravity (a) and capillary (b) branches of the exponential profile are given as is the gravity (c) peak for the stick profile. Quantities have been nondimensionalized with respect to U_{min} and κ_{min}. The wind speed U_a is fixed at $44U_{min}$.

Appendixes and Bibliography

Appendix A Matrix elements in Föppl stability

In examining the stability of the vortex pair behind an elliptical cylinder in Chapter One, it is necessary to calculate matrix elements. Given a stationary location for the vortex pair in the non-physical z-plane, $z^s = x_1^s \pm iy_1^s$, the appropriate linearized system (1.41) has the following matrix element relations:

$$\begin{array}{llll} M_{21} = M_{12} + A_1 & M_{22} = -M_{11} & M_{23} = -M_{14} + A_2 & M_{24} = M_{13} \\ M_{31} = M_{13} & M_{32} = -M_{14} & M_{33} = M_{11} & M_{34} = -M_{12} \\ M_{41} = -M_{23} & M_{42} = M_{13} & M_{43} = -M_{21} & M_{44} = -M_{11} \end{array} \tag{A.1}$$

where $M_{i,j}$ are the elements of the matrix $\mathbf{M}$ in (1.41).

In studying the stationary vortex pair represented in the non-physical plane by $z^s = x \pm iy$ we calculate first the appropriate vortex strength Γ and then fundamental matrix elements as

$$\begin{aligned} M_{11}(\frac{a}{U}) &= 2a^3\sqrt{r^2-y^2}\frac{(r^2-4y^2)}{r^6} \\ &\quad -\frac{\Gamma}{2\pi Ua}a^2 2y\sqrt{r^2-y^2}\{\frac{1}{(r^2-a^2)^2}+\frac{(a^4-r^4)}{((a^2-r^2)^2+4a^2y^2)^2} \\ &\quad +\lambda a^2\frac{y^2(4r^4+8(\lambda a^2-r^2)^2)+\lambda a^2(2r^2-\lambda a^2)^2+\lambda a^2(5r^4+16y^4)-6r^6}{r^4((\lambda a^2-r^2)^2+4\lambda a^2y^2)^2}\}, \end{aligned} \tag{A.2}$$

$$\begin{aligned} M_{12}\left(\frac{a}{U}\right) &= 2a^3y\frac{(3r^2-4y^2)}{r^6}-\frac{\Gamma}{2\pi Ua}a^2\{\frac{2y^2+a^2-r^2}{(a^2-r^2)^2}+\frac{1}{4y^2} \\ &\quad +\frac{r^2((a^2-r^2)^2+4a^2y^2)-2y^2(a^2+r^2)^2}{((a^2-r^2)^2+4a^2y^2)^2} \\ &\quad +\lambda^2a^4\frac{\lambda^2a^4(2y^2-r^2)+\lambda a^2(5r^4-16r^2y^2+16y^4)}{r^4((\lambda a^2-r^2)^2+4\lambda a^2y^2)^2} \end{aligned} \tag{A.3}$$

$$\quad +\lambda^2a^4\frac{(-7r^6+30r^4y^2-48r^2y^4+32y^6)}{r^4((\lambda a^2-r^2)^2+4\lambda a^2y^2)^2} \tag{A.4}$$

$$+\lambda a^2 \frac{3r^8 - 24r^6y^2 + 24r^4y^4}{r^4((\lambda a^2 - r^2)^2 + 4\lambda a^2 y^2)^2}\},$$

$$M_{13}\left(\frac{a}{U}\right) = \frac{\Gamma}{2\pi U a} 4ya^2 \sqrt{r^2 - y^2} \frac{(r^2 - a^2 - 2y^2)}{((a^2 - r^2)^2 + 4a^2y^2)^2}, \tag{A.5}$$

$$M_{14}\left(\frac{a}{U}\right) = \frac{\Gamma}{2\pi U a} a^2 \{\frac{1}{4y^2} + a^2 \frac{(a^2 - r^2)^2 + 4y^2(a^2 - 2r^2 + 2y^2)}{((a^2 - r^2)^2 + 4a^2y^2)^2}\}, \tag{A.6}$$

and

$$A_1\left(\frac{a}{U}\right) = \frac{\Gamma}{2\pi U a} \frac{2a^2}{(r^2 - a^2)^2} \tag{A.7}$$

$$A_2\left(\frac{a}{U}\right) = \frac{\Gamma}{2\pi U a} \frac{a^2}{2y^2}, \tag{A.8}$$

where $r = \sqrt{x^2 + y^2}$.

Appendix B Computation of the image correction

We adopt spherical co-ordinates for the task of finding the order ϵ corrections to the scalar potential:

$$x = r\sin\theta\cos\phi \tag{B.1}$$

$$y = r\sin\theta\sin\phi \tag{B.2}$$

$$z = r\cos\theta \tag{B.3}$$

so the location of the centerline of the perturbed vortex ring is given by

$$x_r = \left(R+\epsilon r_o e^{in\phi}\right)\cos\phi \tag{B.4}$$

$$y_r = \left(R+\epsilon r_o e^{in\phi}\right)\sin\phi \tag{B.5}$$

$$z_r = Z+\epsilon\zeta_o e^{in\phi}. \tag{B.6}$$

At a given a point $\left(r_p,\theta_p,\phi_p\right)$we find the induced velocity in the radial direction is given by

$$\begin{aligned}\mathbf{n}_r\cdot\mathbf{u}\left(\mathbf{x}_p\right) &= -\vec{n}_r\cdot\frac{\Gamma}{4\pi}\oint\frac{\left(\mathbf{x}_p-\mathbf{R}\left(s\right)\right)}{\left|\mathbf{x}_p-\mathbf{R}\left(s\right)\right|^3}\times d\mathbf{s} \\ &\sim \frac{\Gamma}{4\pi}\int_0^{2\pi}\frac{R\left(R\cos\theta_p-Z\cos t\sin\theta_p\right)}{D^{3/2}}dt \\ &\quad +\epsilon\frac{\Gamma}{4\pi}e^{in\phi_p}\left(r_oA_r+\zeta_oA_\zeta\right)+O\left(\epsilon^2\right)\end{aligned} \tag{B.7}$$

where

$$\begin{aligned}A_r &= \int_0^{2\pi}\frac{2R\cos\theta_p\cos nt+Z\sin\theta_p\left(n\sin nt\sin t-\cos t\cos nt\right)}{D^{3/2}}dt \\ &\quad -3R\int_0^{2\pi}\cos nt\frac{\left(R\cos\theta_p-Z\cos t\sin\theta_p\right)\left(R-r\cos t\sin\theta_p\right)}{D^{5/2}}dt\end{aligned} \tag{B.8}$$

and

$$\begin{aligned} A_\zeta &= -R\sin\theta_p \int_0^{2\pi} \frac{\cos t\cos nt + n\sin nt\sin t}{D^{3/2}}dt \\ &\quad -3\left(Z - r\cos\theta_p\right)R\int_0^{2\pi}\cos nt\frac{\left(R\cos\theta_p - Z\cos t\sin\theta_p\right)}{D^{5/2}}dt \end{aligned} \tag{B.9}$$

with D as

$$D = r_p^2 + R^2 + Z^2 - 2r_pZ\cos\theta_p - 2r_pR\cos t\sin\theta_p. \tag{B.10}$$

From the boundary condition of no flow into the sphere (2.33), we find the condition

$$\frac{\partial\varphi_n^r}{\partial r} + \frac{\Gamma}{4\pi}A_r = 0 \tag{B.11}$$

$$\frac{\partial\varphi_n^\zeta}{\partial r} + \frac{\Gamma}{4\pi}A_\zeta = 0 \tag{B.12}$$

evaluated at the sphere's surface, $r = a$. Solving $\nabla^2\left(e^{in\theta}\varphi_n^r, e^{in\theta}\varphi_n^\zeta\right) = (0,0)$ subject to these boundary conditions, and using the requirement that the flow due to these corrections tends to zero for large distances, gives

$$\begin{pmatrix} \varphi_n^r \\ \varphi_n^\zeta \end{pmatrix} = \frac{\Gamma}{4\pi}\sum_{j=n}\begin{pmatrix} C_j^r \\ C_j^\zeta \end{pmatrix} r^{-j-1}\sqrt{\frac{2j+1}{2}\frac{(j-n)!}{(j+n)!}}P_j^n\left(\cos\theta\right) \tag{B.13}$$

where

$$\begin{pmatrix} C_j^r \\ C_j^\zeta \end{pmatrix} = \frac{a^{j+2}}{j+1}\sqrt{\frac{2j+1}{2}\frac{(j-n)!}{(j+n)!}}\int_0^\pi \begin{pmatrix} A_r\left(r=a,\theta\right) \\ A_\zeta\left(r=a,\theta\right) \end{pmatrix} P_j^n\left(\cos\theta\right)\sin\theta d\theta. \tag{B.14}$$

The functions $P_j^n\left(x\right)$ are associated Legendre functions.

Appendix C The Counter-Rotating Point Vortex Pair in Linear Flow

In two-dimensional incompressible fluid flow, we refer to two delta functions of vorticity with equal strength and opposite signs as a counter-rotating point vortex pair. In this appendix we solve for the general time dependent evolution of such a configuration embedded in unbounded linear flow.

The complex velocity for a vortex pair in a linear background flow is given by

$$u - iv = \gamma \exp(-i\phi)\, z + \alpha y + i\beta x + \frac{i}{2\pi}\frac{\Gamma}{z - z_-} - \frac{i}{2\pi}\frac{\Gamma}{z - z_+} \tag{C.1}$$

where $z_\pm$ is the location of the vortex with strength $\pm\Gamma$. Since each point vortex is advected by the linear background and the flow induced by the other vortex, the velocities of the vortices are given by

$$\frac{d}{dt}\overline{(z_+)} = \gamma \exp(-i\phi)\, z_+ + \alpha y_+ + i\beta x_+ + \frac{i}{2\pi}\frac{\Gamma}{z_+ - z_-} \tag{C.2}$$

$$\frac{d}{dt}\overline{(z_-)} = \gamma \exp(-i\phi)\, z_- + \alpha y_- + i\beta x_- + \frac{i}{2\pi}\frac{\Gamma}{z_+ - z_-}. \tag{C.3}$$

C.0.1 Finding the orientation and separation of the vortex pair

Physically we can de-couple the orientation and separation of the vortex pair from its absolute location. Defining

$$R \exp(i\theta) = z_- - z_+ \tag{C.4}$$

implies that R will be the separation between vortices and θ will describe the angle that a line passing through the vortex pair will make with the x-axis. Using the

overdot to denote the time derivative, we see that

$$\dot{R}\, e^{i\theta} + i\dot{\theta} R\, e^{i\theta} = \gamma \exp\left(i\phi - i\theta\right) R + \alpha R \sin\theta - i\beta R \cos\theta.$$

Spliting into real and imaginary parts and simplifying leads to two differential equations:

$$\dot{\theta} = \gamma \sin\left(\phi - 2\theta\right) - \beta \cos^2\theta - \alpha \sin^2\theta \tag{C.5}$$

$$\dot{R} = R\left\{\frac{1}{2}(\alpha - \beta)\sin(2\theta) + \gamma \cos\left(\phi - 2\theta\right)\right\}. \tag{C.6}$$

Notice that the equation for the orientation θ is independent of the separation R so that we may first solve for the orientation as a function of time and then integrate the equation for the separation,

$$R(t) = R(0) \exp\left[\int_0^t \frac{1}{2}(\alpha - \beta)\sin\left(2\theta\right) + \gamma \cos\left(\phi - 2\theta\right)\, d\tau\right]. \tag{C.7}$$

Alternately, for constant background flows, the separation $R(t)$ may also be determined from the orientation by noting that

$$\Psi = R^2\left(\alpha \sin^2\theta + \beta \cos^2\theta + \gamma \sin(2\theta - \phi)\right) \tag{C.8}$$

is a constant of the motion.

In order to find the orientation, we re-write the differential equation as

$$\frac{d}{dt}\tan\theta = -\left(\gamma \sin\phi + \alpha\right)\tan^2\theta - \left(2\gamma\cos\phi\right)\tan\theta - \left(\beta - \gamma\sin\phi\right). \tag{C.9}$$

This differential equation may be solved for a variety of time dependant background flows, but here we choose to give the general solution for the steady background case. From the integral

$$\int \frac{dx}{Ax^2 + Bx + C} = 2\arctan\left(\frac{B + 2Ax}{\sqrt{4AC - B^2}}\right) / \sqrt{4AC - B^2} \tag{C.10}$$

$$\text{or} = -2\tanh^{-1}\left(\frac{B+2Ax}{\sqrt{B^2-4AC}}\right)/\sqrt{B^2-4AC} \quad \text{(C.11)}$$

$$\text{or} = \frac{-2}{B+2Ax} \text{ when } B^2 = 4AC \text{ and } A \neq 0 \quad \text{(C.12)}$$

$$\text{or} = \log\left(x + C/B\right)/B \text{ when } A = 0 \quad \text{(C.13)}$$

where

$$A = -\gamma\sin\phi - \alpha \quad \text{(C.14)}$$

$$B = -2\gamma\cos\phi \quad \text{(C.15)}$$

$$C = -\beta + \gamma\sin\phi \quad \text{(C.16)}$$

we see that the background flow determines if the vortex pair will tumble in its orientation, or settle to a steady direction. We may classify four different types of steady background flow simply from the values of A, B, and C. To gain insight the we examine the streamfunction for the linear background flow,

$$\psi_b = -\frac{1}{2}\left(Ay^2 - Bxy + Cx^2\right), \quad \text{(C.17)}$$

and we find that $\psi_b = const$ corresponds to closed curves, i.e. ellipses, only when $D^2 \equiv 4AC - B^2 > 0$.

Since the orientation of the vortex pair is a driven by the linear flow alone, it is not surprizing that when $D^2 > 0$ we find that

$$\tan\theta = \frac{D}{2A}\tan\left(\frac{D}{2}t + \arctan\left(\frac{B+2A\tan\theta_o}{D}\right)\right) - \frac{B}{2A} \quad \text{(C.18)}$$

which implies that the counter-rotating vortices will tumble about each other. While for other background flows the pair will tend to a fixed orientation. When $D^2 < 0$ and $A \neq 0$ the orientation will obey

$$\tan\theta = \frac{|D|}{2A}\tanh\left(\frac{|D|}{2}t + \operatorname{arctanh}\left(\frac{B+2A\tan\theta_o}{|D|}\right)\right) - \frac{B}{2A} \quad \text{(C.19)}$$

which in the long time limits to $\tan\theta = (B \pm |D|)/(2A)$. While if $D^2 < 0$ and $A = 0$ we find

$$\tan\theta = e^{Bt}\tan\theta_o + \left(e^{Bt} - 1\right)\frac{C}{B} \tag{C.20}$$

so that the final angle will be $\pm\pi/2$ or $\arctan(-C/B)$ depending on the sign of B. And the case $D = 0$ with $A \neq 0$ gives the solution

$$\tan\theta = -\frac{B}{2A} - \left(\frac{2\tan\theta_o + B/A}{t(B + 2A\tan\theta_o) - 2}\right) \tag{C.21}$$

which tends to $\tan\theta = B/(2A)$ algebraically.

C.0.2 Finding the absolute location of the vortex pair

Now that we have the orientation and separation of the vortex pair as functions of time, we give an analytic form for the location of the vortex pair relative to the origin. Define $z_c = X + iY$ as the vector from the origin to a point halfway between the vortices,

$$z_c = \frac{1}{2}(z_+ + z_-). \tag{C.22}$$

The evolution of this point is given by

$$\overline{(\dot{z}_c)} = z_c\gamma e^{-i\phi} + \alpha Y + i\beta X - i\frac{\Gamma}{2\pi R}e^{-i\theta}. \tag{C.23}$$

We re-write this complex equation as two coupled ordinary differential equations by grouping real and imaginary parts;

$$\frac{d}{dt}\begin{pmatrix} X \\ Y \end{pmatrix} = \mathbf{M}\begin{pmatrix} X \\ Y \end{pmatrix} + \mathbf{f} \tag{C.24}$$

where

$$\mathbf{M} = \begin{pmatrix} \gamma\cos\phi & \gamma\sin\phi + \alpha \\ \gamma\sin\phi - \beta & -\gamma\cos\phi \end{pmatrix} \quad \text{and} \quad \mathbf{f} = \frac{\Gamma}{2\pi R}\begin{pmatrix} -\sin\theta \\ \cos\theta \end{pmatrix}.$$

Solving gives

$$\begin{pmatrix} X \\ Y \end{pmatrix} = \underbrace{\exp(t\mathbf{M}) \begin{pmatrix} X_o \\ Y_o \end{pmatrix}}_{\text{advection with background}} + \underbrace{\int_o^t \exp((t-\tau)\mathbf{M})\,\mathbf{f}(\tau)\,d\tau}_{\text{vortex forced motion}}$$

where agreeably enough the homogeneous solution represents the advection of the vortex pair, while the particular solution contains the effect of the self-induced translation of the vortex pair. If one desires, the location of a given vortex can now be easily found;

$$\begin{aligned} z_+ &= X_o + iY_o - \frac{1}{2}R\,e^{i\theta} \\ z_- &= X_o + iY_o + \frac{1}{2}R\,e^{i\theta}. \end{aligned}$$

C.1 Three simple examples

Recall that the instantaneous velocity field representing a point vortex pair embedded in linear flow has the form

$$u - iv = \gamma \exp(-i\phi)\, z + \alpha y + i\beta x - \frac{i}{2\pi}\frac{\Gamma}{z - z_+} + \frac{i}{2\pi}\frac{\Gamma}{z - z_-}. \tag{C.25}$$

By certain prescriptions of the quantities which define the background flow we examine a few basic flows: solid body rotation, constant cross-stream shear, and strain with a time-dependent strength.

C.1.1 Vortex pair in solid body rotation

We begin with the simple case of a background comprising of only solid body rotation. This is obtained by requiring $\alpha = \beta \equiv -\Omega$ and $\gamma = 0$. Not surprisingly the separation of the vortices remains constant, while their relative orientation is simple rotation;

$$\theta = \Omega t + \theta_o \tag{C.26}$$

$$R = R_o. \tag{C.27}$$

Solving for the absolute location gives

$$X = \cos(\Omega t) X_o - \sin(\Omega t) Y_o - \frac{\Gamma t}{2\pi R_o} \sin(\Omega t + \theta_o) \tag{C.28}$$

$$Y = \sin(\Omega t) X_o + \cos(\Omega t) Y_o + \frac{\Gamma t}{2\pi R_o} \cos(\Omega t + \theta_o), \tag{C.29}$$

which we can re-write as a rotation matrix times the solution for the vortex pair moving with no background flow:

$$\begin{pmatrix} X \\ Y \end{pmatrix} = \underbrace{\begin{pmatrix} \cos(\Omega t) & -\sin(\Omega t) \\ \sin(\Omega t) & \cos(\Omega t) \end{pmatrix}}_{\text{Rotation Matrix}} \underbrace{\begin{pmatrix} X_o - \frac{\Gamma}{2\pi R_o} t \sin\theta_o \\ Y_o + \frac{\Gamma}{2\pi R_o} t \cos\theta_o \end{pmatrix}}_{\text{translating pair}}. \tag{C.30}$$

C.1.2 Vortex pair in a linear cross-shear

To produce a simple cross-stream shear we chose $\beta = \gamma = 0$; this leads to the orientation and separation

$$\tan\theta = \frac{\tan\theta_o}{t\alpha \tan\theta_o + 1} \tag{C.31}$$

$$R = R_o \frac{\sin\theta_o}{\sin\theta}. \tag{C.32}$$

Notice that this implies the vertical separation between the point vortices, $R\sin\theta$, is constant; this corresponds to the conservation of linear impulse in the x-direction. The absolute locations are given by the integrations

$$Y = \int_o^t \frac{\Gamma}{2\pi R(\tau)} \cos\theta(\tau)\, d\tau + Y_o \tag{C.33}$$

$$X = \int_o^t \alpha Y(\tau) - \frac{\Gamma}{2\pi R(\tau)} \sin\theta(\tau)\, d\tau + X_o \tag{C.34}$$

which can be easily done by using $\dot{\theta} = -\alpha \sin^2 \theta$. Integrating for Y we find

$$Y = \int_o^t \frac{\Gamma}{2\pi R(\tau)} \cos\theta(\tau)\, d\tau + Y_o \tag{C.35}$$

$$= \frac{\Gamma}{\alpha 2\pi R_o \sin\theta_o} \log\left(\frac{\sin\theta_o}{\sin\theta}\right) + Y_o, \tag{C.36}$$

and likewise for X;

$$X = \int_o^t \alpha Y(\tau) - \frac{\Gamma}{2\pi R(\tau)} \sin\theta(\tau)\, d\tau \tag{C.37}$$

$$= \frac{\Gamma}{2\pi\alpha R_o \sin\theta_o}\left(\frac{1}{\sin\theta_o} - \frac{1+\log\left(\frac{\sin\theta}{\sin\theta_o}\right)}{\sin\theta} + (\theta - \theta_o)\right) + \alpha Y_o t + X_o \tag{C.38}$$

Notice that from the differential equation for θ, we see that $\frac{\sin\theta}{\sin\theta_o} > 0$ for all time, so that the $\log s$ are always well behaved.

The case of $\theta_o = 0$ is obviously of interest, since then the orientation angle θ is steady. The case $\theta_o = \pi$ need not be examined directly due to symmetry. Taking the appropriate limits indicates that the vortex pair travels on a parabolic path:

$$\theta = 0 \tag{C.39}$$

$$R = R_o \tag{C.40}$$

$$X = \frac{\Gamma}{2\pi R_o}\alpha\frac{1}{2}t^2 + \alpha Y_o t + X_o \tag{C.41}$$

$$Y = \frac{\Gamma}{2\pi R_o}t + Y_o. \tag{C.42}$$

C.1.3 Vortex pair in simple strain of time dependent strength

In this case we take $\alpha = \beta = 0$ and with out loss of generality, we orient the axis relative to the strain such that $\phi = 0$. We assume that the strength of the strain γ is given by the derivative of a known time-dependent function $T(t)$ with $T(0) = 0$;

$$\gamma = \frac{dT}{dt} \tag{C.43}$$

The orientation and separation of the vortex pair are now given by

$$\tan\theta = \exp(-2T(t))\tan\theta_o \tag{C.44}$$

$$R^2 = R_o^2\left(\exp(2T(t))\cos^2\theta_o + \exp(-2T(t))\sin^2\theta_o\right). \tag{C.45}$$

Solving for the absolute location gives

$$X = \exp(T(t))X_o - \frac{\Gamma}{2\pi}\int_o^t \exp(T(t)-T(\tau))\frac{\sin\theta(\tau)}{R(\tau)}d\tau \tag{C.46}$$

$$Y = \exp(-T(t))Y_o + \frac{\Gamma}{2\pi}\int_o^t \exp(T(\tau)-T(t))\frac{\cos\theta(\tau)}{R(\tau)}d\tau. \tag{C.47}$$

For the particular case of a constant strain, $\gamma = const$, we find

$$\tan\theta = \exp(-2\gamma t)\tan\theta_o \tag{C.48}$$

$$R^2 = R_o^2\left(\exp(2\gamma t)\cos^2\theta_o + \exp(-2\gamma t)\sin^2\theta_o\right). \tag{C.49}$$

For this case the integrations for the location of the vortex pair may be done analytically;

$$X = \exp(\gamma t)X_o + \frac{\Gamma}{2\pi}\frac{\exp(\gamma t)}{4\gamma R_o\sin\theta_o}\log\left(\frac{1+\tan^2\theta_o\exp(-4\gamma t)}{1+\tan^2\theta_o}\right) \tag{C.50}$$

$$Y = \exp(-\gamma t)Y_o + \frac{\Gamma}{2\pi}\frac{\exp(-\gamma t)}{4\gamma R_o\cos\theta_o}\log\left(\cos^2\theta_o\exp(4\gamma t) + \sin^2\theta_o\right). \tag{C.51}$$

Appendix D Hamiltonian formulation for patches in shear

We briefly present the Hamiltonian for elliptic vortex patches in a background flow with constant vorticity ω_∞. The inclusion of the background vorticity is an extension of the work of Melander, Zabusky, and Styczek [14]. This generalization has been done independently, by Ngan, Meacham, and Morrison [26] who also assume,as we do, that the Hamiltonian for vortex patches can be identified with the finite part of the kinetic energy of the system. We show that the equations arrived at by this assumption are consistent with the elliptical model we developed from first principles in Chapter Four.

We assume that the flow is composed of a background linear shear producing a constant vorticity ω_∞ and a collection of vortex patches each with vorticity $(\omega_i + \omega_\infty)$ and occupying a region A_i. We decompose the streamfunction representing such a flow into a time independent background flow which describes the shear, ψ_B, and time-dependent functions, ψ_i which represent the flow induced by each patch:

$$\psi(x,y,t) = \omega_\infty \psi_B(x,y) + \sum_i \omega_i \psi_i(x,y,t) \tag{D.1}$$

where

$$\nabla^2 \psi_B = -1 \text{ everywhere} \tag{D.2}$$

$$\nabla^2 \psi_i = -1 \text{ in } A_i \tag{D.3}$$

and ψ_i is irrotational outside of the region A_i.

Due to the flux of fluid at infinity, the Kinetic Energy for such a flow is infinite. We choose to subtract the time-independent energy of the background shear to give, H, the finite part of the kinetic energy. H may be computed by an application of

Green's formula as

$$H = \frac{1}{2}\int (\nabla\psi)^2\, dA - \frac{1}{2}\int (\nabla\psi_B)^2\, dA \tag{D.4}$$

$$= \frac{1}{2}\sum_i \left(\omega_i^2 \int \psi_i dA_i\right) + \frac{1}{2}\sum_i \sum_{j\neq i} \left(\omega_i\omega_j \int \psi_i dA_j\right) \tag{D.5}$$

$$+ \sum_i \left(\omega_i\omega_\infty \int \psi_B dA_i\right), \tag{D.6}$$

where it has been assumed that

$$\lim_{R\to\infty} \oint_{|x|=R} \psi_b \frac{\partial\psi_i}{\partial n} dl = 0. \tag{D.7}$$

The first sum is the self induced energy of the patches, the second term represents the mutual energy of the interaction of patches, and the third sum give the energy of interaction between the steady background flow and patches. Previous presentations of the Hamiltonian for vortex patches in a steady irrotational background flow with flux at infinity required an appeal to the reciprocal theorems for harmonic fields in the introduction of the third term. As this Hamiltonian has been independently produced by Nga, Meacham, and Morrision [26], we choose not to concern ourself by the introduction of Poisson brackets for H. Instead we approximate this function to create a simple analytic Hamiltonian for elliptically shaped vortex patches interacting in a background shear flow, and we then use direct differentiation to demonstrate the Hamiltonian structure.

The streamfunction, ψ_i, for a vortex patch of unit strength in the region A_i can be computed as

$$\psi_i = -\frac{1}{2\pi}\int \log\left|\mathbf{r} - \mathbf{r}'\right| dA_i'. \tag{D.8}$$

For the case of linear shear plus a constant translational velocity, the contribution from background flow is given by

$$\psi_B = -\frac{1}{2}y^2 + \frac{V_\infty}{\omega_\infty}x. \tag{D.9}$$

Assuming the patches are elliptical with aspect ratios λ_i, the self-induced energy term, H_S, and the energy from the interaction with the background, H_B, can be evaluated exactly since

$$H_S = \frac{1}{2}\sum_i \left(\omega_i^2 \int \psi_i dA_i\right) \tag{D.10}$$

$$= \frac{1}{2}\sum_i \left(-\frac{\omega_i^2}{2\pi}\int\int \log\left|\mathbf{r}-\mathbf{r}'\right| dA_i' dA_i\right) \tag{D.11}$$

$$= \frac{1}{2}\sum_i \left(\frac{-\omega_i^2 |A_i|^2}{4\pi}\left[\log\frac{(\lambda_i+1)^2}{\lambda_i} + \log\frac{|A_i|}{4\pi} + \frac{1}{4}\right]\right) \tag{D.12}$$

and

$$H_B = \sum_i \left(\omega_i\omega_\infty \int \psi_B dA_i\right) \tag{D.13}$$

$$= -\sum_i \left(\omega_i\omega_\infty \int \frac{1}{2}y^2 dA_i\right) + \sum_i \left(\omega_i V_\infty \int x dA_i\right) \tag{D.14}$$

$$= -\frac{\omega_\infty}{2}\sum_i \omega_i \left(\frac{|A_i|^2}{4\pi\lambda_i}\left(\lambda_i^2 + \left(1-\lambda_i^2\right)\cos^2\phi_i\right) + |A_i| Y_i^2\right) \tag{D.15}$$

$$+\sum_i \omega_i V_\infty |A_i| X_i. \tag{D.16}$$

Where the centroid of the patch is found at (X_i, Y_i) and $|A_i|$ gives its area; ϕ_i is the orientation angle.

To calculate the interaction energy, H_I,

$$H_I = -\frac{1}{4\pi}\sum_i\sum_{j\neq i} \omega_i\omega_j \int\int \log\left|\mathbf{r}-\mathbf{r}'\right| dA_i dA_j' \tag{D.17}$$

we write

$$\log\left|\mathbf{r}-\mathbf{r}'\right| = \log\left|\mathbf{R}_i - \mathbf{R}_j + (\mathbf{r}-\mathbf{R}_i) - \left(\mathbf{r}'-\mathbf{R}_j\right)\right| \tag{D.18}$$

and assume the characteristic lengths of the patches are small compared with the separation distances between the patches, allows us to replace the logarithmic term by a linear Taylor series. Under this approximation, equivalent to truncating a moment

expansion of the energy, H_I takes the form

$$H_I = -\frac{1}{4\pi}\sum_i\sum_{j\neq i}\omega_i\omega_j\left|A_i\right|\left|A_j\right|\left[\log R_{i,j} - \frac{A_i}{4\pi R_{i,j}^2}\frac{\lambda_i^2-1}{\lambda_i}\cos 2\left(\phi_i-\theta_{i,j}\right)\right] \quad \text{(D.19)}$$

where the vector between centroids defines $R_{i,j}$ and $\theta_{i,j}$ by

$$\left(X_i - X_j, Y_i - Y_j\right) = R_{i,j}\left(\cos\theta_{i,j}, \sin\theta_{i,j}\right). \quad \text{(D.20)}$$

To demonstrate the Hamiltonian nature of $H = H_S + H_I + H_B$, direct differentiation and comparison with the equations of evolution for derived in Chapter 5, shows that

$$\frac{\partial H}{\partial X_i} = -\omega_i\left|A_i\right|\frac{dY_i}{dt} \quad \text{(D.21)}$$

$$\frac{\partial H}{\partial Y_i} = \omega_i\left|A_i\right|\frac{dX_i}{dt} \quad \text{(D.22)}$$

$$\frac{\partial H}{\partial \lambda_i} = \frac{\left|A_i\right|^2\omega_i\left(1-\lambda_i^2\right)}{8\pi\lambda_i^2}\frac{d\phi_i}{dt} \quad \text{(D.23)}$$

$$\frac{\partial H}{\partial \phi_i} = -\frac{\left|A_i\right|^2\omega_i\left(1-\lambda_i^2\right)}{8\pi\lambda_i^2}\frac{d\lambda_i}{dt}. \quad \text{(D.24)}$$

These equations may be put in canonical Hamiltonian form by defining the variables as

$$q_i = -\frac{\left|A_i\right|^2\omega_i\left(1+\lambda_i^2\right)}{8\pi\lambda_i} \quad \text{(D.25)}$$

$$p_i = \phi_i \quad \text{(D.26)}$$

$$\hat{X}_i = \sqrt{\omega_i\left|A_i\right|}X_i \quad \text{(D.27)}$$

$$\hat{Y}_i = \sqrt{\omega_i\left|A_i\right|}Y_i. \quad \text{(D.28)}$$

Appendix E Howard Semicircle Theorem

The Howard Semicircle theorem for perturbations to two fluid parallel flow with surface tension at interface (Rayleigh equation with our boundary conditions): Given

$$U_{\min} = \min_y U(y) \text{ and } U_{\max} = \max_y U(y) \tag{E.1}$$

f $\Re(c) > U_{\max}$ or $\Re(c) < U_{\min}$ then $\Im(c) = 0$. Furthermore if $\Im(c) \neq 0$ and $\kappa^2 T + g(\rho_w - \rho_a) \geq 0$ then

$$\left| c - \frac{1}{2}(U_{\max} + U_{\min}) \right|^2 \leq \frac{1}{4}(U_{\max} - U_{\min})^2 . \tag{E.2}$$

Proof with addition of surface tension T : Fist we change to a new dependent variable

$$F(y) = \frac{\phi}{W} \tag{E.3}$$

where $W = U - c$. Rayleigh equation becomes

$$\left(W^2 F'\right)' - \kappa^2 W^2 F = 0 \tag{E.4}$$

and the jump at $y = 0$ is

$$\left(W^2 F'\right)' - \kappa^2 W^2 F = 0. \tag{E.5}$$

Multiplying (E.4) by $\rho_w F^*$ and integrating the water,

$$\rho_w \left\{ \left(W^2 F'\right) F^*|_{y=0} - \int_{-\infty}^{0} W^2 \left|F'\right|^2 dy - \kappa^2 \int_{-\infty}^{0} W^2 |F|^2 dy \right\} = 0. \tag{E.6}$$

Likewise, multiplying by $\rho_a F^*$ and integrating the air

$$\rho_a \left\{ \left(W^2 F'\right) F^*|_{y=0} - \int_{0}^{\infty} W^2 \left|F'\right|^2 dy - \kappa^2 \int_{0}^{\infty} W^2 |F|^2 dy \right\} = 0. \tag{E.7}$$

Adding (E.6) and (E.7) and appluing the boundary condition (E.5) gives

$$\left(\rho_w \int_{-\infty}^{0} dy + \rho_a \int_{0}^{\infty} dy\right) \left[W^2 Q\right] = |F(0)|^2 \left(\kappa^2 T + g\left(\rho_w - \rho_a\right)\right) \tag{E.8}$$

where

$$Q = \left|F'\right|^2 + \kappa^2 |F|^2 . \tag{E.9}$$

Say $c = c_r + ic_i$; the $\Im\left[(E.8)\right]$ gives

$$c_i \left(\rho_w \int_{-\infty}^{0} (U - c_r) Q dy + \rho_a \int_{0}^{\infty} (U - c_r) Q dy\right) = 0. \tag{E.10}$$

$$\longrightarrow c_i = 0 \text{ if } c_r \text{ isn't in the range of } U(y) \ . \tag{E.11}$$

If $c_i \neq 0$; $2c_r/c_i$, we see that $\Im\left[(E.8)\right] + \Re\left[(E.8)\right]$ becomes

$$\left(\rho_w \int_{-\infty}^{0} dy + \rho_a \int_{0}^{\infty} dy\right) \left(U^2 - c_r^2 - c_i^2\right) Q = |F(0)|^2 \left(\kappa^2 T + g\left(\rho_w - \rho_a\right)\right); \tag{E.12}$$

using the inequality $(U - U_{\min})(U - U_{\max}) Q \leq 0$ and the relation (E.10) we find

$$A \left(\rho_w \int_{-\infty}^{0} Q dy + \rho_a \int_{0}^{\infty} Q dy\right) \geq |F(0)|^2 \left(\kappa^2 T + g\left(\rho_w - \rho_a\right)\right) \tag{E.13}$$

with $A = \left(\left(U_{\max} + U_{\min}\right) c_r - c_r^2 - c_i^2 - U_{\max} U_{\min}\right)$. For those wavenumbers, κ, such that $\kappa^2 T + g\left(\rho_w - \rho_a\right) \geq 0$ we see that

$$\left(U_{\max} + U_{\min}\right) c_r - c_r^2 - c_i^2 - U_{\max} U_{\min} > 0, \tag{E.14}$$

or equivalently

$$\left|c - \frac{1}{2}\left(U_{\max} + U_{\min}\right)\right|^2 \leq \frac{1}{4}\left(U_{\max} - U_{\min}\right)^2 . \tag{E.15}$$

Appendix F Stability region for two simple profiles

F.1 Stability regions for wind only

In this section we identify stability boundaries for infinitesimal perturbations to a flow which represents a smooth parallel wind profile blowing over still water. By choosing $U_w = 0$, the velocity profile (5.18) becomes

$$U(y) = U_a \left(1 - \exp\left[-2y/\Delta_a\right]\right) H(y). \tag{F.1}$$

The implicit dispersion relation (5.24) simplifies somewhat to give

$$\frac{2}{\kappa\Delta_a} U_a s + \frac{1}{c}\left(g\frac{1-s}{\kappa} + \kappa\frac{T}{\rho_w}\right) = c\left(1 + s + s\frac{2}{\kappa\Delta_a} Z_1 \frac{F_a'(Z_1)}{F_a(Z_1)}\right), \tag{F.2}$$

with $Z_1 = U_a/(U_a - c)$.

By the Howard semicircle theorem, we know that if a infinitesimal wave with wavenumber κ and wavespeed $c(\kappa)$ is unstable then $0 < \Re(c(\kappa)) < U_a$. Sketching the curve defined by $c(\kappa)$ in the complex c-plane, see Figure $F.1$, we note that the slowest right-traveling waves become unstable immediately upon entering the semicircle at the point U_a. To identify the stability boundaries we shall obtain the wavenumbers at which the right-traveling wavespeed enters and leaves the semicircle. These two wavenumbers will define a range; those right-traveling waves with wavenumbers in this range will be unstable. We point out that the left-traveling waves are always stable. It is a simple matter to show from equation (F.2) that the left-traveling waves do not enter the semicircle. Taking the limit $c \to 0$ one finds κ is defined by $\kappa^2 = -g(1-s)\rho_w/T$ and this implies imaginary wavenumbers as $s = \rho_a/\rho_w$ is less than one.

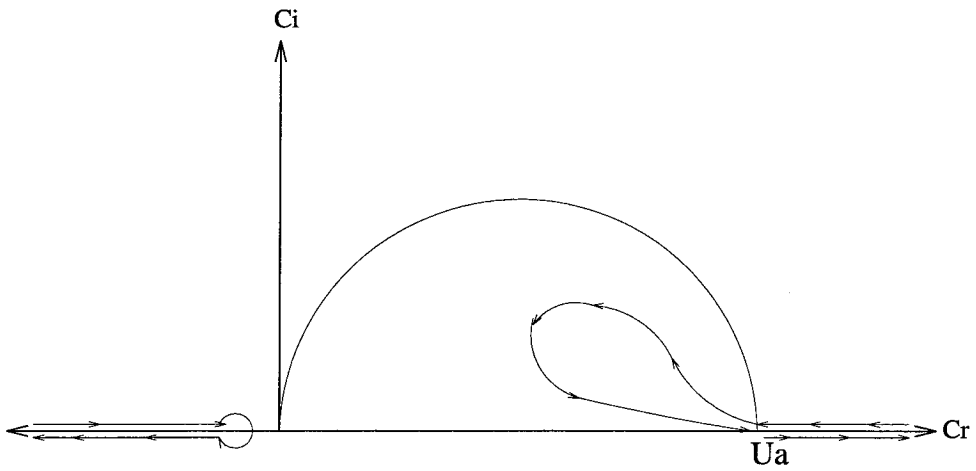

Figure F.1: Sketch of the compex wave speed $c(\kappa)$ for the case of wind only entering and exiting the Howard semicircle.

In order to find the entry and exit κ for the right-traveling waves, we set $c = U_a$. For this choice of wavespeed, the form of the function ϕ simplifies;

$$\phi = \left\{ \begin{array}{ll} \exp\left(-\sqrt{\kappa^2 + 4/\Delta_a^2}\, y\right) & y > 0 \\ \exp\left(\kappa y\right) & y < 0 \end{array} \right\} . \tag{F.3}$$

The dispersion relation which now defines the wavenumbers of the right-traveling waves which travel at speed U_a takes the form

$$U_a s \left(\frac{2}{\kappa \Delta_a} - \sqrt{\left(\frac{2}{\kappa \Delta_a}\right)^2 + 1} \right) + \frac{1}{U_a} \left(g \frac{1-s}{\kappa} + \kappa \frac{T}{\rho_w} \right) = U_a. \tag{F.4}$$

We choose to non-dimensionalize with respect to the physically relevant minimum wavespeed $U_{\min}$ and wavenumber $\kappa_{\min}$ of the gravity-capillary dispersion relation (5.25), see equations (5.26) and (5.27) . Under this nondimesionalization, say $U_a \to U, \kappa \to k$, and $\Delta_a \to d_a$. The interface condition (F.4) is now written as

$$s\sqrt{k^2 + 4/d_a^2} = 2s/d_a - k + \frac{(1+s)}{2U^2}\left(1 + k^2\right) \tag{F.5}$$

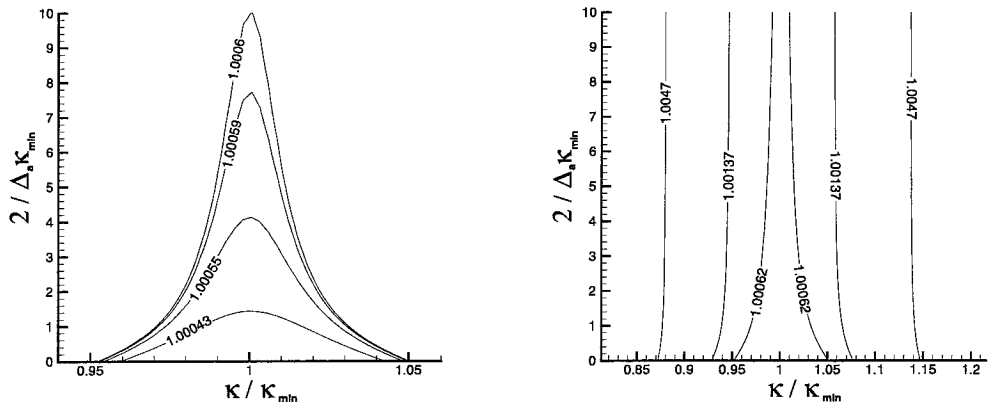

(a) $(1+s) > U^2 > 1$ (b) $U^2 > 1+s$

Figure F.2: Stability boundaries $a(k)$ labeled by nondimensional windspeed $U = U_a/U_{min}$. These curves correspond to waves which travel at the wind speed, $c = U_a$

or solving for d

$$d_a(k) = \frac{8sU^2(1+s+k^2(1+s)-2kU^2)}{(1+s)(2kU^2-1-k^2)(1+s+k^2(1+s)+2kU^2(s-1))}. \tag{F.6}$$

For fixed values of $U = U_a/U_{\min}$ equation (F.6) produces a curve in the (k, d_a) plane. By our definitions of the profile and wavenumber, the region of physical interest is $k, d_a > 0$.

For values of $U^2 < 1$ all perturbations are stable as the equation (F.6) does not admit solutions with positive k, d_a. Thus we need the wind speed U_a to exceed the minimum speed of an infinitesimal gravity-capillary for instability to occur. For values of $U > 1$ there exist unstable wavenumbers. Notice that the neutral curve $d_a(k)$ defined by (F.6) limits to infinity at the points

$$k_1^{\pm} = U^2 \pm \sqrt{U^4 - 1}; \tag{F.7}$$

this corresponds to the fact that at these wavenumbers gravity-capillary waves are traveling at the speed U. To simplify graphing we choose to plot $a(k) \equiv 2/d(\kappa)$.

For values of the nondimensional wind speed U such that $(1+s) > U^2 > 1$, the

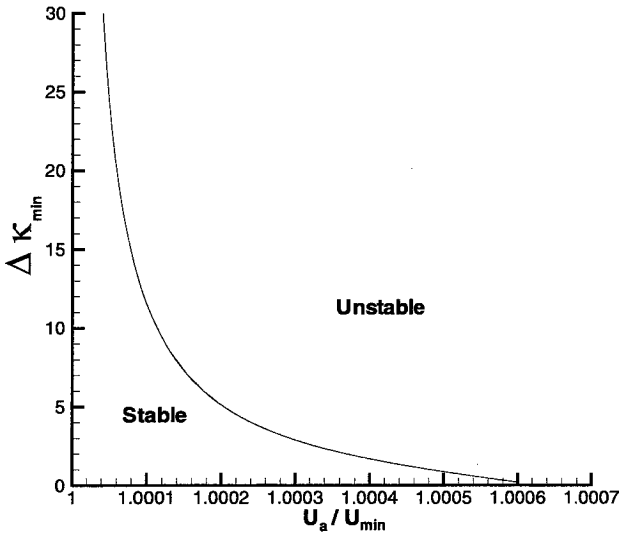

Figure F.3: Stability boundary in the $(U, \Delta k)$ plane for wind only.

curve $a(k)$ which separates the stable and unstable regions has a finite maximum, see Figure F.2 (a). The area beneath the curve for a given U is unstable. This indicates that if a wind layer is thin enough, i.e., $a = 2/(\Delta_a \kappa_{\min})$ above the curve, all wavenumbers are stable. But for higher winds speeds,$U^2 > (1+s)$, the $a(k)$ curve asymptotes to infinity for the wavenumbers

$$k_2^{\pm} = \frac{\left(U^2 \pm \sqrt{U^4 - (1+s)^2}\right)}{1+s}. \tag{F.8}$$

This result maybe anticipated, as we have shown in the limit $a \to \infty$ $(d \to 0)$ with finite k the Kelvin-Helmholtz dispersion relation is reclaimed. It is necessary that $U^2 > (1+s)$ for a Kelvin-Helmholtz wave to travel at a speed less than U and the points $k_2^{\pm}$ are the wavenumbers at which the Kelvin-Helmholtz wavespeed enters and leaves the Howard semicircle. In Figure F.2 (b) we see that the curve $a(k)$ in the (k, a) plane connects the point $(k_1^-, 0)$ to the limit (k_2^-, ∞) and (k_2^+, ∞) to $(k_1^+, 0)$. Thus when $U^2 > (1+s)$ we see that for any given inverse layer thickness a there exists a unstable wavenumbers.

By calculating the maximum of $a(k)$ as a function of the wind speed U, a curve

can be drawn in the space of wind speed vs. layer thickness. Such a curve is shown in Figure F.3. This curve separates the region in which any perturbation is stable from that in which there exist unstable wavenumbers. It is interesting to note that in the transitional area of $(1+s) > U^2 > 1$, an increase in layer thickness destabilizes the flow.

F.2 Stability regions for drift layer only

In this section we assume that wind is traveling parallel to the flat surface of the water at a uniform constant velocity equal to the velocity of the water at the interface. We choose a velocity profile in the water which resembles a drift layer, perhaps initially caused by wind induced stress and we perturb the flow to study waves generated by the drift layer. In a frame of reference in which the undisturbed interface is stationary, the velocity profile $\mathbf{u} = (U(y), 0)$ is taken to be of the simple form

$$U(y) = H(-y)\, U_w \left(\exp\left(2y/\Delta_w\right) - 1\right) \tag{F.9}$$

with $\Delta_w > 0$. The wavespeeds c for infinitesimal perturbations to the interface of the form $\eta(x,t) = \exp(i\kappa(x-ct))$ may be obtained from a simplified form of the implicit dispersion relation (5.24);

$$-\frac{2}{\kappa\Delta_w}U_w + \frac{1}{c}\left(g\frac{1-s}{\kappa} + \kappa\frac{T}{\rho_w}\right) = c\left(1+s+\frac{2}{\kappa\Delta_w}Z_2\frac{F_w'(Z_2)}{F_w(Z_2)}\right) \tag{F.10}$$

where $Z_2 = U_w/(U_w + c)$. We will not actually use equation (F.10) to calculate the wavespeeds, but instead we will determine stability regions from a simpler equation. But we note that the implicit dispersion relation implies that the wavespeed $c = 0$ can not be obtained by real valued wavenumbers when $1 > s = \rho_a/\rho_w$.

An application of the Howard semicircle theorem tells us that $-U_w < \Re(c(\kappa)) < 0$ for unstable waves. Sketching the curve defined by $c(\kappa)$ in the complex c-plane, Figure F.4, we see that the slowest left-traveling waves become unstable immediately upon entering the semicircle at the point $-U_w$. Stability boundaries are obtained from the

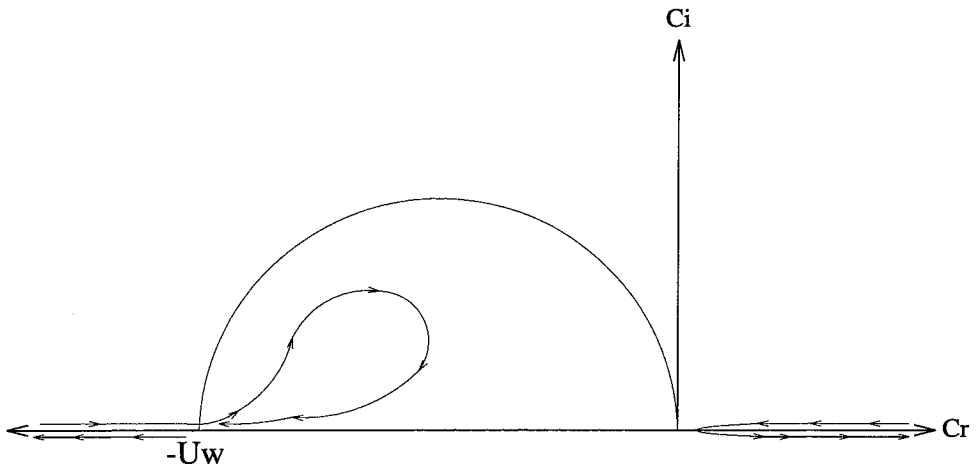

Figure F.4: Sketch of the compex wave speed $c(\kappa)$ for the case of a drift layer only entering and exiting the Howard semicircle.

wavenumbers at which the left-traveling wavespeed enters and leaves the semicircle. These wavenumbers will define a range; those left-traveling waves with wavenumbers in this range will be unstable. The right-traveling waves are always stable: It would be necessary for the dispersion relation to pass thru the origin, but as we mentioned earlier c cannot equal zero for real wavenumber κ.

Setting $c = -U_w$ we calculate the wavenumbers κ associated with entering and exiting the semicircle. For this choice of wavespeed, the form of the function ϕ simplifies;

$$\phi = \left\{ \begin{array}{ll} \exp\left(-\kappa y\right) & y > 0 \\ \exp\left(\sqrt{\kappa^2 + 4/\Delta_w^2}\, y\right) & y < 0 \end{array} \right\}. \tag{F.11}$$

We find from the dispersion relation (F.10) that the wavenumbers for left-traveling perturbations with speed $-U_w$ are defined by the equation

$$U_w \left(\frac{2}{\kappa \Delta_w} - \sqrt{\left(\frac{2}{\kappa \Delta_w}\right)^2 + 1} \right) + \frac{1}{U_w} \left(g \frac{1-s}{\kappa} + \kappa \frac{T}{\rho_w} \right) = s U_w \kappa. \tag{F.12}$$

Nondimensionalizing with respect to the minimum waves speed $U_{\min}$, (5.26), of a gravity-capillary wave and its corresponding wavenumber $\kappa_{\min}$, (5.27); we say $U_w \rightarrow$

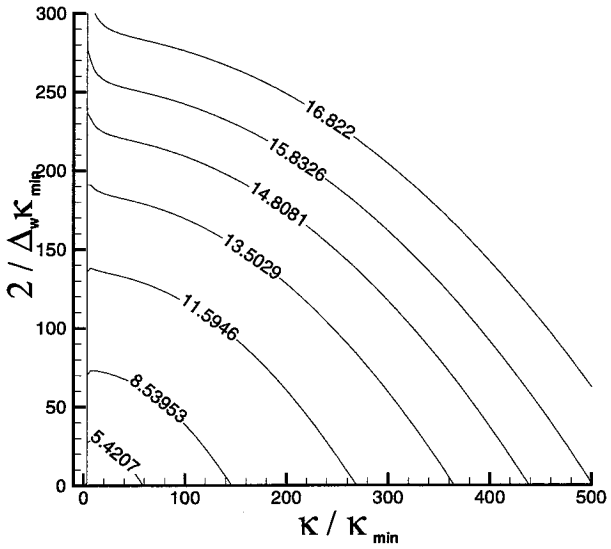

Figure F.5: Stability boundaries $b(k)$ labeled by nondimensional drift layer speed $U = U_w/U_{min}$. These curves correspond to waves which travel at the drift layer speed, $c = U_a$

$U, \kappa \to k$, and $\Delta_w \to d_w$. The interface condition (F.10) may now be expressed as

$$\sqrt{k^2 + 4/d_w^2} = 2/d_w - sk + \frac{(1+s)}{2U^2}\left(1 + k^2\right), \tag{F.13}$$

or solving for the inverse the drift layer thickness

$$d_w = \frac{8U^2\left(1 + s + k^2\left(1 + s\right) - 2ksU^2\right)}{\left(1 + s\right)\left(2kU^2 - 1 - k^2\right)\left(1 + s + k^2\left(1 + s\right) + 2k\left(1 - s\right)U^2\right)}. \tag{F.14}$$

All perturbations are stable when $U^2 < 1$ as in this case d_w calculated by equation (F.14) is negative for all positive k. This implies that the curve $c\left(\kappa\right)$ does not enter the unstable semicircle. The velocity which defines the drift layer speed must to exceed, in absolute value, the minimum speed of an infinitesimal gravity-capillary for instability to occur. For values of $U^2 > 1$ there exist unstable wavenumbers. We find the curve $d_w\left(k\right)$ limit to infinity at the points

$$k_1^{\pm} = U^2 \pm \sqrt{U^4 - 1}; \tag{F.15}$$

at these wavenumbers gravity-capillary waves are traveling at the speed U. We define $b = 2/d_w$ and make a series of plots to investigate the unstable region. In Figure $F.5$ we have fixed values of $U = U_w/U_{\min}$ and used equation (F.14) to produce a curve in the (k, b) plane.

For values of the nondimensional wind speed U such that $(1 + 1/s) > U^2 > 1$, the curve $b(k)$ which separates the stable and unstable regions has a finite maximum, examples of which can be seen in Figure $F.5$. This indicates that for drift speeds in this range all wavenumbers will be stable if the drift layer is thin enough. This is a rather large range as $\sqrt{1 + 1/s} \simeq 28.189$.

For higher drift speeds, i.e. $U^2 > (1 + 1/s)$, the $b(k)$ curve asymptotes to infinity for the wavenumbers

$$k_2^{\pm} = \frac{\left(U^2 \pm \sqrt{U^4 - (1 + 1/s)^2}\right)}{1 + 1/s}. \tag{F.16}$$

The Kelvin-Helmholtz dispersion relation is reclaimed in the limit $b \to \infty$ $(d_w \to 0)$ with finite k. Setting U_a to zero in the Kelvin-Helmholtz dispersion relation (5.31) one finds that it is necessary that $U^2 = (U_w/U_{\min})^2 > (1 + 1/s)$ for a Kelvin-Helmholtz wave to travel at speeds in the range $\{-U_w, 0\}$, and one also discovers that the points $k_2^{\pm}$ are the wavenumbers at which the Kelvin-Helmholtz wavespeed enters and exits the Howard semicircle. The curve $b(k)$ in the (k, b) plane connects the point $(k_1^-, 0)$ to the limit (k_2^-, ∞) and (k_2^+, ∞) to $(k_1^+, 0)$. When $U^2 > (1 + 1/s)$ we see that for any given inverse layer thickness b there exists a unstable wavenumbers.

By calculating the maximum of $b(k)$ as a function of the drift speed U, a curve can be drawn in the space of drift speed vs. layer thickness. Such a curve is shown in Figure $F.6$. This curve separates the region in which any perturbation is stable from that in which there exist unstable wavenumbers. As we found in the previous section, an increase in the layer thickness may destabilize a flow.

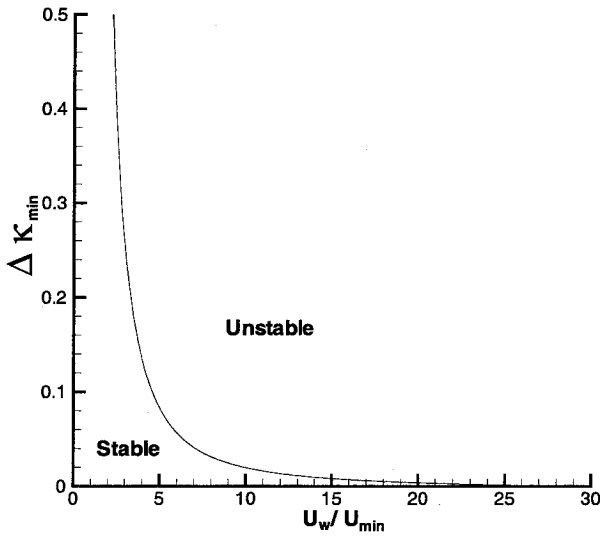

Figure F.6: Stability boundary in the $(U, \Delta k)$ plane for a drift layer only.

Appendix G A variational principle for a bubble in potential flow

Luke [10] presented a variational formulation for gravity waves. Luke describes a least action principle in which the pressure serves as the Lagrangian density and an elimination of the first variation results in the equations of motion for irrotational waves in the absence of surface tension. In this section we alter the geometry to that of two-dimensional bubbles in potential flow and make the addition of surface tension at the bubble interface. By considering the potential energy stored in both the interface and the pressure field as the "action," we are able to obtain the complete equations of evolution.

For our two-dimensional bubble, the time dependent interface is defined in polar co-ordinates as

$$r = R(\theta, t). \tag{G.1}$$

Starting with the Euler equation,

$$\nabla\left(\varphi_t + \frac{1}{2}(\nabla\varphi)^2 + f\right) = -\frac{1}{\rho}\nabla P, \tag{G.2}$$

we integrate along some arc from the bubble surface to a point in the fluid

$$P = -\rho\left[\varphi_t + \frac{1}{2}(\nabla\varphi)^2 + f\right] + \rho\Omega \tag{G.3}$$

where $\Omega \equiv \varphi_t + \frac{1}{2}(\nabla\varphi)^2 + f + P$ evaluated on the surface of the bubble. Setting density equal to one, define

$$\pounds = \int_0^{2\pi}\left[\int_\infty^R\left[\varphi_t + \frac{1}{2}(\nabla\varphi)^2 + f\right] r\, dr + T\sqrt{\left(\frac{\partial R}{\partial\theta}\right)^2 + R^2}\right] d\theta \tag{G.4}$$

where f is the body force and T is the surface tension. Notice that the square root is just an infinitesimal length element of the interface; the product with T represents the potential energy stored in an element of the interface via the tension. We will be interested in the variations of I , where

$$I = \int_{t_1}^{t_2} \pounds \; dt. \tag{G.5}$$

Physically $\pounds$ is the total potential energy stored in the pressure field and stored in the interface. The total first variation of I is

$$\begin{aligned} \delta I \;\; = \;\; & \int_{t_1}^{t_2} \int_0^{2\pi} \left[\varphi_t + \frac{1}{2} \left(\nabla \varphi \right)^2 + f + T \frac{R^2 + 2R_\theta^2 - R_{\theta\theta}}{\left(R_\theta^2 + R^2 \right)^{3/2}} \right] R \; \delta R \; d\theta \; dt \\ & + \int_{t_1}^{t_2} \int \int \delta \varphi_t \; dA \; dt + \int_{t_1}^{t_2} \int \int \nabla \delta \varphi \cdot \nabla \varphi \; dA \; dt \end{aligned} \tag{G.6}$$

where the term in braces on the first line is evaluated at the interface. We recognize that

$$\kappa = \frac{R^2 + 2R_\theta^2 - R_{\theta\theta}}{\left(R_\theta^2 + R^2 \right)^{3/2}} \tag{G.7}$$

gives the curvature.

After an application of Green's formula, the variation of the stored energy becomes;

$$\begin{aligned} \delta I \;\; = \;\; & \int_{t_1}^{t_2} \int_0^{2\pi} \left[\varphi_t + \frac{1}{2} \left(\nabla \varphi \right)^2 + f + T\kappa \right] R \; \delta R \; d\theta \; dt \\ & + \int_{t_1}^{t_2} \frac{d}{dt} \int \int \delta \varphi \; dA \; dt \\ & - \int_{t_1}^{t_2} \int \int \delta \varphi \nabla^2 \varphi \; dA \; dt \\ & + \int_{t_1}^{t_2} \int_0^{2\pi} \left[\frac{\partial \varphi}{\partial n} - \frac{\partial R}{\partial t} \right] R \; \delta \varphi \; d\theta \; dt \\ & - \lim_{r \to \infty} \int_{t_1}^{t_2} \int_0^{2\pi} \left[\frac{\partial \varphi}{\partial n} \right] r \; \delta \varphi \; d\theta \; dt \end{aligned} \tag{G.8}$$

we admit variations such that $\int \int \delta \varphi \; dA = 0$ at the two times t_1, t_2.

Of course we are now interested in $\delta I = 0$. The independent variation of the bubble interface, δR, gives us Bernoulli's equation on the interface

$$\varphi_t + \frac{1}{2}(\nabla\varphi)^2 + f + T\kappa = 0 \tag{G.9}$$

while variations of the potential imply incompressibility

$$\nabla^2\varphi = 0, \tag{G.10}$$

and the kinematic boundary condition

$$\frac{\partial\varphi}{\partial n} = \frac{\partial R}{\partial t}. \tag{G.11}$$

Restricting ourselves to variations which don't effect a prescribed flow at infinity, implies $\lim_{r\to\infty}\int_{t_1}^{t_2}\int_0^{2\pi}\left[\frac{\partial\varphi}{\partial n}\right] r\ \delta\varphi\ d\theta\ dt = 0$.

Bibliography

[1] G.K. Batchelor. *An Introduction to Fluid Dynamics.* Cambridge University Press, first edition, 1967.

[2] E.A. Caponi, M.Z. Caponi, P.G. Saffman, and H.C. Yuen. A simple model for the effect of water shear on the generation of waves by wind. *Proc. R. Soc. Lond. A.*, 438:95–101, 1992.

[3] S.C. Crow. Stability theory for a pair of trailing vortices. *AIAA Journal*, 8(12):2172–2179, 1970.

[4] T.W.G. deLaat and R. Coene. Two-dimensional vortex motion in the cross-flow of a wing-body configuration. *J. Fluid Mech.*, 305:93–109, 1995.

[5] L. Foppl. Wirbelbewegung hinter einem kreiszylinder. *Sitz. K. Bayer Akad. Wiss.*, 1:1–18, January-March 1913. (Also: 1983. Vortex motion behind a circular cylinder. N.A.S.A T.M. 77015.).

[6] S.P. Kang. *work in progress.* Ph.D. dissertation, CalTech, 1998.

[7] E. Kelley and M.M. Wu. Path instabilities of rising air bubbles in a Hele-Shaw cell. *Physical Review Letters*, 79:1265–1268, 1997.

[8] S. Kida. Motion of an elliptic vortex in a uniform shear flow. *Journal of the Physical Society of Japan*, 50(10):3517–3520, 1981.

[9] M.F. Lough. On the motion and stability of a vortex ring in a pipe. (Also found in M. Lough's Ph.D. thesis), Sept 1992.

[10] J.C. Luke. A variational principle for a fluid with a free surface. *J. Fluid Mech*, 27:395–397, 1967.

[11] E.B. McLeod. The explicit solution of a free boundary problem involving surface tension. *J. Rat. Mech. Anal.*, 4:557–, 1955.

[12] D.I. Meiron. On the stability of gas bubbles rising in an inviscid fluid. *J. Fluid Mech*, 198:101–, 1989.

[13] D.I. Meiron, P.G. Saffman, and J.C. Schatzman. The linear two-dimensional stability of inviscid vortex streets of finite-cored vortices. *J. Fluid Mech.*, 147:187–212, 1984.

[14] M.V. Melander, N.J. Zabusky, and A.S. Styczek. A moment model for vortex interaction of the two-dimensional Euler equations, Part I., Computational validation of a Hamiltonian elliptical representation. *J. Fluid Mech*, 167:95–115, 1986.

[15] V.V. Meleshko and G.J.F. vanHeijst. On Chaplygin's investigations of two-dimensional vortex structures in an inviscid fluid. *J. Fluid Mech.*, 272:157–182, 1994.

[16] J.W. Miles. On the generation of surface waves by shear flow. *J. Fluid Mech*, 3:2185–204, 1957.

[17] L.M. Milne-Thomson. *Theoretical Hydrodynamics.* The Macmillan Company, fourth edition, 1960.

[18] D.W. Moore. The rise of a gas bubble in a viscous liquid. *J. Fluid Mech.*, 6:113–, 1959.

[19] D.W. Moore. The velocity of rise of distorted gas bubbles in a liquid of small viscosity. *J. Fluid Mech.*, 23:749–, 1965.

[20] D.W. Moore and P.G. Saffman. Stucture of a line vortex in an imposed strain. In Olsen, Goldburg, and Rogers, editors, *Aircraft wake turbulence*, pages 339–354. Plenum, 1971.

[21] D.W. Moore and P.G. Saffman. The motion of a vortex filament with axial flow. *Phil. Trans. Roy Soc.*, A272:403–, 1972.

[22] D.W. Moore and P.G. Saffman. The instability of a straight vortex filament in a strain field. *Proc. R. Soc. Lond. A.*, 346:413–425, 1975.

[23] L.C. Morland and P.G. Saffman. Effect of wind profile on the instability of wind blowing over water. *J. Fluid Mech.*, 252:383–398, 1993.

[24] L.C. Morland, P.G. Saffman, and H.C. Yuen. Waves generated by shear layer instabilities. *Proc. R. Soc. Lond. A*, 433:441–450, 1991.

[25] R. Natarajan and A. Acrivos. The instability of the steady flow past spheres and disks. *J. Fluid Mech.*, 254:323–344, 1993.

[26] K. Ngan, S. Meacham, and P.J. Morrison. Elliptical vortices in shear: Hamiltonian moment formulation and Melnikov analysis. *Phys. Fluids*, 8(4):896–913, 1996.

[27] Q. Nie and S. Tanveer. The stability of a two-dimensional rising bubble. *Phys. Fluids*, 7(6):1292–1306, 1995.

[28] G. Pedrizzetti and E.A. Novikov. Instability and chaos in axisymmetric vortex-body interactions. *Fluid Dynamics Research*, 12:129–151, 1993.

[29] G. Ryskin and L.G. Leal. Numerical solution of free-boundary problems in fluid mechanics. Part 1. The finite-difference technique. *J. Fluid Mech.*, 148:1–17, 1984.

[30] G. Ryskin and L.G. Leal. Numerical solution of free-boundary problems in fluid mechanics. Part 2. Bouyancy-driven motion of a gas bubble through a quiescent liquid. *J. Fluid Mech.*, 148:19–35, 1984.

[31] P.G. Saffman. On the rise of small air bubbles in water. *J. Fluid Mech*, 1:249–, 1956.

[32] P.G. Saffman. *Vortex Dynamics.* Cambridge Monographs on Mechanics and Applied Mathematics. Cambridge University Press, second edition, 1992.

[33] P.N. Shankar. On the shape of a two-dimensional bubble in uniform motion. *J. Fluid Mech*, 244:287–, 1992.

[34] S. Shirayama. Flow past a sphere: Topological transitions of the vorticity field. *AIAA Journal*, 30(2):347–358, February 1992.

[35] M.E. Stern and Y.A. Adam. Capillary waves generated by a shear current in water. *Mem. Soc. r. Sci. Liege, 6e serie*, 6:179–185, 1973.

[36] S.J. Tang and N. Aubry. On the symmetry-breaking instability leading to vortex shedding. *Physics of Fluids*, 9:2550–2561, 1997.

[37] J.J. Thomson. *A treatise on the motion of vortex rings.* Macmillan, 1883.

[38] A.G. Tomboulides, S.A. Orszag, and G.E. Karniadakis. Direct and large-eddy simulation of axisymmetric wakes. *AIAA.* 31st Aerospace sciences meeting and exhibit January 11-14, 1993 Reno, NV.

[39] D. Tordella. Nonsteady stability of the flow around the circle in the foppl model. *Quarterly of Applied Mathematics*, LIII(4):683–694, December 1995.

[40] G.R. Valenzuela. The growth of gravity-capillary waves in a coupled shear flow. *J. Fluid Mech.*, 76(2):229–250, 1976.

[41] A.G. Voronovich, E.D. Lobanov, and S.A. Rybak. On the stability of gravitational-capillary waves in the presence of a vertically nonuniform current. *Izv. atm. Ocean Phys.*, 16:220–222, 1980.

[42] S.E. Widnall, D.B. Bliss, and C. Tsai. The instability of short waves on a vortex ring. *J. Fluid Mech.*, 66:35–47, 1974.

[43] S.E. Widnall and J.P. Sullivan. On the stability of vortex rings. *Proc. R. Soc. Lond. A.*, 332:335–353, 1973.

[44] S.E. Widnall and C. Tsai. The instability of the thin vortex ring of constant vorticity. *Phil. Trans. Roy. Soc.*, A287:273–305, 1977.

[45] C.S. Yih. Surface waves in flowing water. *J. Fluid Mech*, 76:209–220, 1972.